8-6-2021

# Characterization of 3D printed polyester scaffolds modified by nano-hydroxyapatite for bone tissue engineering

Weitong Chen

tjcwt99@sina.com

Follow this and additional works at: https://scholarsjunction.msstate.edu/td

Characterization of 3D printed polyester scaffolds modified by nano-hydroxyapatite for bone

tissue engineering

By

Weitong Chen


Approved by:

Lauren B. Priddy  (Major Professor)
Steven H. Elder
Santanu Kundu
Matthew W. Priddy
Michael Jaffe
Steven H. Elder (Graduate Coordinator)
Jason M. Keith (Dean, Bagley College of Engineering)



A Dissertation
Submitted to the Faculty of
Mississippi State University
in Partial Fulfillment of the Requirements
for the Degree of Doctor of Philosophy
in Biomedical Engineering
in the Department of Agricultural and Biological Engineering


Mississippi State, Mississippi

August 2021

Copyright by

Weitong Chen

2021

Name: Weitong Chen

Date of Degree: August 6, 2021

Institution: Mississippi State University

Major Field: Biomedical Engineering

Major Professors: Lauren B. Priddy

Title of Study:  Characterization of 3D printed polyester scaffolds modified by nano-hydroxyapatite for bone tissue engineering

Pages in Study: 99

Candidate for Degree of Doctor of Philosophy

It estimated that by 2023, around four million bone graft surgeries will be performed globally every year at a cost of 3.4 billion dollars, with over a million of those procedures in the US alone. The global medical costs of these procedures have reached $15 billion each year and are expected to increase at an annual rate of 13%. Currently, the gold standard for treating bone defects is the use of autograft bone from a non-load-bearing site, normally the iliac crest. Autologous bone largely avoids the limitations associated with allografts, including undesired immune response, infection, and minimal osteoconductivity. Nonetheless, the drawbacks of autografts including limited volume of bone and donor site pain and morbidity still limit their clinical efficacy. Therefore, the development of customized biodegradable scaffolds that mimic the surface properties of native bone is an urgent need.

The aim of these studies is to improve the physical, mechanical, and biological properties of 3D printed biodegradable polyester scaffolds by establishing effective methods to combine the advantages of the polyester matrix and bioceramic additives. This work will investigate: (i) the ability of alkali treatment to promote nHA immobilization on 3D printed PLA and PLGA scaffold (ii) the surface morphology, and biological and mechanical properties of 3D printed PLGA/nHA

composite scaffold, (iii) the ability of polydopamine surface modification to promote nHA immobilization on PLGA surface, and (iv) the surface morphology, and biological and mechanical properties of 3D printed PLGA-nHA composite scaffold with dopamine-nHA coating. Consequently, the 3D printed polymer-ceramic-based scaffold will be expected to display advantageous surface chemistries and morphologies, mechanical properties, and biological properties compared to PLGA-nHA composite scaffold and PLGA/pDA-nHA scaffold for bone tissue engineering.

## ACKNOWLEDGEMENTS

research. I met most of you in the freshman class and was proud of seeing your academic success as graduate student now or soon.

Lastly, although thousands of miles away from me, I would like to thank my family for their tremendous support over the past four years. Thanks to my parents and in-laws, who encouraged me to return to academia two-year after I worked in the industry. Finally, and most importantly, I would like to thank my wife, Star, for your selfless sacrifices for supporting my dream. It was a tough decision to cut off the established social relationship with your beloved colleagues, especially for a rising star and an annual sales champion of the company. I saw your tears but then your strength; I knew your sorrow but then your faith. You are A Star shining wherever you are. You made me the best partner, my soulmate.

I am blessed to have you, Dr. Lauren Priddy, my committees, lovely students, and my family. You are the angels surrounding me. Without your constant support, I cannot get this PhD. Thank you all! Let us keep printing the love in 3D!

TABLE OF CONTENTS

# LIST OF TABLES

x

LIST OF FIGURES

xiii

xiv

# 1

## INRODUCTION

### 1.1    Clinical motivation

As the strongest tissue in the human body, the bones provide major structural support and large load bearing capacity. Despite bone's strength, large/extensive bone defects beyond the capacity of self-regeneration can be caused by many factors, e.g. accidents and bone tumor resection, which result in difficulty of restoration and if untreated, lead to dramatically reduced quality of life.[1] In the United States, it is estimated that over a million people are expected to undergo bone implant surgeries with a total cost of $5 billion by the year 2020.[2] The global medical costs of bone surgery have reached $15 billion each year, in which the bone grafting and repairing will increase at an annual rate of 13%.[3] Therefore, bone tissue engineering is needed to augment the healing process.

In 1668, Dr. Job van Meekeren performed the first bone graft operation.[4] Currently, the gold standard for treating bone defects is the use of autograft bone from a non-load-bearing site, normally the iliac crest. Autologous bone avoids the potential limitations that exist with allografts, including undesired immune response, infection, less osteoconductivity, and shortage of donor tissue compared to the increasing demands.[5,6,7,8] Nonetheless, the drawbacks of autografts still limit their clinical utility. Firstly, the harvested bone volume from the iliac crest is extremely limited and is only suitable for small defects. Secondly, donor site pain and morbidity contribute to complications for the patient.

1

For conquering these issues, the metal implant has begun to attract much attention over the past decade, for applications such as bone fracture fixation[9], pelvic cup of hip joint implant[10], spinal interbody cage[11], and segmental bone scaffold[12]. Common materials for metal alloy implants include stainless steel, Co-Cr-Ni, and $TiAl_6V_4$, which show the great advantages to the autografting method, for instance, only one step surgery, non-immune-response, the sufficiently high mechanical property for supporting large load bearing bone defect, etc. However, the life span limitation of alloy implant is limited up to 15 years primarily due to the stress shielding. Young's modulus of human bone ranges from 0.02 to 30 GPa, which is much lower than that of the current alloy implants,[13] 100 to 230 GPa.[14,15,16] The implant-peripheral bone will begin to be absorbed given the reduced load and the implant start to loosen from the initial binding site. Thus, the Young's modulus is considered to be one of the most significant characteristics of the bone implant.[17]

The following major problem is the loosening implant accelerating the generation rate of the free metal particles through corrosion and wear. The metal particles will be detached from implant during constant motion and or slow oxidation in the non-neutral chemical environment (body fluid). Then, accumulated in the surrounding tissue, inflammation and localized tissue necrosis can occur.[18] Although the metal implant has been recently modified to improve the osseointegration and bone ingrowth by introducing porous surface and structure, the non-biodegradable nature of these metals can serve as a site for bacterial colonization[19]. Also, the metal implant can interference with the diagnostic accuracy of X-ray and CT images.[20]

Finally, the fabrication method for current alloy implant is not flawless either. The major methods of fabrication include machine milled or drilled into a desired shape, formed from molten metal that is poured into a mold, and shaped into its final form with the use of forces such as

2

bending or hammering, which can hardly create an implant with precisely fitted size and shape to the bone defect site for a specific patient. Thus, John Charnley, in 1958, employed poly-methyl methacrylate (PMMA/Acrylic poly) as bone cement for anchoring a total hip prosthetic.[21] The current solution is to fabricate an implant with slightly smaller parameters than the defect site, then inject the paste of PMMA/MMA composite and 10%-40% of $Ba(SO)_4$ (for radiopaque requirement) as composite bone cement to anchor the interfaces.[22] The long-term clinical history validates its high strength and bio-inertness.[23] However, some major shortcomings diminish the PMMA practicable capability. There is a potential for allergic reaction because of the toxic monomer. The PMMA additionally is highly exothermic when it cures, shrinking and later expanding due to water absorption, which can lead to peripheral tissue necrosis and hardly has positive contributions to osteo-inductivity/conductivity and biocompatibility.[22,24,25] More importantly, the cement fragments and foreign body reaction to wear debris result in local inflammation based chronic complications, implant loosening, and peripheral osteolysis, which has co-aggravate-effects with stress shielding. Nevertheless, Khaled et al. in 2016 claimed that no substitute method available so far has the similar mechanical properties with PMMA while avoiding the complications simultaneously.[26]

The revision/secondary surgery can diminish the quality of life, especially for younger patients who potentially need to retain the normal motion ability for several decades. Therefore, the revolutionary modification of current implant materials is an urgent need for improving patient outcomes in reconstructive bone surgeries.

## 1.2 Biomaterial in this study

Bone, as a unique tissue of the human body, can be regenerated and heal itself from moderate damage. However, the challenge is that massive bone defects are usually beyond the

3

capacity of self-healing. As bone is the second most often transplanted tissue, bone grafts are used for augmenting bone repair.[27] Autografting is currently the gold standard in the regeneration of bone defects but has shown disadvantages in the limited volume/shape of harvested bone, donor site pain/morbidity, severe complications (e.g. deep vein thrombosis, pulmonary embolism, and kidney failure), and extra surgical procedures. Therefore, 3D printed biodegradable bone scaffolds with the personalized geometries, biological properties, and mechanical properties serve as a robust alternative approach.

Toward this end, the monomers polylactic acid (PLA) and polyglycolic acid (PGA), and their co-polymer PLGA have attracted significant interest and been considered due to the flexible shaping process via fused deposition modeling. It is crucial to mention that PLGA, PLA, PGA, and PCL are the common synthetic and biodegradable polyesters approved by US Food and Drug Administration (FDA) for clinical use in humans.[28,29]

PLA is a thermoplastic, biodegradable, biocompatible, synthetic polymer with high strength and modulus but with relatively slow degradation rate of about 10 months to 4 years.[30] PLA can be made in highly crystalline form (L-type) or completely amorphous (D-type) due to disordered polymer chains.[31]

PGA is a rigid thermoplastic material, with high crystallinity, modulus and strength. PGA can be synthesized via polymerization of glycolic acid. It has a faster degradation rate of 6 to 12 weeks (compared to PLA). The co-polymer PLGA is used in order to combine the advantages of both polymers. Hence, the degradation rate of PLGA is much faster than PLA, given the presence of GA in PLGA and the degradation rate is highly flexible based on different requirements by adjusting the ratio of LA and GA.[32] Nevertheless, one common obstacle of polyester is hydrophobic surface, which makes the surface less ideal for cell attachment and proliferation.[33,34]

4

Thus, surface modification of the polyester is required to introduce hydrophilic functional groups, and enhance the surface roughness. Additionally, pure polyesters normally show insufficient mechanical properties. Extra materials are therefore required to mechanically reinforce the polyester-based structure, meanwhile, positively interplay or at least not to impede the surface modifications.

Bioceramics have the chemical/structural similarity to the mineral phase of native bone and effective interactions with osteogenic cells resulting in promising osteoconductivity.[353637] As a bioceramic material, hydroxyapatite (HA), generally known as $Ca_{10}(PO_4)_6(OH)_2$, has been widely applied for bone regeneration, given its chemical and structural similarity to the mineral phase of native bone and effective interactions with osteogenic cells resulting from its osteoconductive properties.[35,36,37] The cell viability and proliferation on PCL/HA composite scaffold was superior to PCL/tricalcium phosphate (TCP), another member of the bioceramic family.[38] Typically, nano-particle sized (100nm) HA (nHA) has a higher degradation rate than that of micro size (mHA) due to the increasing exposure of molecules.[39] Because of the nano-size, nHA can effectively create nanotopology, further improving wettability and cell function.[40] Since polyesters are normally hydrophobic and show poor osteoconductivity, HA has been used as support material to enhance the biological performance by improving the hydrophilicity and surface roughness[41,42,43] and promoting cell attachment and differentiation[44,45,46,47,48]. Introducing HA can also buffer the local acidic environment resulted from the acidic by-products of PLGA.[45,49,50,51,52,53]

Additionally, due to the larger surface area to volume ratio, nHA enables rapid biomineralization[54] and can better mechanically strengthen the matrix material than mHA.[55] However, because of its brittle nature, HA has poor ductility, and new bone formed in a pure HA

5

scaffold cannot sustain the loading ability due to the higher Young's modulus of HA compared to the native bone, which can cause stress shelding.[56] PLGA as a polymer binder can reduce the brittleness of HA,[57] and nHA blended polyester (e.g., PLGA) scaffolds have demonstrated improved mechanical properties compared to polymer alone. In the composite material, the presence of nHA reorganizes the polymer chain, increases the crystallinity of the polymer substrate, and inhibits crack growth in the polymer phase, thus enhancing the mechanical properties.[44,58,59,60] Expectedly, the amount of HA in the PLGA substrate is a critical variable that affects the mechanical and biological functionality of the composite. 3D printed PLA scaffolds containing 10% nHA demonstrated a higher compressive modulus than PLGA alone.[31] PLGA with 30% nano-biphasic calcium phosphate showed the highest Young's modulus compared to 10%, 20%, 40%, and 50%.[45] Similarly, PLGA with 20% nHA showed the highest compressive modulus, which decreased with increasing amount of nHA.[26] Likewise with polycaprolactone (PCL), 20% tricalcium phosphate (TCP) blended PCL scaffolds produced optimal compressive modulus compared to the 0%, 10%, and 30% counterparts.[44] The lower compressive modulus for nHA content larger than 20% might result from the disruption of the carbon chains and local aggregation of nHA particles.[46,47] Thus, when incorporating nHA in the polymer substrate, 20% appears to be the threshold for augmenting mechanical properties.

## 1.3    Surface treatment

Surface properties including chemical composition, surface wettability, and roughness play important roles in cellular activities including adhesion, proliferation, and differentiation in *in vitro* study.[61,62,63]

Various approaches to modify the surface properties of polyesters have been previously studied. Plasma treatment generates deposition of coating material via high energy ionized gas

6

particles at the top nanometer of the surface,[64] which was recently used as a surface functionalization method for biodegradable polymers.[65,66] However, plasma treatment provides insufficient degradation and roughening of the material compared to many wet chemical treatments.[67,68] The difficulty in penetrating pores is a major obstacle for modifying the surface throughout 3D scaffolds.[66] Physical adsorption is one of the most common methods for simply allowing bioactive molecules to immobilize on the polymer surface. Although physical adsorption improves surface wettability and roughness,[33,69] the structural integration between the bioactive factor and polymer may be lost upon adsorption,[70] since extent of adsorption depends on surface topography[33]. Covalent grafting is another effective method to modify the surface of polymer via the establishment of covalent bonds between bioactive molecules and reactive functional groups on the polymer surface[71]. Yet challenges with the chemicals and crosslinkers lead to the loss of molecular integration[72], thus requiring extra surface modification for introducing hydrophilic groups, similar to physical adsorption. Surface entrapment is a two-step method that involves polymer swelling in a mixture of solvent, non-solvent, and bioactive molecules. Within the swollen layer, the molecules are able to be "entrapped" through immersion in a non-solvent mixture[73] which improves the surface hydrophilicity and biocompatibility[74], while no significant influences on surface morphology were found.[75] Despite the success of these methods for modifying polymer surfaces, the implementation of these technologies is limited due to instrumentation requirements and complicated reaction controls.[76]

Compared to the aforementioned techniques for modifying the chemical and morphological properties of polymer scaffolds, alkali treatment (AT) is less time consuming and labor-intensive than surface entrapment,[77] and more effective at penetrating porous structures and more cost-effective than plasma treatment.[78] Alkali treatment is also advantageous due to the

7

stronger covalent bonds than the weak bond of physical adsorption,[70] while avoiding additional modifications required prior to covalent grafting[79]. AT as a wet chemical method is the carbon chain scission (hydrolysis) at ester bonds which also introduces carboxyl and hydroxyl groups. The treatment is performed by immersing a polyester (e.g., PLA, polycaprolactone (PCL), poly(lactic-co-glycolic acid) (PLGA), etc.) in a strong basic solution, such as sodium hydroxyl, with specific pH for minutes to days[80,81,82,83], which introduces hydrophilic groups and morphological changes on the surface. To form reactive carboxyl groups, PLGA nanofibrous membranes were soaked in sodium hydroxyl (20mg/mL, pH=14.1) for 2 hours, resulting in an increase in surface roughness.[84] The average diameter of PCL fibers was slightly reduced with the treatment of 2N (pH=14.3) sodium hydroxyl for 12 hours.[85] Furthermore, the surface of PLA film wrinkled after alkali treatment at pH 12.0 for 1 hour at room temperature.[86] Although the process of AT with sodium hydroxyl is simple, one disadvantage is the difficulty of removing sodium hydroxyl after the process[87]. Alternatively, ammonia can be completely evaporated after surface treatment. Although it is a weak base, ammonia solution can become more strongly alkaline by adjusting the concentration. Few studies using ammonia treatment on PLA microspheres[88] and nanofibers[86] have been reported, and the influence of duration of ammonia-alkali treatment on the surface and structure of polymers has not been studied.

Recently, the mussel-inspired polydopamine (pDA) has been demonstrated as a simple coating method for surface modification of various materials including polymers, ceramics, and metals.[89] Polydopamine has a similar molecule structure to Mytilus edulis foot protein-5 (Mefp-5), which is a typical adhesive foot protein in mussels.[90] Thus, a surface treatment inspired by mussels' adhesive mechanism becomes an equipment-/material-independent alternative approach to produce effective poly(dopamine) (pDA) coating via self-polymerization by simply dipping a

8

substrate into alkaline dopamine solution.[91] Unlike traditional surface modifications, polydopamine is capable of coating on both hydrophobic and hydrophilic surfaces[92,93] through oxidative self-polymerization under room temperature in a single step, without the requirements of advanced equipment. More importantly, pDA has been shown to significantly improve the immobilization of nano-HA (nHA),[94] and increase the surface roughness and hydrophilicity,[95] which are collectively beneficial to osteogenic cell adhesion and differentiation.[96,97]

Although some specific formation process of pDA coating is still to be discovered, multiple intermediates of the mechanism are confirmed. At the beginning of the oxidation process, the monomer DA is oxidized into dopamine quinone, which then forms leucodopaminechrome (DAL) through cycloaddition reaction. Further oxidation of DAL produces 5,6-dihydroxyindole (DHI). Consequently, it forms 5,6-indolequinone, which branchingly reacted with DHI, resulting in a majority of dimers and higher-order-oligomers self-polymerized into a coating layer on substrate[98] through covalent bonds, hydrogen bonds, π bonds and catechol/quinone interactions[99,100,101]. Among the aforementioned bonds, π bonds and salt displacement between the amine groups and aromatics rings mainly contribute to the strong attractions between the poly-catecholamine molecules.[102] The interactions between the pDA coating and the substrate rely on covalent and noncovalent interactions as well.[103] Additionally, the pDA coating on the substrate, especially polymer, is very stable and durable in numerous environments, as long as the pH not exceeding 13.[104,105,106]

Based on the analysis of mechanism, it reveals that the formation of pDA coating entirely depends on the oxidation of DA, which leads to the remarkable advantage of this surface modification method that pDA coating can be formed on both hydrophobic and hydrophilic

9

surfaces[92,93] and a wide range of organic and inorganic materials, such as polymers, metals, and ceramics.[107]

Instead of altering bulk properties, as a novel method of surface modification, pDA can strongly affect surface chemistry, morphology, hydrophilicity, and mechanical properties.[90] The surface roughness of PCL films and polypropylene (PP) mesh was improved after treating with pDA.[108,109] Water contact angle was dramatically decreased by coating pDA on PLA scaffold and Ti surface. [95,110]

Polydopamine also provides remarkable anti-microbial properties. The growth of *E. coli* was inhibited by a low dose of pDA (100 mg $L^{-1}$) in the media.[111] PLA scaffold soaked in 2mg/ml had a significantly lower amount of adhered S. aureus. It exhibited a higher mortality rate in comparison with PLA, indicating that the antibacterial activity of pDA could be increased in the coating layer.[112] The antibacterial properties would be further improved by absorbing silver or nanoparticles on the pDA coating.[113,114]

Polydopamine coating has been proved to promote the adhesion and proliferation of certain cell types to various surfaces due to an increase in the immobilization of serum adhesive proteins.[115,116,117,97,118] This may be directly related to the improvement of surface hydrophilicity[119] and functional groups (e.g., $OH^-$, $NH_2^-$)[120]. In a study of pDA coating on PLA scaffold,[112] higher hADSC cell attachment rate and proliferation to PLA/pDA compared with PLA through the entire culturing process. Type I collagen (Col I) secretion was significantly higher on the substrates with the highest amount of pDA coating 1-hour post-seeding.[112] More importantly, pDA coating itself is beneficial for osteogenic capability. Since pDA increases surface roughness, the micro-/nano-patterns on the substrate are also advantageous to osteoblast differentiation.[95] The average roughness (Ra) value of the pDA coated PLGA film surface was significantly higher than the pure

10

PLGA film.[93] The pDA coating may provide topographical stimulation that accelerates cell attachment process[121] and therefore activates intracellular signal transductions.[122] Even on the bioinert metal implant (e.g. Ti and Ti alloys), the pDA-assisted surface modification can also offer the osteoconductivity and osteoinductivity and augment cell viability, proliferation, differentiation, and material mineralization [107,123,124,125].

From the molecular biology aspect, a study demonstrated that MC3T3 cells express functional DA receptors, which improve proliferation and mineralization, and pDA upregulate osteoblast differentiation.[126] In another study, pDA coated PCL scaffold significantly stimulate proliferation, differentiation, osteogenesis, and angiogenesis of hMSCs.[127] In recent research, pDA induces osteogenic differentiation of BMSCs since that DA mimicked D1 receptor agonist and further upregulated Runx2 transcriptional activity.[128]

Since pDA can tightly bind on various surfaces and form a durable layer, it serves as an intermediate for conjugation of biomolecules containing amino or thiol groups[91,129,130,131,132,133] (e.g. BMP-2 and VEGF). Many growth factors (e.g. BMP-2) immobilized by pDA retain high activity and that the immobilization process does not affect the structure of the substrate.[134] Polydopamine also interacts with various metal ions[135,136] through its catechol and amine group onto scaffold surfaces without surface pretreatment, which enables a powerful potential that inducing HA to effectively deposit on polymer surface.[107]

It is demonstrated that nHA could be effectively deposited on various surfaces modified by pDA. Nano-HA particles could be immobilized onto Ti substrates via dopamine self-polymerization to form a porous and hierarchical micro/nanostructured composite coating, which showed promising osteoinductivity.[94] In a comparable research, the surface roughness also further increased after HA coated on pDA immobilized Ti scaffolds, which exhibited significantly higher

11

ALP activity.[95] Similar results observed from biodegradable polymer substrates as well. HA formed on the pDA coating enhanced adhesion of preosteoblasts to porous polycaprolactone (PCL) scaffolds.[137] In another *in vivo study*, the nHA, human-like collagen (HLC), and BMP-2 were incorporated in PCL scaffold with or without the presence of pDA. The ALP activity of the nHA/RHLC/PLA-BMP-2 group was significantly lower than that of nHA/HLC/PLA-pDA-BMP-2 group, which was related to the different amount of nHA and BMP-2 from the scaffolds with different treatments.[134] Most importantly, in a recent study, nHA was coated on pDA modified PCL substrate (PCL/pDA-nHA).[97] The results suggested that PCL/pDA-nHA improved cell attachment, proliferation, and differentiation without using osteogenic growth factors in *in vivo* experiments. Therefore, there is a vast potential to discover more capabilities of pDA assisted nHA immobilization on 3D printed biodegradable polymer.

Accordingly, the overall objective of this research is to create a 3D printed scaffold with a specific polyester, select an appropriate surface treatment method, and consequently find an effective way to integrate the positive characteristics of polyester and bioceramic. We expected that the developed scaffold shows improved surface conditions, suitable biological properties, and mechanical properties through a serial of systematic characterizations and evaluations.

12

# INVESTIGATE THE EFFECTS OF NHA COATING ON 3D PRINTED PLA SCAFFOLDS ASSISTED BY ALKALI TREATMENT

Surface modifications play a vital role in the activation of polymer surface for bone tissue engineering. However, the traditional surface treatments are normally constrained by tedious preparations, and harsh demands on equipment and reaction conditions,[138] which add difficulties to the manipulations of effective surface modification. This aim will investigate the capability of alkali treatment as a surface modification method on 3D printed PLA scaffold and on nHA deposition. The *objectives* of the current study were: (i) to investigate the effect of alkali treatment time (1-hour vs 6-hour) on nHA coating, and (ii) to characterize the effects of nHA coating on the chemical, mechanical, and biological properties of 3D printed PLA scaffolds. Both modifications were assessed through the observation of surface morphology and chemistry, hydrophilicity, mechanical properties, and cell attachment/proliferation. The efficacy of surface modifications will be analyzed by SEM, EDX, FTIR, and WCA. Compression testing assesses the influence of surface modifications on the mechanical properties. CCK-8 assay evaluates the potential differences in cell attachment and proliferation of different scaffolds. It is *hypothesized* that (i) 6-hour (but not 1-hour) alkali treatment would enhance nHA coating, (ii) the nHA coating on the 6-hour alkali-treated surface would increase hydrophilicity and cell attachment/growth, and (iii) stiffness and effective Young's modulus would be reduced by 6-hour alkali treatment.

13

## 2.1    Rationale

As aforementioned, the combination of polyester and bioceramics will integrate the positive characteristics. Nevertheless, since the bioceramic particles were covered and entrapped in the polymer substrate, the hydrophilicity and cell attachment were not significantly improved.[139,140,141] In this specific chapter, nHA coating on 3D printed PLA scaffold was selected as the research model. Since alkali treatment (AT) is advantageous over the current modifications, such as the capability of penetrating the porous structure, strong covalent bonds, and less labor-intensive, AT is employed as surface treatment methods to introduce hydroxyl functional group to the PLA substrate as shown in **Figure 2.1**.

A series of pilot studies (1hAT, 2hAT,…6hAT) were previously conducted to decide the AT time producing significant changes of strut width to the scaffold. The major objectives of this aim are: (i) to investigate the effect of alkali treatment time on nHA coating, and (ii) to characterize the overall differences of nHA coating as a secondary surface modification. Both modifications were assessed through the observation of surface morphology and chemistry, hydrophilicity, mechanical properties, and cell attachment/proliferation. The *hypotheses* were that: (i) 6-hour (but not 1-hour) alkali treatment will enhance nHA coating on 3D printed PLA scaffolds, (ii) the nHA coating on the 6-hour alkali treated surface will increase hydrophilicity and cell attachment/growth, and (iii) stiffness and effective Young's modulus will be reduced by 6-hour alkali treatment.

14

## 2.2    Experimental approach and data analysis
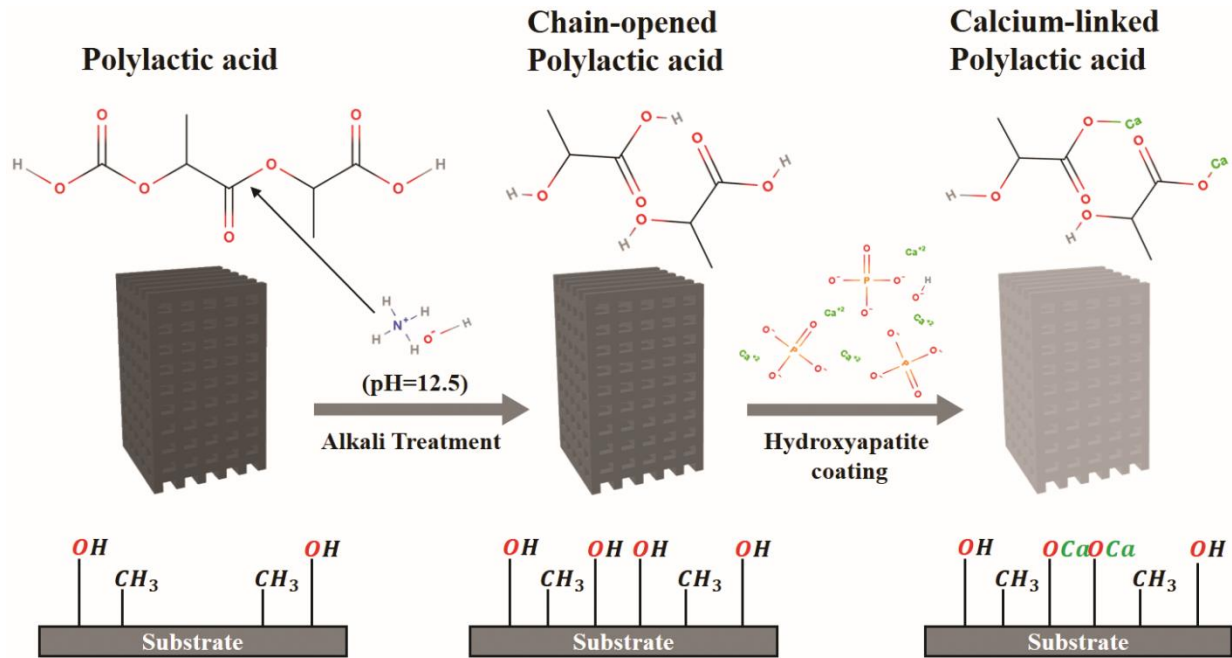


Figure 2.1    Mechanism of alkali treatment and nHA coating on PLA substrate.

Table 2.1    The global structure/surface morphologies of scaffold were characterized by SEM.

| Experimental groups | Structure | Dimensions | Sample size |
|---|---|---|---|
| PLA | Scaffold | 7×7×2 mm | n=1 |
| PLA/nHA | | | n=1 |
| PLA/1hT | | | n=1 |
| PLA/1hAT/nHA | | | n=1 |
| PLA/6hAT | | | n=1 |
| PLA/6hAT/nHA | | | n=1 |

Table 2.2    The surface chemistries were characterized by EDX.

| Experimental groups | Structure | Dimensions | Sample size |
|---|---|---|---|
| PLA | | | n=6 |
| PLA/nHA | | | n=6 |
| PLA/1hT | Scaffold | 7×7×2 mm | n=6 |
| PLA/1hAT/nHA | | | n=6 |
| PLA/6hAT | | | n=6 |
| PLA/6hAT/nHA | | | n=6 |

Table 2.3    The surface chemistries were characterized by FTIR.

| Experimental groups | Structure | Dimensions | Sample size |
|---|---|---|---|
| PLA | | | n=1 |
| PLA/nHA | Scaffold | 7×7×2 mm | n=1 |
| PLA/6hAT | | | n=1 |
| PLA/6hAT/nHA | | | n=1 |

Table 2.4    The hydrophilicity was measured by water contact angle.

| Experimental groups | Structure | Dimensions | Sample size |
|---|---|---|---|
| PLA | | | n=5 |
| PLA/nHA | Solid plate | 7×7×2 mm | n=5 |
| PLA/6hAT | | | n=5 |
| PLA/6hAT/nHA | | | n=5 |

Table 2.5    The compression testing evaluated stiffness and effective Young's modulus.

| Experimental groups | Structure | Dimensions | Sample size |
|---|---|---|---|
| PLA | | | n=8 |
| PLA/nHA | Scaffold | 4×4×8 mm | n=8 |
| PLA/6hAT | | | n=8 |
| PLA/6hAT/nHA | | | n=8 |

16

Table 2.6    The *in vitro* study investigated cell attachment and proliferation.

| Experimental groups | Structure | Dimensions | Sample size |
|---|---|---|---|
| PLA | | | n=10 |
| PLA/6hAT | Scaffold | $7\times7\times2$ mm | n=10 |
| PLA/6hAT/nHA | | | n=8 |

## 2.3    Results

### 2.3.1    Characterization of global structure

No differences in strut width were found between PLA and PLA/nHA, PLA/1hAT and PLA/1hAT/nHA, or PLA/6hAT and PLA/6hAT/nHA, indicating nHA coating did not significantly influence the strut width. Moreover, 1hAT reduced the strut width only in the presence of nHA coating, as the effect was observed only between PLA/1hAT/nHA ($405.14 \pm 9.72$ µm) and PLA/nHA ($435.87 \pm 10.46$ µm). Six-hour AT induced significant decreases in strut width, as PLA/6hAT ($228.1 \pm 5.47$ µm) and PLA/6hAT/nHA ($214.5 \pm 5.15$ µm) were lower than all other groups. The strut width decreased by 46.9% (PLA vs PLA/6hAT) and 50.8% (PLA/nHA vs PLA/6hAT/nHA) (Figure 2.3). The average cross-sectional area is summarized as well in **Figure 2.3**.

17
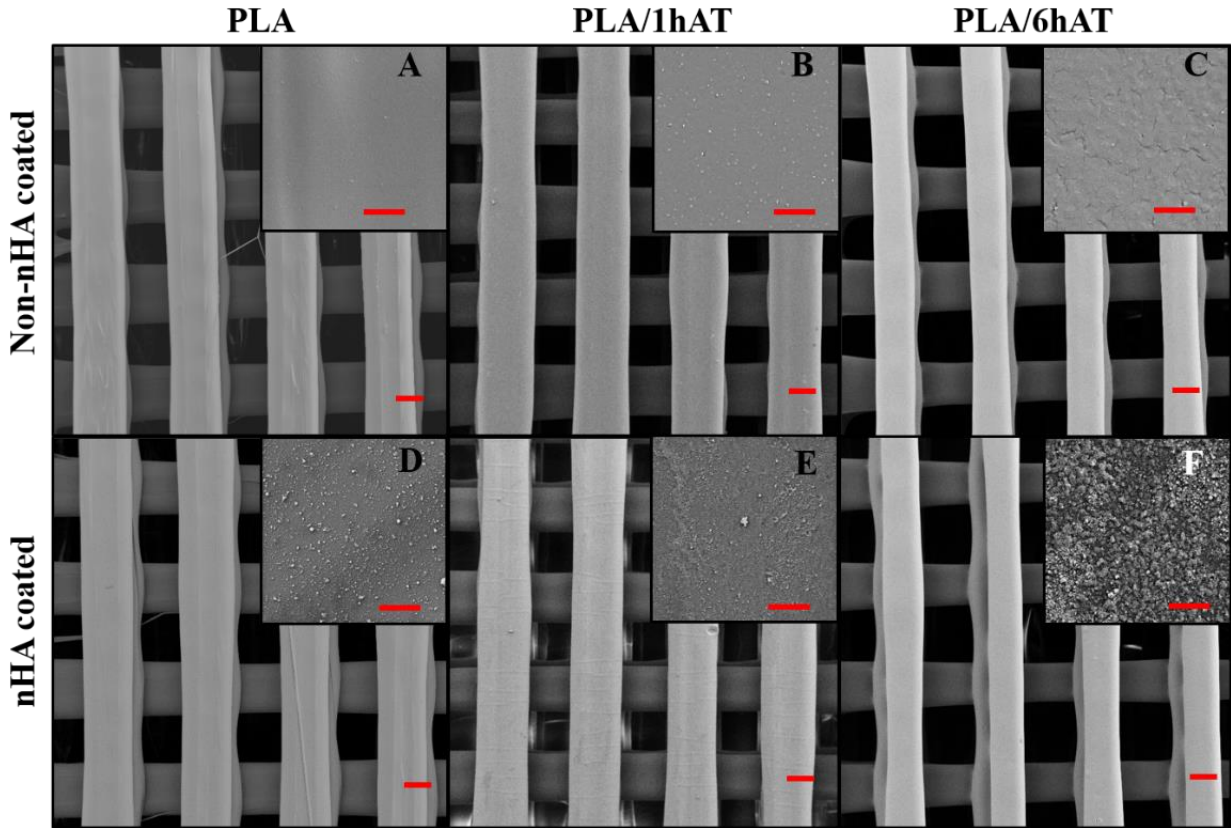
Figure 2.2    Scanning electron microscopy (SEM) images of strut width (larger images, scale bar=200 µm) and surface morphology (inset images, scale bar=10 µm).

(A) PLA, (B) PLA/1hAT, (C) PLA/6hAT, (D) PLA/nHA, (E) PLA/1hAT/nHA, and (F) PLA/6hAT/nHA.
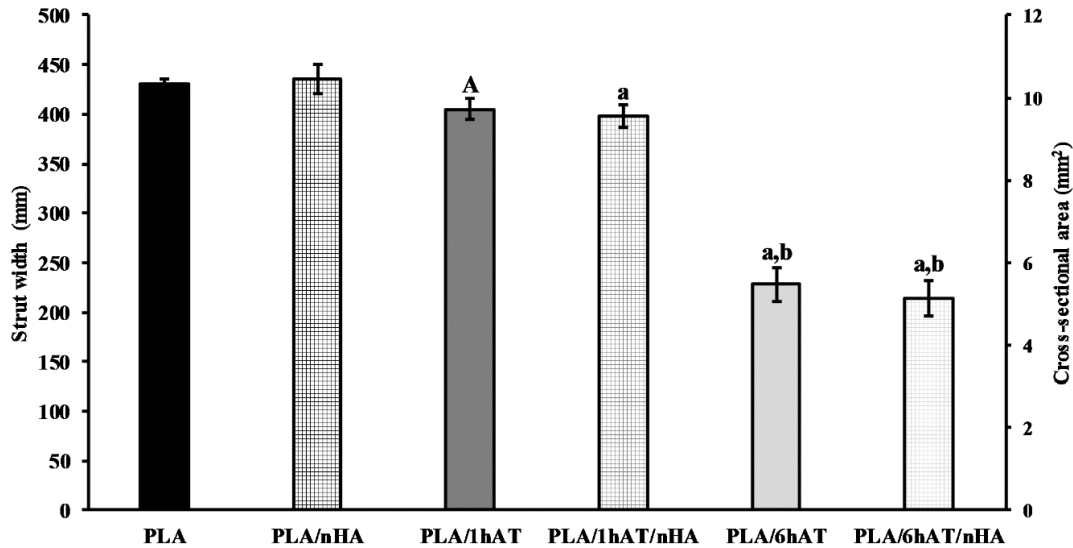
Figure 2.3    Strut width and cross-sectional area (n=8, $p<0.05$).

No significant differences in PLA versus PLA/nHA, PLA/1hAT versus PLA/1hAT/nHA, and PLA/6hAT versus PLA/6hAT/nHA. "A" denotes significantly lower strut width and cross-sectional area compared to PLA/nHA. "a" denotes significantly lower strut width and cross-sectional area compared to PLA and PLA/nHA. "b" denotes significantly lower strut width and cross-sectional area compared to PLA/1hAT and PLA/1hAT/nHA.

### 2.3.2    Characterization of surface morphology and chemistry

The surface of PLA/6hAT was noticeably rougher, with a wavy surface and numerous micro-cracks (**Figure 2.2**). The amount of nHA coating on the PLA/6hAT surface appeared higher than that on PLA and PLA/1hAT, while similar amounts of nHA coating on PLA and PLA/1hAT were observed. The thickness of nHA coating on PLA/6hAT/nHA was $0.97 \pm 0.14$ µm (**Figure 2.4**), while no measurable coating was detected on PLA/nHA or PLA/1hAT/nHA. In the EDX spectra, a small peak at 3.8 keV was found in PLA/6hAT/nHA, which was determined to be a calcium peak with 2.48 wt% of the total weight.

19

The FTIR spectra (**Figure 2.5**) revealed that multiple peaks of PLA/6hAT/nHA overlapped with peaks of nHA (dark grey bands), including P-O (568 cm$^{-1}$, 598 cm$^{-1}$, 962 cm$^{-1}$), P=O (1036 cm$^{-1}$), and OH$^-$ (625 cm$^{-1}$), which indicated crystalline nHA.
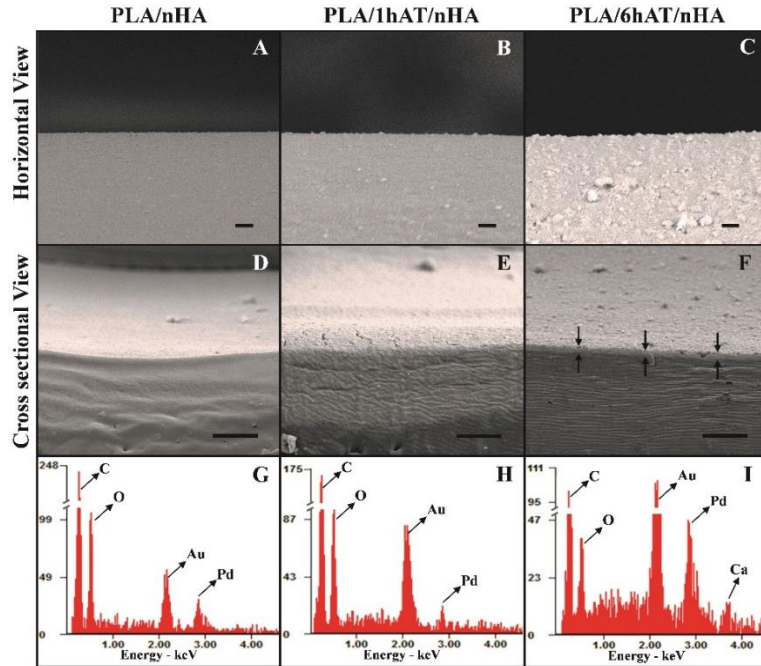


Figure 2.4    SEM images of horizontal view (A-C, scale bar=2 µm) and cross-sectional view (D-F, scale bar=10 µm).

(F) Arrows indicate the layer of nHA coating. (G-I) Energy dispersive X-ray spectroscopy (EDX) spectra. Arrows indicate the detected elements, in which a Ca peak was found only in PLA/6hAT/nHA. Note: the scales of the y-axes are different.
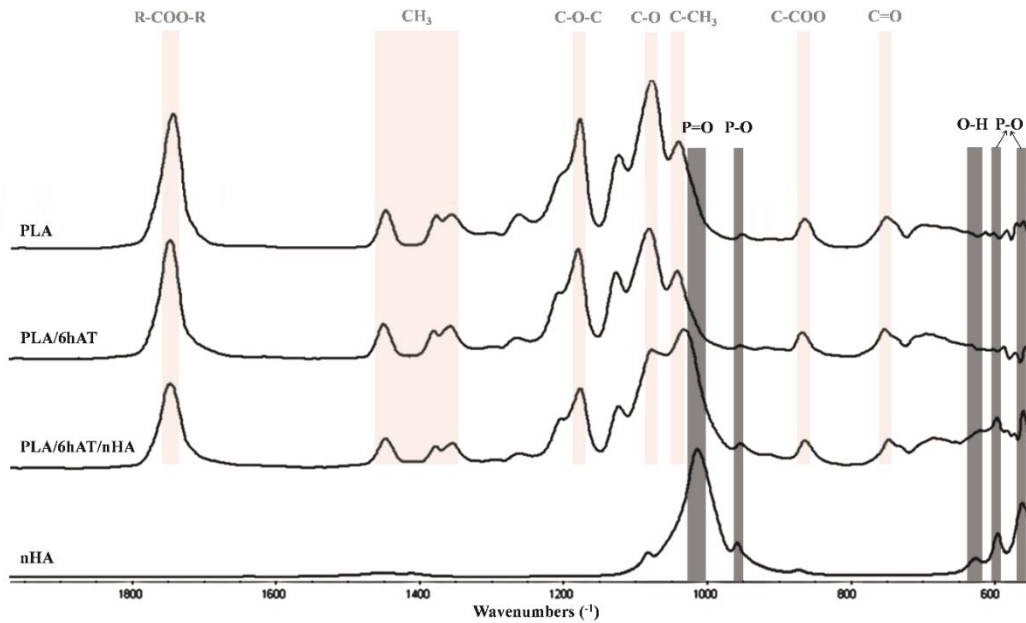
Figure 2.5    FTIR spectra (absorbance). Light gray bands indicate functional groups present in PLA, and dark gray bands indicate functional groups present in nHA.

### 2.3.3    Water contact angle analysis

Water contact angles of PLA, PLA/6hAT, PLA/nHA, and PLA/6hAT/nHA were reduced (for all pairwise comparisons) in the following order: $116.4°\pm1.8° > 96.9°\pm1.7° > 60.1°\pm3.4° > 38.8°\pm 4.8°$ (**Figure 2.6**).

21
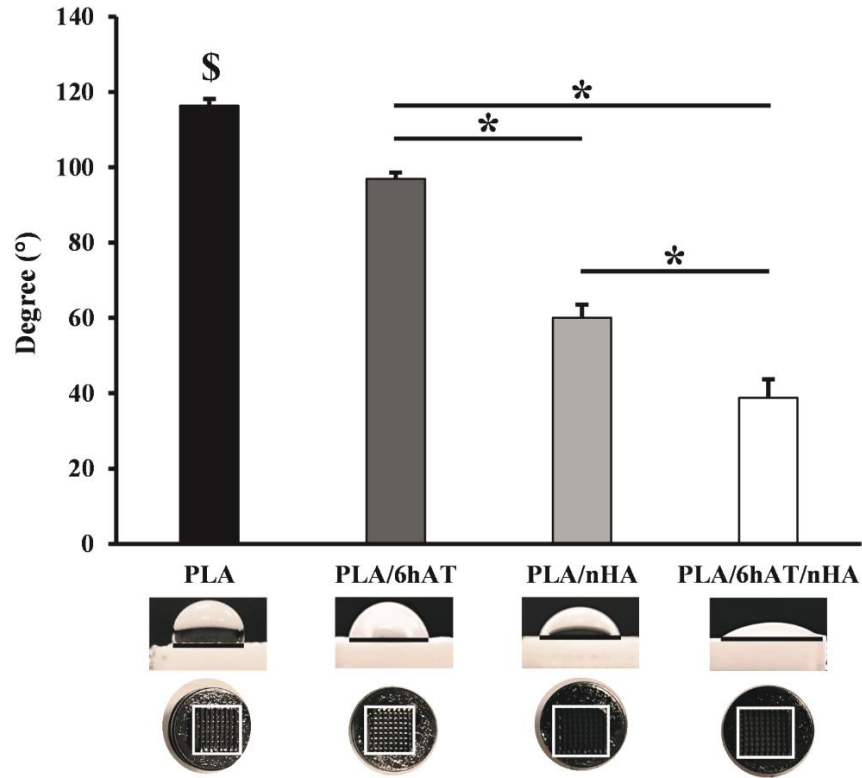
Figure 2.6    Water contact angle (n=5, *$p<0.0001$) and light of the nHA coated scaffold was more diffusely reflected.

### 2.3.4    Mechanical Properties

Stiffness ($k$) of PLA and PLA/nHA were higher than PLA/6hAT and PLA/6hAT/nHA (**Figure 2.7**). Similarly, effective modulus ($E_e$) for PLA was higher compared to that for PLA/6hAT and PLA/6hAT/nHA. No significant difference in effective Young's modulus ($E_e$) was found between PLA and PLA/nHA, which demonstrated that the amount of nHA on the PLA/nHA surface was not sufficient to augment mechanical properties, despite the greater hydrophilicity of PLA/nHA compared to PLA. Interestingly, no significant difference in Ee was observed between PLA/nHA and PLA/6hAT/nHA.

22
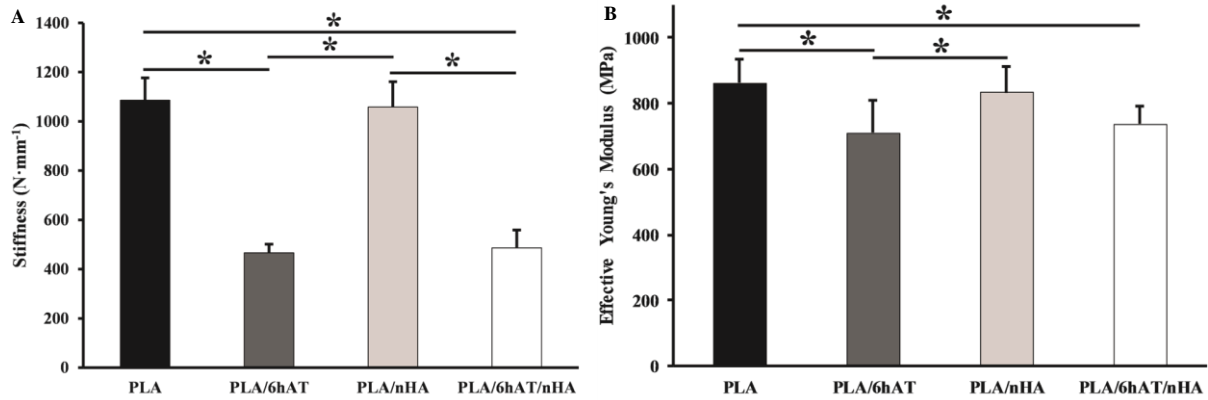
Figure 2.7    Stiffness (A) and effective Young's modulus (B). (n=8, *$p<0.05$)

### 2.3.5    Cell Proliferation Assay

The cell number on PLA/6hAT/nHA was the highest at all-time points, and cell numbers were similar between PLA and PLA/6hAT at all-time points (**Figure 2.8A**). The cell number per unit area showed a clearer trend that PLA/6hAT was higher than PLA, and PLGA/6hAT/nHA was higher than PLA/6hAT when the reduced cross-sectional area was considered (**Figure 2.8B**). The normalized data (**Figure 2.8C**) showed less proliferation on PLA/6hAT/nHA on day 5.

23
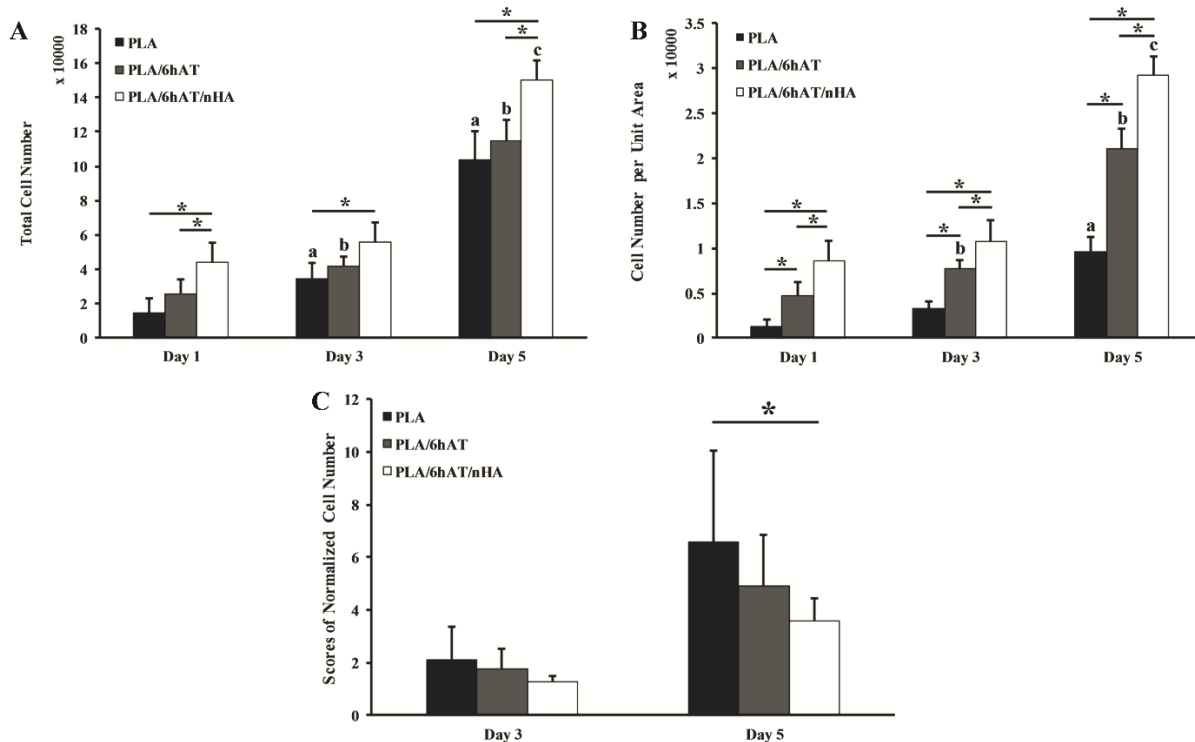
Figure 2.8    Total cell number (A), cell number per unit area (B), and cell number normalized to day 1 (C).

"a" denotes increases over time for PLA. "b" denotes increases over time for PLA/6hAT. "c" denotes increases over time for PLA/6hAT/nHA. *Differences between groups at the same time point. (n=10, $p<0.05$ for all comparisons).

## 2.4    Discussion of the current method

In the present study, the effects of alkali treatment and nano-hydroxyapatite coating on 3D printed PLA scaffolds were evaluated. Alkali treatment is a simple and efficient method to introduce carboxyl functional groups on PLA carbon chains.[142] The struts from as-printed scaffolds (**Figure 2.2A**) were printed uniformly except for a few thin PLA residuals on the surface of struts and in the middle of pores, indicating the capability of consistent printing of the printer. From the global view of the SEM images of all groups, the joint area of the top and second-from-top layers

24

showed a slightly increased strut width compared to the spacing in between struts, likely due to the auto-adjustment process for the printer to reinforce the bridging struts, which is typical for FDM printers[143].

In the AT scaffolds, the average strut width decreased after 1h and 6h AT, demonstrating that the ammonia solution degraded the PLA material. The strut width decreased by 46.9% (PLA vs PLA/6hAT) and 50.8% (PLA/nHA vs PLA/6hAT/nHA). This is the first time, to our knowledge, that quantitative changes in polymer strut width following alkali treatment have been reported, while a few comparable results have been reported. Although quantitative differences were not evaluated, PLA fibers in NaOH (pH=11.0, 7 days) appeared thinner than those in PBS (pH=7.4, 8 days).[144] Microcracks similar to the ones observed here have been observed on the surface of PLA fibers after 2-day alkali treatment.[82] The diameter of electrospun PCL fibers appeared slightly reduced after aqueous NaOH treatment (pH=14.3, 12 hours), but no quantification was reported.[85] In another study, PLA microspheres were treated by NaOH solution (pH=13.3) for 5, 10, 20, 30, or 40 minutes. The average diameter of the alkali-treated PLA microspheres was reduced after only 5 min and kept decreasing with increasing treatment time.[145] The diameter decreased by 40% for the 40 min group, which was similar to the strut width changes resulting from 6hAT in this study. It is possible that the similar change (~50% decrease in width) with longer treatment time in the present study was due to the smaller surface area to volume ratio for our 0.4 mm wide struts compared to microspheres.

Ester bond hydrolysis (degradation) was demonstrated not only on the global structure but also at the micro scale, as indicated by higher magnification SEM images. Although surface morphology for PLA/1hAT appeared similar to untreated PLA, the surface of PLA/6hAT was noticeably rougher, with a wavy surface and numerous micro-cracks (**Figure 2.2A-C, insets**). The

25

nHA particles on PLA, PLA/1hAT, and PLA/6hAT were observed via the high magnification SEM (**Figure 2.2D-F, insets**). The amount of nHA coating on the PLA/6hAT surface appeared higher than that on PLA and PLA/1hAT, while similar amounts of nHA coating on PLA and PLA/1hAT were observed. The SEM images of nHA coating following 6hAT suggested that the 6hAT process effectively promoted nHA coating of the PLA scaffolds. This likely occurred via cleavage of the carbon chain and exposure of carbon radicals that were able to bind hydroxyl groups from the alkali solution, which subsequently provided a suitable surface condition for capturing the nHA particles. A previous study also demonstrated that pretreatment by alkaline hydrolysis effectively promoted the formation of a dense and bioactive layer of HA nanoparticles on PLA microspheres.[145] Moreover, with longer alkali treatment time (5, 20, 30 minutes), a thicker and more visible layer of HA nanoparticles was formed on the surface.[145] Similarly, our results suggested that the surface roughness appeared to be improved and a noticeable nHA layer was formed on only the PLA/6hAT/nHA surface (**Figure 2.4F**).

Although SEM images showed evidence of nHA particles on all surfaces, EDX spectra detected and quantified a calcium peak on only the PLA/6hAT/nHA surface. A small peak at 3.8 keV was found in PLA/6hAT/nHA, which was determined to be a calcium peak with 2.48 wt% of the total weight and was slightly higher than other trace metals such as Ti (2.03%), Co (1.58%), and Cu (1.29%). Collectively, the calcium amount in PLA/6hAT/nHA might barely exceed the detection threshold of EDX, even with an obvious layer of coating in the SEM image (**Figure 2.4F**). The common elements were also detected for all the groups, such as C and O. Interestingly, the gradually decreased intensity of C and O in the order of PLA/nHA, PLA/1hAT/nHA, and PLA/6hAT/nHA (**Figure 2.4G-I**) may be due to the loss of carbon chains in PLA with increasing alkali treatment time. Given the limited influence of 1hAT on strut width and nHA coating, only

26

the 6-hour alkali treatment groups were used in the subsequent analyses for effectively evaluating the influence of AT.

To confirm the nHA coating chemically, FTIR spectra were detected to determine the functional groups of nHA. Interestingly, the C-CH$_3$ bonds in PLA/6hAT/nHA were right-skewed, instead of aligning with those in PLA and PLA/6hAT, due to the existence of P=O bonds at the right. A similar phenomenon appeared at 962 cm$^{-1}$ (P-O bond) and 625 cm$^{-1}$ (O-H bond) in PLGA/6hAT/nHA; these peaks showed a trend to approximate the wavenumbers of P-O and OH in the nHA alone. All the top three spectra in **Figure 2.5** showed an R-COO-R group with one of the major peaks at 1750cm$^{-1}$ that reflected the carbon backbone linked by ester bonds. Whereas, the peak absorbance of PLA/6hAT/nHA was much lower than PLA and PLA/6hAT, which agreed with previous work that the R-COO-R peak in PLA/HA coating was reduced compared to that of PLA.[86] Given the existence of Ca$^{2+}$, the R-COO-R peak was weakened likely since part of the O=C-OR was hydrolyzed to form O=C-OH. Furthermore, the hydrogens were likely substituted by Ca$^{2+}$ to form R-COO-Ca$^{2+}$ via the ionic interactions between PLLA and nHA.[86] As one of the strongest chemical bonds, ionic bonds might provide sufficient energy to prevent the coated nHA particles from detaching during the ultrasonication process. This could explain why the nHA particles were barely coated on PLA and PLA/1hAT, since nHA was likely deposited physically and/or the number of R-COOH groups available for nHA to ionically interact with were limited.

Hydrophilicity is one of the critical surface conditions that affects the practical application of tissue engineering scaffolds,[141] as strong hydrophobic surfaces are not conducive to cell attachment and migration.[146,147] Water contact angle was measured to determine the hydrophilicity of the alkali-treated and nHA-coated surfaces. Since a hydrophilic surface may be defined by a WCA less than 90°,[81] PLA/nHA and PLA/6hAT/nHA were deemed hydrophilic. The effect of

27

both AT and nHA ($p<0.0001$ compared to untreated PLA) suggested that both surface treatments significantly improved the wettability of the PLA surface and nHA provided more wettability to the surface. More importantly, PLA/6hAT/nHA was the most hydrophilic, resulting in the lowest WCA. Notably, a significant interaction was detected between AT and nHA ($p = 0.0031$) in the two-way ANOVA of WCA data, which indicated that AT promoted the formation of nHA coating on the PLA surface. Interestingly, after sputter coating for SEM imaging, the light reflection was noticeably different (**Figure 2.6** bottom pictures). Presumably due to their rougher surfaces (as also shown in SEM), nHA coated scaffolds apparently reflected less light than non-nHA coated scaffolds

Sufficient compressive mechanical properties of 3D printed scaffolds are crucial for load-bearing biomaterials in bone tissue engineering applications. Since stiffness depends on the geometry of a structure, it is reasonable to see higher stiffness in non-AT treated groups compared to AT-treated groups because the strut width decreased by approximately 100% as a result of 6 hours of alkali treatment, and the porosity increased by 100%. A similar, although dampened, effect of 6hAT on effective Young's modulus was observed, as effective modulus for PLA was higher compared to that for PLA/6hAT and PLA/6hAT/nHA, due in part to the reduced strut width (and cross-sectional area) following PLA hydrolysis during alkali treatment. Others have also demonstrated that adjusting the geometry parameters of a porous structure significantly changed the internal stress distribution and thus influenced effective modulus.[148] For example, a decrease in strut width would reduce cross-sectional area and increase porosity, thus resulting in a reduced effective modulus.[3,149,150,151] Besides changes to strut width at the macroscale, and despite the similar FTIR spectra between PLA and PLA/6hAT, changes in polymer morphology and/or

28

chemistry may have further contributed to reduced mechanical properties as a result of alkali treatment.

Surface modification with nHA had no effect on stiffness, which demonstrated that the amount of nHA on the PLA/nHA surface was not sufficient to augment mechanical properties, despite the greater hydrophilicity of PLA/nHA compared to PLA. Interestingly, the effective modulus of PLA/nHA was not higher than PLA/6hAT/nHA. Given that the Young's modulus of nHA is 7 to 13 GPa (~ an order of magnitude higher than that of PLA), the nHA coating following alkali treatment may have functioned as a load-bearing component, reinforcing the thinner struts and compensating for the loss of polymer following 6hAT. As more material was lost during 6hAT compared to 1hAT, the nHA in PLA/6hAT/nHA likely comprised more of the total volume of a strut (and of the entire scaffold) compared to untreated PLA scaffolds. As a result, PLA/6hAT/nHA possessed advantageous surface conditions while also mitigating a decrease in effective modulus.

Due to limited accuracy during the 3D printing process, the inconsistent cross-sectional area along the height of the scaffold could have an effect on the calculation of equation (**A.1**)[152] and introduce localized, non-uniform deformation along the height of the scaffolds. Regardless of printer accuracy, the application of Hooke's law is limited here because the cross section is not uniform along the length of the sample (i.e., alternating hatch pattern layer by layer), further contributing to non-uniform deformation as a function of scaffold height. Nonetheless, the qualitative trends of effective modulus between groups still could reflect relative structural and material changes. Additionally, for better mimicking the mechanical properties of the scaffolds in in vivo condition, it will be meaningful to conduct the mechanical testing under 37°C and wet environment in an *ex vivo* model.

29

To investigate the *in vitro* biocompatibility of the modified scaffolds, osteosarcoma cells were cultured on PLA, PLA/6hAT, and PLA/6hAT/nHA scaffolds. Metabolic activity (viability) was evaluated on days 1 (attachment), 3, and 5 (proliferation) (**Figure 2.8A**). The highest cell number on PLA/6hAT/nHA and the similar cell numbers PLA and PLA/6hAT at all-time points demonstrated the efficacy of the 6hAT and nHA combination surface modification for enhanced cell function. Except for no change in cell number from day 1 to day 3 for PLA/6hAT/nHA, the cell number in all the groups increased with time, as expected. Since cross-sectional area was reduced after 6hAT, the total cell numbers were divided by the corresponding cross-sectional areas (PLA, 10.32 $mm^2$; PLA/6hAT, 5.47 $mm^2$; PLA/6hAT/nHA, 5.15 $mm^2$) to obtain the "cell number per unit area". The cell number per unit area revealed differences in all pairwise comparisons at each time point (**Figure 2.8B**). The results demonstrated that the 6hAT alone had a positive effect on cell growth when the reduced cross-sectional area was considered. Similarly to findings from the non-normalized data, the combined modifications of 6hAT and nHA optimally promoted cell growth among the experimental groups. Interestingly, when cell numbers from days 3 and 5 were normalized to those on day 1, PLA had a higher score than PLA/6HAT/nHA on day 5 (**Figure 2.8C**), indicating less proliferation on the combination scaffolds at this time point and suggesting the positive effect of 6hAT/nHA surface modifications may be due primarily to enhanced attachment, not proliferation, of the cells. In other words, the number of initially attached (successfully seeded) cells at day 1 was likely the most influential factor of cell numbers at days 3 and 5. The lower proliferation rate of PLA/6hAT/nHA compared to the other groups might be a result of the cells reaching confluency sooner, thus slowing their growth

30

## 2.5    Summary of the current method

In summary, nano-hydroxyapatite was successfully coated on 3D printed, alkali-treated polylactic acid scaffolds, and 6-hour alkali treatment reduced strut width and mechanical properties, while improving the nHA coating and hydrophilicity. More importantly, effective modulus of PLA/6hAT/nHA was not reduced compared to the non-alkali-treated, nHA coated scaffolds (PLA/nHA). Furthermore, in vitro experiments showed that the combined 6hAT/nHA modification improved cell adhesion, resulting in the highest cell counts at days 1, 3, and 5. In conclusion, the simple methods of alkali treatment and nHA coating effectively modified 3D printed PLA scaffolds, which may be advantageous for cancellous bone regeneration. Through this study, the long alkali treatment time was detrimental to the structure of PLA scaffold. However, the strut width of 3D printed PLA was significantly reduced after 6-hour alkali treatment, which leads to the damped mechanical properties. Therefore, to avoid the over-hydrolysis and shorten the treatment time, PLGA is selected as alternative polyester due to its higher intrinsic hydrophilicity in the future study.

## 2.6    Results for the alternative approach

### 2.6.1    Thermal properties of purchased PLGA

Unlike the commercial PLA, there are no standardized parameters for 3D printing a specific PLGA. Thermal analysis (DSC and TGA) was first introduced to predict the safety and reasonable range of the printing temperature. Poly(D, L-lactide-co-glycolide) (PLGA, LA:GA=75:25, MW=156 kD) with ester end-group was purchased from LACTEL® Absorbable Polymers (Birmingham, AL, USA). To determine the potential temperature range prior to thermal plastic 3D printing, a differential scanning calorimeter (DSC) and thermogravimetric analysis

31

(TGA) were employed. According to DSC curve, $T_g$ of PLGA was ranging from 42.9 to 47.2 °C and $T_m$ was 51.2 °C. The TGA curve revealed that the mass percentage start to decrease drastically at 244.5 °C, which potentially because of the beginning of material degradation. Therefore, the safety range of printing PLGA was 47.2 - 244.5 °C. (**Figure 2.9**) The printing parameters selected were shown in **Table 2.7**.
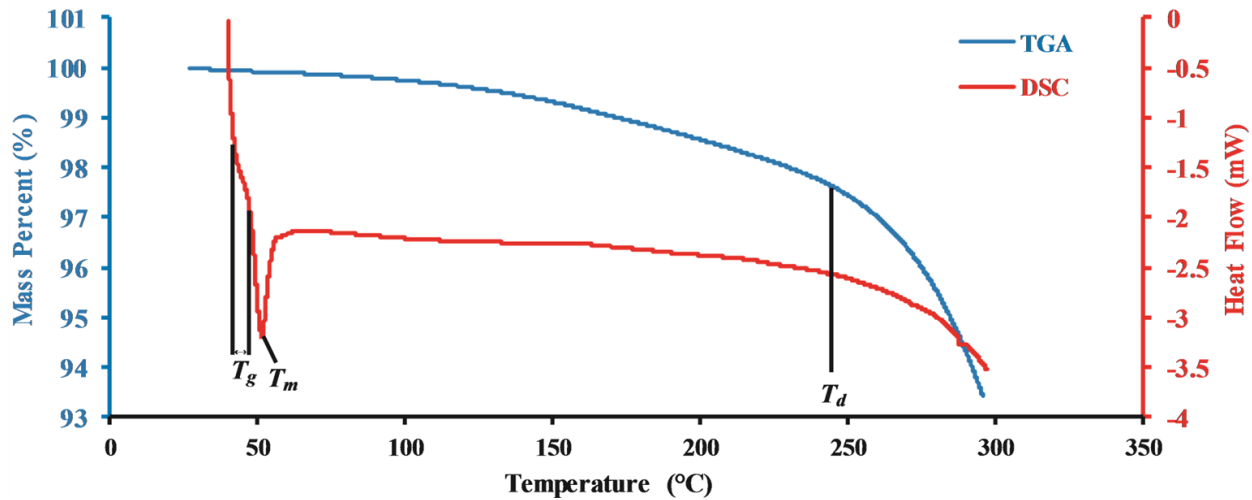


Figure 2.9    The glass transition temperature ($T_g$), melting point ($T_m$), and decomposition temperature ($T_d$) measured.

Table 2.7    Printing parameters for printing PLGA scaffold.

| Printing parameters | Value |
|---|---|
| Temperature | 145 °C |
| Pressure | 160 kPa |
| Printing speed | 2 mm/s |
| Nozzle diameter | 0.2 mm |
| Layer thickness | 0.2 mm |
| Strut width | 0.2 mm |
| Pre-flow | 1000 ms |
| Post-flow | 200 ms |

### 2.6.2 Characterization of global structures and surface morphologies

The global images displayed similar in structures among all the groups in the large images of **Figure 2.10**. Although without quantification of strut width, the strut widths of PLGA/1hAT and PLGA/ were notably decreased compared to non-treated PLGA. In terms of surface images, among the non-nHA coated groups, wrinkle(s) appeared on the surface images of PLGA/1hAT and much more on PLGA/2hAT, while PLGA showed a total smooth surface. According to the nHA coated groups, despite there was no visible difference between PLGA/nHA and PLGA/1hAT/nHA, PLGA/2hAT/nHA seemed to present the highest amount of nHA coating.
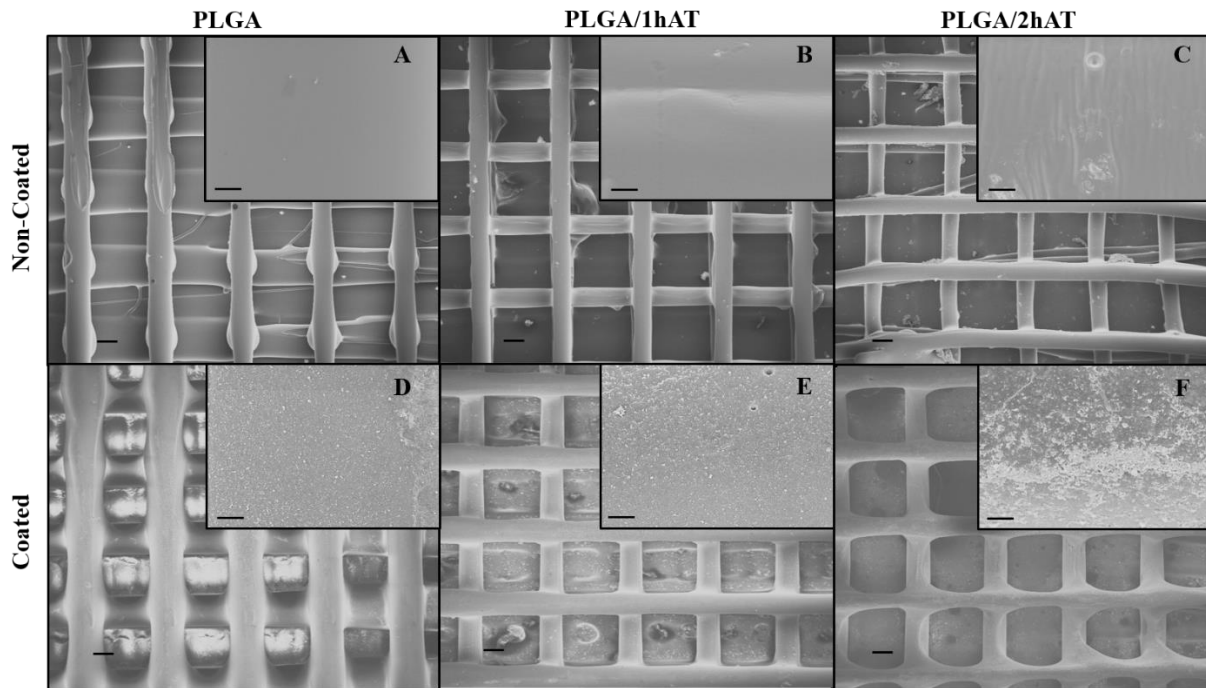


Figure 2.10   (A-C) Non-coated PLGA scaffolds and (D-F) nano-hydroxyapatite coated PLGA scaffolds. (E-F, insets)

The effect of AT time on extent of nHA coating is visible. Large images, scale bar = 200 µm. Inset images, scale bar = 10 µm.

33

### 2.6.3 Characterization of surface chemistry

The element map (**Figure 2.11**) of calcium on nHA coated surfaces revealed that the most nHA particles were found in PLGA/2hAT/nHA while there was no obvious difference between PLGA/nHA and PLGA/1hAT/nHA. Since the 1hAT has limited capability of modifying PLGA surface and improving nHA coating compared to 2hAT, PLGA/1hAT/nHA will not proceed to the following evaluations.
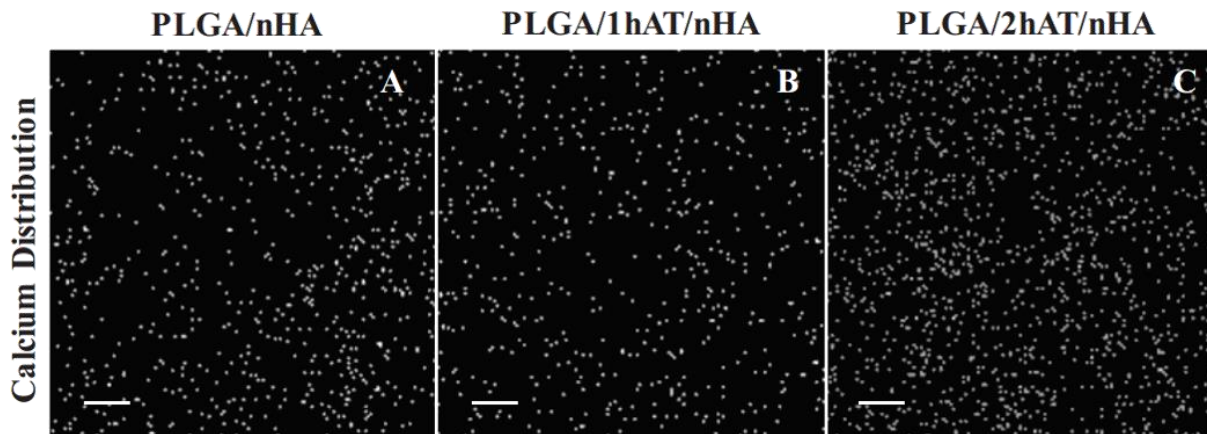


Figure 2.11    The element maps of calcium on the surface of (A) PLGA/nHA, (B) PLGA/1hAT/nHA, and (C) PLGA/2hAT/nHA. Scale bar = 10 µm.

### 2.6.4 Water contact angle analysis

WCA of PLGA, PLGA/2hAT, PLGA/nHA, and PLGA/2hAT/nHA were reduced in the following trend: $123.4° \pm 14.5° > 109.4° \pm 8.4° > 96.80° \pm 24.4° > 51.87° \pm 13.3°$ (**Figure 2.12**), although PLGA/2hAT was not significantly higher than PLGA/nHA. PLGA/2hAT/nHA was the only hydrophilic surface. The one-way ANOVA also suggested that pretreatment with AT positively affects the attachment of the nHA coating, based off the significant (*p=0.0240*) difference between the PLGA/nHA and PLGA/2hAT/nHA surfaces.

34
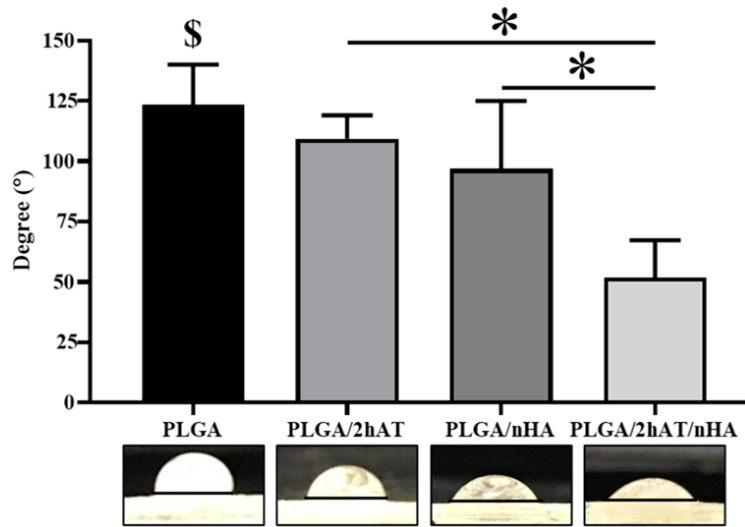
Figure 2.12    Water contact angle for all the groups. $p<0.05 compared to all groups. *p<0.05 pairwise comparisons as indicated. (n=5).

## 2.7    Discussion of the modified method

In this study, the thermal properties of PLGA were studied. Since the molecule weight ($M_w$) and ratio of LA:GA might influence the thermal properties of PLGA[153] and theses data were unique for the PLGA used in this study, the thermal properties needed to be investigated. Moreover, the appropriate printing temperature needs to be higher than $T_g$ and lower than $T_d$ to achieve successful print and to prevent thermal degradation of the material. Therefore, prior to the printing process, DSC and TGA were performed to collectively determine the potential range of printing temperature. In a systematic study of 3D printing PLGA,[154] Tg of PLGA with LA:GA of 85:15 and $M_w$ of 62 kD was around 57 ℃, while it decreased to around 42℃ for PLGA with LA:GA of 60:40 and $M_w$ of 42 kD. $T_g$ (42.9 to 47.2 ℃) of PLGA in this study was at the middle of these two values, which potentially because of the 75:25 ratio of LA: GA. On the contrary, the high $M_w$ (156 kD) showed insufficient improvement on $T_g$, which was contradictory to the

35

conclusion that $T_g$ strongly rely on $M_w$[154]. Overall, the final printing temperature shown in Table 1 (145 ℃) was able to print PLGA meanwhile prevent thermal decomposition.

The global structures of different groups were consistent except for the second layer of PLGA and both layers of PLGA/nHA. The strut width of PLGA/nHA was seemed to be thicker than PLGA, which potentially indicated the nHA coating increased the strut width. However, by comparing the surface SEM images of **Figure 2.10D** and **Figure 2.10E**, there was no significant difference in the nHA coating density and the strut width of PLGA/1hAT/nHA was not significantly increased compared to PLGA/1hAT. Thus, the ticker struts in PLGA and PLGA/nHA were possibly resulted from printing issues, instead of nHA coating. Among the surface SEM images, wrinkles started to form on the PLGA/1hAT surface and stacked more regularly on PLGA/2hAT while PLGA showed total smooth surface. The similar wrinkles were also found on poly lactic acid (PLA) mesh treated by ammonia solution (pH=12) for 1 hour.[86] This was possibly due to the accumulated hydrolysis of the carbon backbone of polymer molecules,[84] and became more noticeable with the increase of treatment time. More importantly, the hydrolysis process unlocked carbons from molecule chains and introduced hydroxyl functional groups on PLGA surface, which might provide suitable binding sites of nHA particles. Nevertheless, the nHA coating seemed to have no significant differences in PLGA/1hAT/nHA and PLGA/nHA, while PLGA/2hAT/nHA showed the best coating among all the groups. The element maps of calcium verified this result that the calcium density was apparently the highest, whereas 1hAT did not show the capability of attracting more nHA particles to adhere. Hence, in the comparison of 1hAT, 2hAT might provide superior surface conditions for nHA coating.

Hydrophilicity was one of the critical surface conditions that affected the practical application of tissue engineering scaffold.[155] The effects of AT and nHA on WCA indicated that

36

both AT and nHA improved the wettability of the PLGA surface individually, and the combination of both modifications further improved the wettability. Although the WCA of PLGA/2hAT was significantly lower than PLGA, the trend of decrease was less promising than PLGA and PLGA/2hAT/nHA. Additionally, the WCA of PLGA/nHA was not significantly lower than PLGA/2hAT, which indicated that the modification quality was similar between 2hAT and nHA. Thus, nHA coating was only demonstrated the best surface modification of hydrophilicity with the presence of 2-hour alkali treated PLGA surface. This finding verified the SEM surface images that PLGA/2hAT/nHA showed the best nHA coating. On the other hand, the positive effect of 2hAT on PLGA surface and nHA coating confirmed that the extra carboxyl functional groups were successfully formed on PLGA surface, which consequently attracted more nHA molecules to adhere. Similar result was also reported on PLA surface,[86] since the hydrogens from hydroxyl functional groups were likely substituted by $Ca^{2+}$ to form $R\text{-COO-}Ca^{2+}$ via the ionic interactions between PLA and nHA. Therefore, the PLGA/2hAT/nHA surface displayed the optimal surface modification.

## 2.8    Summary of the modified method

The selected printing temperature can produce a repeatable scaffold while preventing thermal decomposition of the material. Therefore, DSC and TGA may be needed as an initial evaluation for determining the printing temperature prior to 3D printing of materials with unknown thermal properties. The SEM images and WCA suggest that 2hAT/nHA is the optimal surface modification. During the hydrolysis in ammonia solution, the hydroxyl and carboxyl functional groups are sufficiently introduced, and therefore, more nHA particles are adhered compared to 1hAT and as-printed PLGA scaffold. Thus, to achieve effective surface modification for PLGA, the alkali treatment time was reduced to 2 hours compared to 6 hours for PLA scaffold, while the

37

2hAT process was still detrimental to the struts, which might counteract the efficacy of alkali treatment. Therefore, the main focus of the next study should move to an alternative surface treatment method that induces sufficient modifications and is material friendly.

# 3D PRINTING OF PLGA-NHA COMPOSITE SCAFFOLD FOR MODIFYING MECHANICAL PROPERTIES

So far, nHA particles have been immobilized on PLA or PLGA surface through AT. Although nHA improved the surface conditions and showed superior biological properties, because of the nature of coating, the capability of nHA affecting mechanical properties is limited. Thus, gaps still exist in the study that if the biological and mechanical properties can be both improved significantly by 3D printing PLGA/nHA composite (doping nHA in PLGA matrix). The *objectives* of Aim II are to investigate: (i) the thermal properties of PLGA/nHA composite material before and after printing, (ii) the size and distribution of nHA particles in PLGA matrix, (iii) the mechanical properties of PLGA/nHA composite scaffold, (iv) the influence of nHA filler on PLGA/nHA composite scaffold's physical and mechanical properties, and (v) the biological properties of the PLGA/nHA scaffold. It is *hypothesized* that: (i) the doped nHA will be randomly distributed and will enhance the thermal and mechanical properties of the PLGA matrix, and (ii) the addition of nHA will improve the surface conditions, and biological properties of the 3D printed PLGA/nHA composite scaffold.

## 3.1    Rationale

Nano-sized HA blended polyester scaffold have demonstrated the improved mechanical properties. However, the blending method of PLGA-nHA and the printability of PLGA and nHA were remained unclear. Therefore, it is necessary to verify the capability of nHA blending in the

3D printed PLGA matrix through 1,4-dioxane dissolving. To this end, Aim II will investigate: (i) the printability of PLGA-nHA composite scaffold with DSC, (ii) thermo-stability of PLGA-nHA composite with TGA, (iii) the size and distribution of nHA particles in PLGA matrix, (iv) the mechanical properties of PLGA/nHA composite scaffold, (v) the study of *in vitro* cell behavior on PLGA-nHA composite scaffold. To validate the efficacy of the nHA particles mixed in PLGA matrix as the filler in 3D printed composite scaffold, it is hypothesized that (i) 1,4-dioxane will not induce differences in the thermal properties after the mixing process, (ii) the thermal stability of PLGA/nHA will be stable prior to and after printing, (ii) the size of nHA particles will be smaller than 200nm, (iii) nHA particles can be randomly distributed in PLGA matrix, (iv) the surface roughness of PLGA-nHA will be higher than PLGA, (iv) the effective Young's modulus of PLGA/nHA composite scaffold will be improved compared to PLGA, (v) the outcomes of cell adhesion, proliferation, and differentiation will be superior on PLGA/nHA to PLGA.

## 3.2    Experimental approach and data analysis
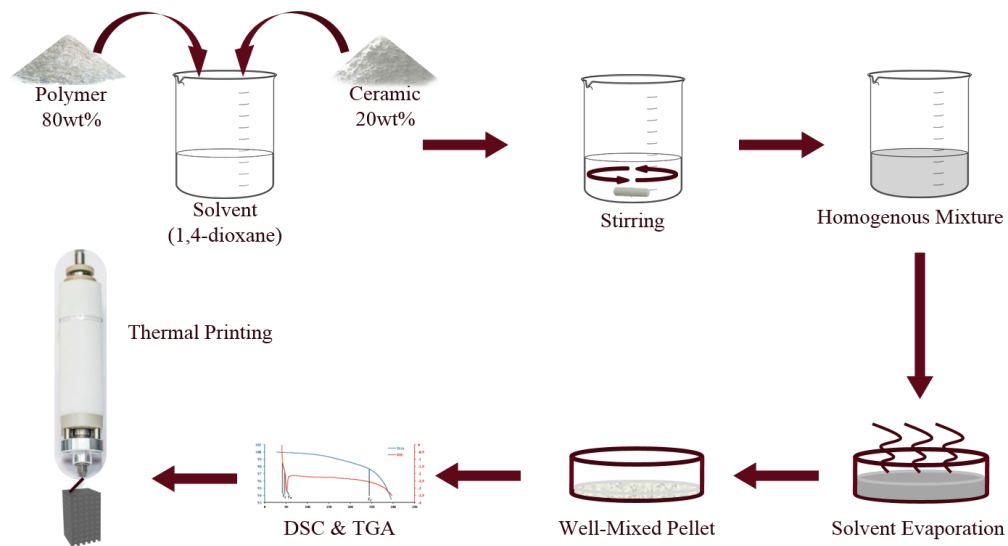


Figure 3.1    The preparation and 3D printing of PLGA-nHA composite scaffold.

Table 3.1    The thermal properties will be investigated by DSC

| Experimental groups | Structure | Mass | Sample size |
|---|---|---|---|
| PLGA | Pellet | 5-10 mg | n=3 |
| PLGA-nHA | | | n=3 |

Table 3.2    The thermal properties will be investigated by TGA

| Experimental groups | Structure | Mass | Sample size |
|---|---|---|---|
| PLGA | Pellet | 5-10 mg | n=3 |
| PLGA-nHA | | | n=3 |

Table 3.3    The global/surface morphologies and cross-sectional area of PLGA/nHA scaffold were observed under SEM.

| Experimental groups | Structure | Dimensions | Sample size |
|---|---|---|---|
| PLGA | Scaffold | 7×7×2.2 mm | n=1 |
| PLGA-nHA | | | n=1 |

Table 3.4    The analysis of nHA particle size and distribution were analyzed based on SEM cross-sectional images processed by ImageJ software (particle analysis and NND plugin tool)

| Experimental groups | Structure | Dimensions | Sample size (struts) | Sample size (locations) |
|---|---|---|---|---|
| PLGA | Scaffold | 7×7×2.2 mm | n=1 | n=3 |
| PLGA-nHA | | | n=1 | n=3 |

Table 3.5    The surface chemistries will be analyzed by EDX and FTIR.

| Experimental groups | Structure | Dimensions | Sample size (struts) | Sample size (locations) |
|---|---|---|---|---|
| PLGA | Scaffold/Solid plate | 7×7×2.2 mm | n=1 | n=3 |
| PLGA-nHA | | | n=1 | n=3 |

41

Table 3.6    The hydrophilicity will be measured from water contact angle processed by ImageJ software.

| Experimental groups | Structure | Dimensions | Sample size |
|---|---|---|---|
| PLGA | Solid plate | 7×7×2.2 mm | n=5 |
| PLGA-nHA | | | n=5 |

Table 3.7    The stiffness and effective Young's modulus will be measured from compression testing.

| Experimental groups | Structure | Dimensions | Sample size |
|---|---|---|---|
| PLGA | Scaffold | 8×8×4 mm | n=8 |
| PLGA-nHA | | | n=8 |

Table 3.8    The in vitro cell behaviors will be analyzed by CCK-8, Phalloidin/DAPI staining, and ALP assay.

| Experimental groups | Structure | Dimensions | Sample size |
|---|---|---|---|
| PLGA | Scaffold | 7×7×2.2 mm | n=10 |
| PLGA-nHA | | | n=10 |

## 3.3    Results

### 3.3.1    Characterization of global structure, surface morphologies, and cross-sectional morphologies

The sphere shaped nHA particles were found fully spread in PLGA matrix from the top and the cross-sectional view of the 3D printed PLGA-nHA struts, while no nHA particles were found in PLGA strut (**Figure 3.2**). There were 1,050 nHA particles in the SEM image were defined in ImageJ software with boundaries by the range of the particles' diameters (0.04-0.2µm) with a binary mode (threshold = 18.93%). The diameter distribution of nHA particle (**Figure 3.3A**) showed that 98.6% of the particles were below 200nm, which was consistent to the information provided by the vendor (particle size < 200nm, Sigma Alderich). More importantly, only 1.4% of

42

the particles were larger than 200nm, indicating the agglomerations of nHA particles were well controlled during the stirring process of the PLGA-nHA mixture. The Nearest neighbor distance (NND) analysis was performed by the NND plugin tool in ImageJ. The scatter plot of the NND analysis (**Figure 3.3B**) revealed a weak correlation ($R^2 = 0.00385$) between the NND and the distance between particles and the top boundary of the image, and the slop of the trendline was near zero (0.00196). Therefore, the NND and the location of the nHA particles could be treated independent. Collectively, nHA particles in PLGA-nHA composite was randomly distributed based on the one sample observation, while more samples were expected to be fabricated and observed to further confirm the uniformity of nHA particle distribution. Additionally, to optimize the evaluation of mechanical reinforcement of nHA, different nHA percentage (e.g. 5%, 10%, 20%, and 30%) in the PLGA matrix can be assessed such that the PLGA-nHA with the highest mechanical properties will be unveiled and proceeded with the following observations and evaluations.
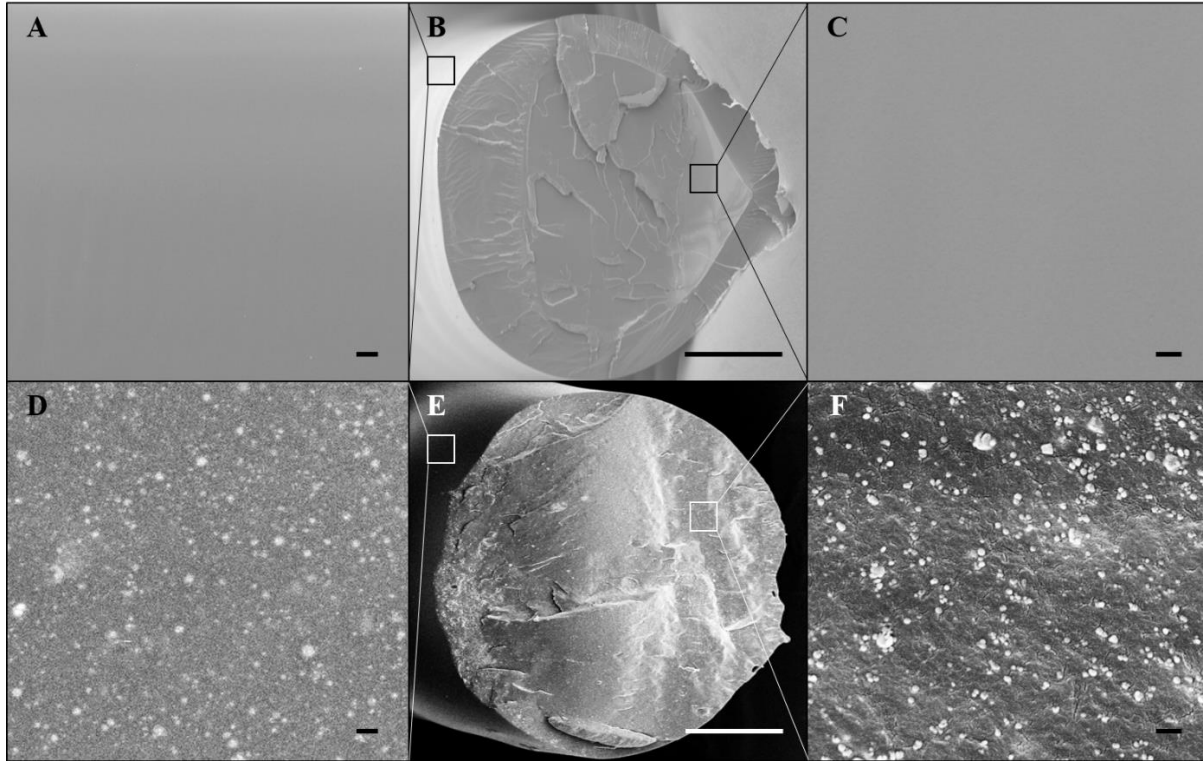
Figure 3.2    The SEM images of (A-C) top view, the cross-sectional view, the higher magnification of cross-sectional view of a PLGA strut.

The SEM images of (D-F) top view, the cross-sectional view, the higher magnification of cross-sectional view of a PLGA/nHA composite strut. Scale bar of (A) and (D) =2µm. Scale bar of (B) and (E) = 100µm. Scale bar of (C) and (F) =500nm.
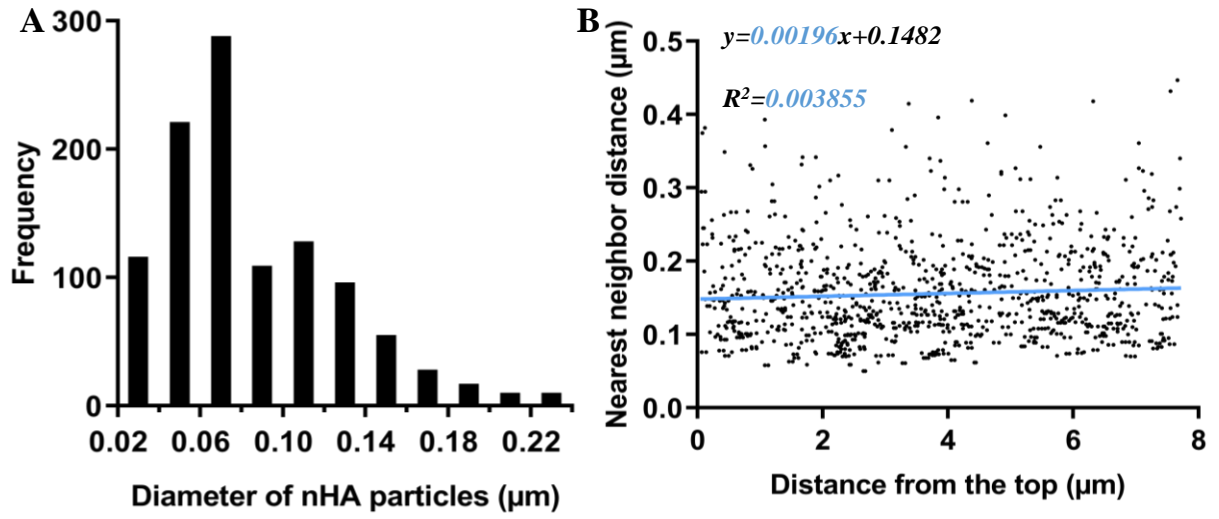
Figure 3.3    (A) The distribution frequency of nHA particles diameters. (B) the nearest neighbor distance of nHA particles distributed in PLGA matrix.

EXPLORE POLYDOPAMINE INDUCED NHA COATING ON 3D PRINTED PLGA

SCAFFOLDS

## 4.1    Rationale

To explore the non-destructive methods of surface modification, poly-dopamine replaces ammonia solution as a new approach to modify the PLGA surface. Recently, polydopamine (pDA) coating, a derivative idea from mussel-adhesion mechanism, has been leveraged a simple and effective approach for surface modification of biomaterials for bone tissue engineering without being detrimental to the bulk structure. Although the results from Aim I showed that 2-hour alkali treatment successfully modified the PLGA surface and promoted nHA deposition, the strut width was reduced, even with shortened treatment time (compared to that of PLA). Thus, surface modification of PLGA will be performed via intermediary polydopamine (pDA) coating.

Despite the mentioned advantages of polydopamine treatment, the coating processing is very time consuming (typically longer than 12 hours) and the coating thickness is generally limited to nanometers (e.g. 45-80 nm).[156,157,158] Since the pH and temperature of the solution environment are critical, and these parameters can be used to modify the thickness and morphology of the pDA coating. To our knowledge, the highest pDA coating thickness observed with traditional solution deposition was 187.2 nm, obtained by adjusting the pH to the range from 9 to 10.2 under room temperature.[159] When the temperature was increased to 60°C and the pH lowered to 8.5, a comparable thickness of 176 nm was achieved.[160] Nevertheless, surface nano-structures have

46

resulted in less cell adhesion and proliferation than micro-structures,[161] and have demonstrated less efficacy in enhancing cell-material interactions compared to the combination of nanoscale and microscale features.

Although polydopamine coating has been shown to be an effective method to modify polymer surfaces, the thickness of the pDA coating was limited with the traditional method (pH=8.5, 10mM Tris-HCl, room temperature).[162] Therefore, enhancing the coating speed could significantly improve the coating thickness. Increasing the dopamine concentration to 8 mg/mL has been reported to greatly increase the coating thickness to 80 nm (20 nm/h), and no further improvement was obtained with higher concentrations.[158,159] Metal ions and hydrogen peroxide have also been shown to serve as oxidants in the dopamine solution to catalyze the coating growth to 43 nm/h.[163] Meanwhile, adjusting the oxidant/dopamine ratio and raising the temperature has improved the coating speed to $90 \pm 5$ nm/h.[164] The highest reported pDA coating speed was 339 nm/h, obtained by treating the substrate with sulfuric acid/sodium sulfate gas in a 300°C nitrogen environment.[165] An increase in the non-oxidized monomer dopamine has demonstrated positive effects on the pDA coating thickness.[166,167] Another similar point agrees to this that the formation of pDA coating mainly occurred to the intermediates in the early stage of dopamine oxidation.[168] When pDA-based surface modification was developed a decade ago, the dopamine monomers were typically first polymerized on the substrate to form the pDA coating, and the secondary bioactive particles (e.g., HA, bone morphogenetic protein-2 (BMP-2) were subsequently introduced onto the pDA coating.[95,134,110,169,170,171] However, this sandwich structure of "substrate—pDA coating—bioactive coating," wherein only the secondary/top-layer coating material is exposed to the outer environment, may restrict the exposure of pDA on the surface of the biomaterial, hindering the intrinsic benefits of pDA for promoting cell-material interactions.

47

In this study, to enhance the exposure of pDA coating and thus the immobilization of nHA particles on the PLGA surface, nHA was mixed with dopamine *during* the polymerization process, such that the nHA particles would be exposed to more catechol and amine groups throughout the coating formation than the traditional layer-wise coating (e.g. nHA onto pDA). Using this novel method, both pDA and nHA could synergistically enhance the surface properties of the 3D printed PLGA substrate. Toward this end, the efficacy of the pDA-induced nHA (pDA-nHA) coating was assessed through observation of surface morphology and chemistry, hydrophilicity, mechanical properties, and *in vitro* cell attachment and proliferation. Therefore, Instead of immobilizing nHA on pDA treated surface, in this study, the nHA particles and dopamine monomers will be mixed simultaneously for the surface modification to maximize the interactions between the dopamine monomers, nHA particles, and substrate surface. (**Figure 4.1**) The *objectives* of this aim are to investigate: (i) the influence of pDA modification on strut width of 3D printed PLGA scaffold, (ii) the chemical interactions between pDA and nHA coating through EDX and FTIR, and (iii) the hydrophilicity of pDA-nHA coated PLGA scaffold. It is *hypothesized* that: (i) the surface modification of pDA and pDA-nHA coating will not alter PLGA strut width, and (ii) the presence of pDA will enhance the amount of nHA immobilized on the PLGA surface and the hydrophilicity over PLGA/nHA without pDA.

48

## 4.2 Experimental approach and data analysis
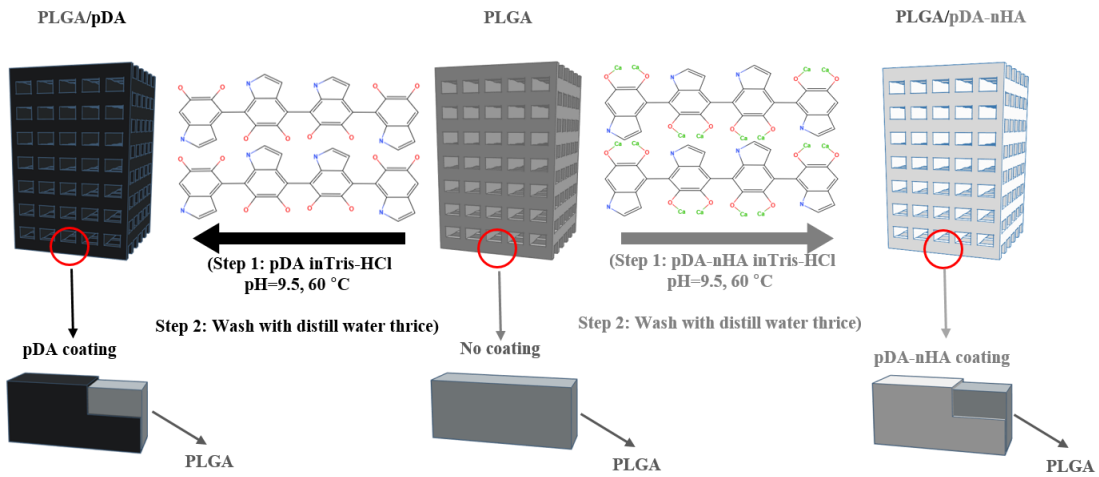


Figure 4.1    The mechanism of pDA and pDA-nHA coating on PLGA substrate scaffold.
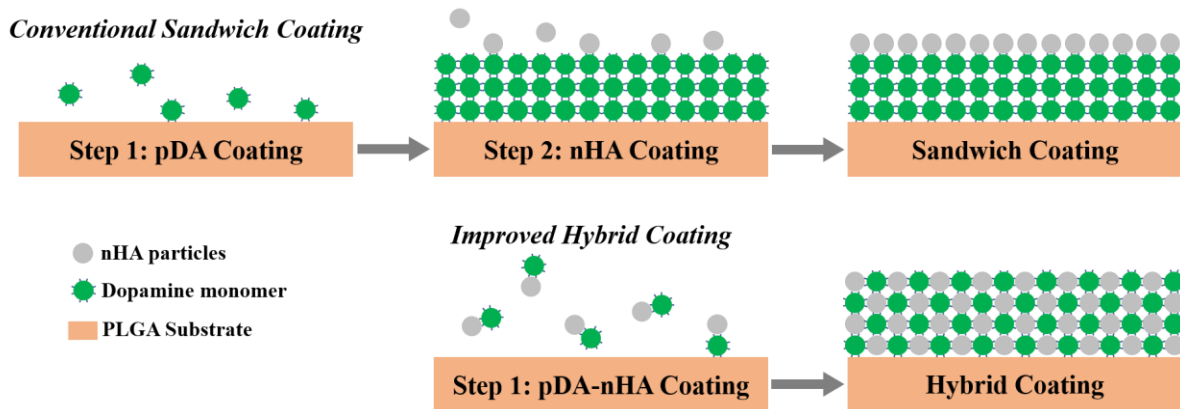


Figure 4.2    The comparison of the conventional sandwich coating and the improved hybrid coating.

Table 4.1    The global structure/surface morphologies of scaffold were characterized by SEM.

| Experimental groups | Structure | Dimensions | Sample size |
|---|---|---|---|
| PLGA | | | n=1 |
| PLGA/nHA | Scaffold | 7×7×2.2 mm | n=1 |
| PLGA/pDA | | | n=1 |
| PLGA/pDA-nHA | | | n=1 |

Table 4.2    The cross-sectional area of scaffold was characterized by SEM.

| Experimental groups | Structure | Dimensions | Sample size (Struts) | Sample size (locations) |
|---|---|---|---|---|
| PLGA | | | n=3 | 10<n<20 |
| PLGA/nHA | Scaffold | 7×7×2.2 mm | n=3 | 10<n<20 |
| PLGA/pDA | | | n=3 | 10<n<20 |
| PLGA/pDA-nHA | | | n=3 | 10<n<20 |

Table 4.3    The surface chemistry was characterized by EDX.

| Experimental groups | Structure | Dimensions | Sample size (Struts) | Sample size (locations) |
|---|---|---|---|---|
| PLGA | | | n=3 | n=5 |
| PLGA/nHA | Scaffold | 7×7×2.2 mm | n=3 | n=5 |
| PLGA/pDA | | | n=3 | n=5 |
| PLGA/pDA-nHA | | | n=3 | n=5 |

Table 4.4    The surface chemistry was characterized by FTIR.

| Experimental groups | Structure | Dimensions | Sample size |
|---|---|---|---|
| PLGA | | | n=1 |
| PLGA/nHA | Solid plate | 7×7×2.2 mm | n=1 |
| PLGA/pDA | | | n=1 |
| PLGA/pDA-nHA | | | n=1 |

50

Table 4.5    The hydrophilicity was measured by water contact angle.

| Experimental groups | Structure | Dimensions | Sample size |
|---|---|---|---|
| PLGA | | | n=5 |
| PLGA/nHA | Solid plate | 7×7×2.2 mm | n=5 |
| PLGA/pDA | | | n=5 |
| PLGA/pDA-nHA | | | n=5 |


Table 4.6    The cell proliferation was assessed by CCK-8 assay.

| Experimental groups | Structure | Dimensions | Sample size |
|---|---|---|---|
| PLGA | | | n=4 |
| PLGA/nHA | Solid plate | 7×7×2.2 mm | n=4 |
| PLGA/pDA | | | n=4 |
| PLGA/pDA-nHA | | | n=4 |


Table 4.7    The cell viability was assessed by live/dead assay.

| Experimental groups | Structure | Dimensions | Sample size |
|---|---|---|---|
| pDA-extract on day 1 | | | n=3 |
| pDA-extract on day 3 | Solid plate | 7×7×2.2 mm | n=3 |
| pDA-extract on day 5 | | | n=3 |


## 4.3    Results

### 4.3.1    Characterization of global structure and surface morphologies

The struts of the scaffolds were consistently fabricated via fused deposition modeling. As expected, the strut width was not changed after pDA modification. (**Figure 4.3**) Even the thin strings and other residues produced by nozzle movement on the surface were still existed, indicating that pDA modification was not detrimental to the PLGA substrate even with 12-hour treatment time.  Regarding surface microstructure, the PLGA/pDA surface appeared rougher, with full coverage of the polymerized dopamine, compared to the smooth PLGA surface. A few nHA

51

particles were found randomly distributed on PLGA/nHA surface, while the surface of PLGA/pDA-nHA was covered fully and evenly.
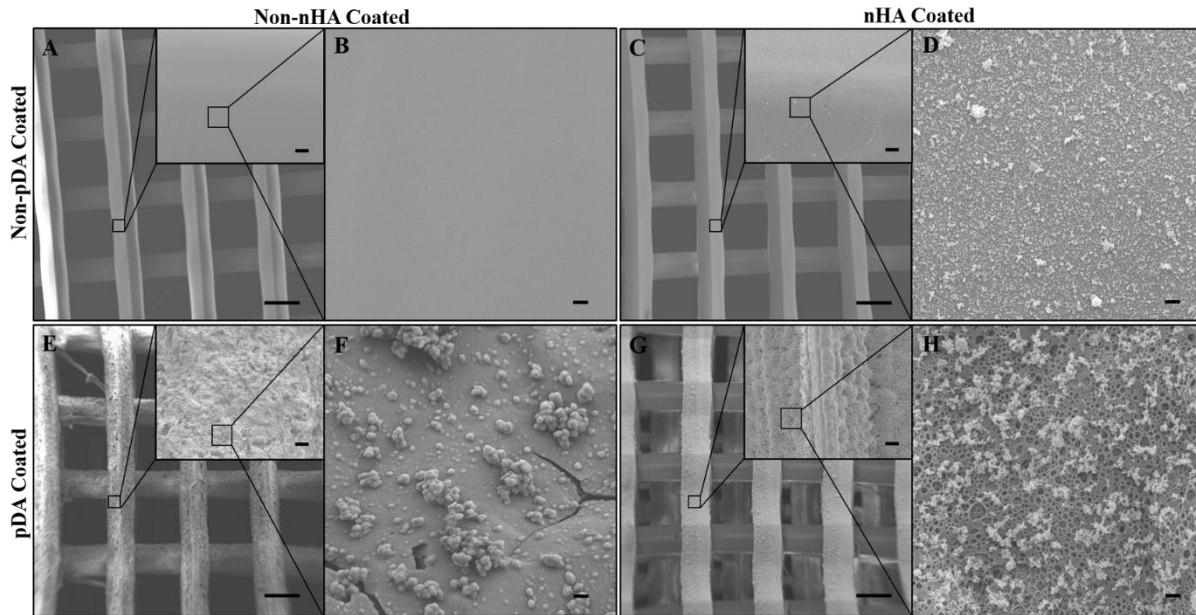


Figure 4.3    (A) PLGA scaffold, (B) Surface view of PLGA scaffold, (C) PLGA/nHA scaffold, (D) Surface view of PLGA/nHA scaffold, (E) PLGA/PDA scaffold, (F) Surface view of PLGA/PDA scaffold, (G) PLGA/PDA-nHA scaffold, (H) Surface view of PLGA/PDA-nHA scaffold.

Scaffold global view images (27X), scale bars = 500µm. Inset images (500X), scale bars = 20µm. Surface view images (5000X), scale bars = 1µm.

### 4.3.2    Evaluation of coating growth and thickness

No measurable coating thickness was obtained from PLGA and PLGA/nHA surfaces. Surprisingly, on the surface of PLGA/pDA, a porous layer of coating with a thickness of $17.22 \pm 3.56$ µm (1435 nm/h) was measured; and a $22.11 \pm 2.91$ µm (1842 nm/h) coating layer of pDA and nHA was found on the surface of PLGA/pDA-nHA, which was significantly thicker than that of PLGA/pDA. Interestingly, the coating morphology resembled cancellous bone-like porous

52

structures, with some larger pores (~microns) found within the PLGA/pDA-nHA coating. (**Figure 4.4**)
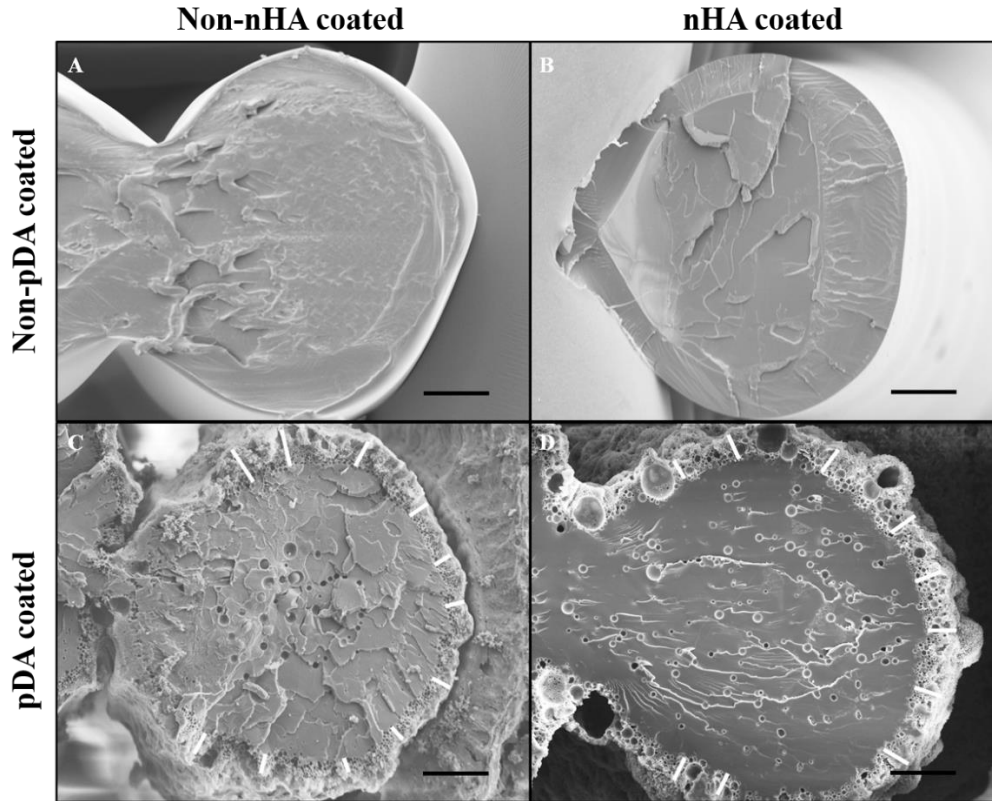


Figure 4.4    Cross-sectional view of a single strut from (A) PLGA scaffold, (B) PLGA/nHA scaffold, (C) PLGA/PDA scaffold, (D) PLGA/PDA-nHA scaffold.

White bars in C and D indicate the PDA and PDA-nHA coating. Scale bars (300X)= 50µm.

### 4.3.3    Investigation of surface chemistry

The EDX results (**Table 4.8**) showed that the weight percentage of carbon in PLGA was significantly lower than that in PLGA/pDA ($p<0.01$), while the oxygen in PLGA was higher than that in PLGA/pDA ($p<0.01$). The amount of calcium and phosphorous in PLGA/pDA-nHA was significantly higher than those in PLGA/nHA ($p<0.01$). The FTIR spectra (**Figure 4.5**) provide

supportive information for the pDA and nHA coatings. A broad stretching band of 3100 $cm^{-1}$ to 3600 $cm^{-1}$ indicated the existence of N-H and O-H on PLGA/pDA and PLGA/pDA-nHA. More importantly, aromatic C=C and C=N were observed in the range of 1500 $cm^{-1}$ to 1610 $cm^{-1}$. Both findings provided evidence that pDA was successfully coated. A peak of P=O at 1020 $cm^{-1}$ for PLGA/pDA-nHA confirmed the nHA in the coating layer.

Table 4.8     The percentage of carbon, oxygen, calcium, and phosphorus (%). [*]$p<0.01$ compared to PLGA, [$]$p<0.01$ compared to PLGA/nHA.

| Elements | PLGA | PLGA/nHA | PLGA/pDA | PLGA/pDA-nHA |
|---|---|---|---|---|
| C | $47.51 \pm 0.14$ | $44.45 \pm 0.12$ | $49.21 \pm 0.35$[*] | $45.44 \pm 0.72$ |
| O | $52.49 \pm 0.14$ | $53.27 \pm 0.11$ | $50.79 \pm 0.35$[*] | $50.92 \pm 0.65$ |
| Ca | 0.00 | $1.33 \pm 0.08$ | 0.00 | $2.47 \pm 0.36$[$] |
| P | 0.00 | $0.95 \pm 0.10$ | 0.00 | $1.49 \pm 0.18$[$] |
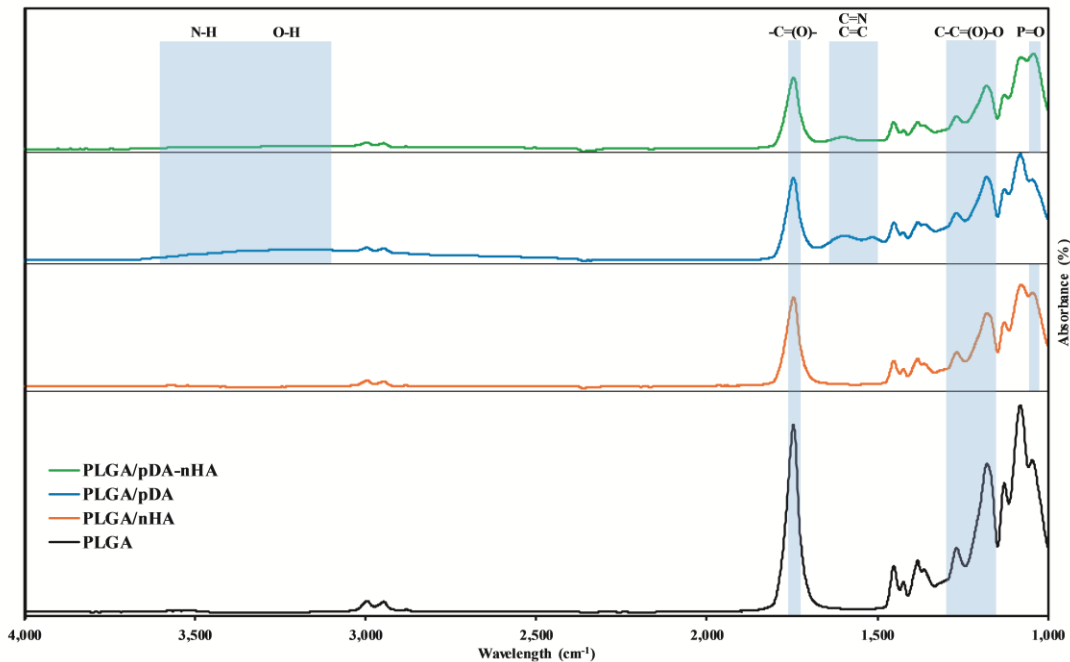


Figure 4.5     The FTIR spectra (absorbance). The pDA coating was confirmed with the wide bands of N-H/O-H and C=N/C=C in PLGA/PDA and PLGA/pDA-nHA. A noticeable peak of P=O (presumably nHA) was found in PLGA/pDA-nHA and PLGA/nHA.

54

### 4.3.4 Water contact angle analysis

The WCA (**Figure 4.6**) was significantly reduced in the following order: PLGA, PLGA/nHA, PLGA/pDA, and PLGA/pDA-nHA (all pairwise comparisons, $p<0.0001$), with values of $108.6 \pm 5.9º > 70.7 \pm 3.6º > 42.9 \pm 1.8º > 26 \pm 2.6º$, respectively. All the groups except for PLGA exhibited hydrophilic surfaces.
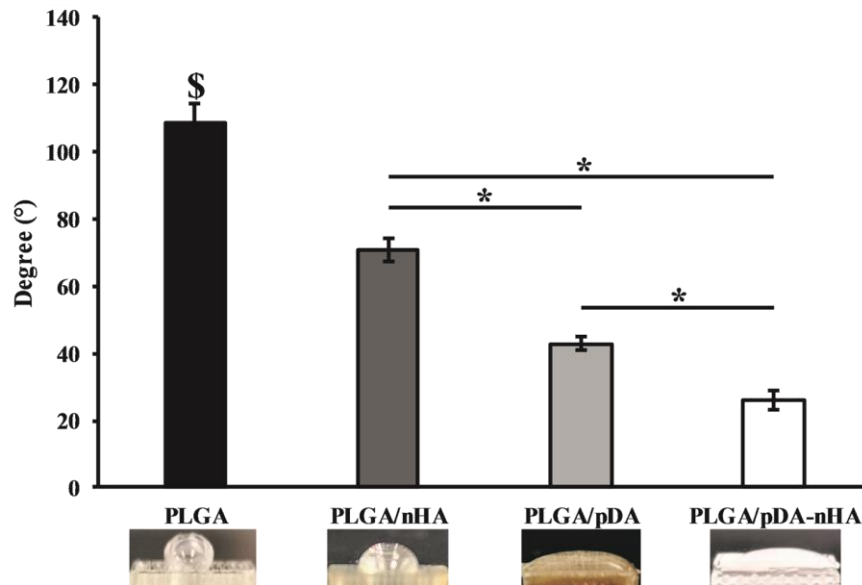


Figure 4.6    Water contact angle. $p<0.0001$ compared to all groups. *$p<0.0001$ pairwise comparisons as indicated. (n=5).

### 4.3.5 Cell proliferation assay

Moreover, the proliferation of MC3T3 cells on PLGA/pDA and PLGA/pDA-nHA was significantly lower than PLGA and PLGA/nHA on day 1 and day 3. (**Figure 4.7**) Accordingly, all cells were dead in pDA treated PLGA substrates on day 5. The chances are that pDA was overdosed on PLGA scaffold so that it is beyond the cytotoxicity threshold.
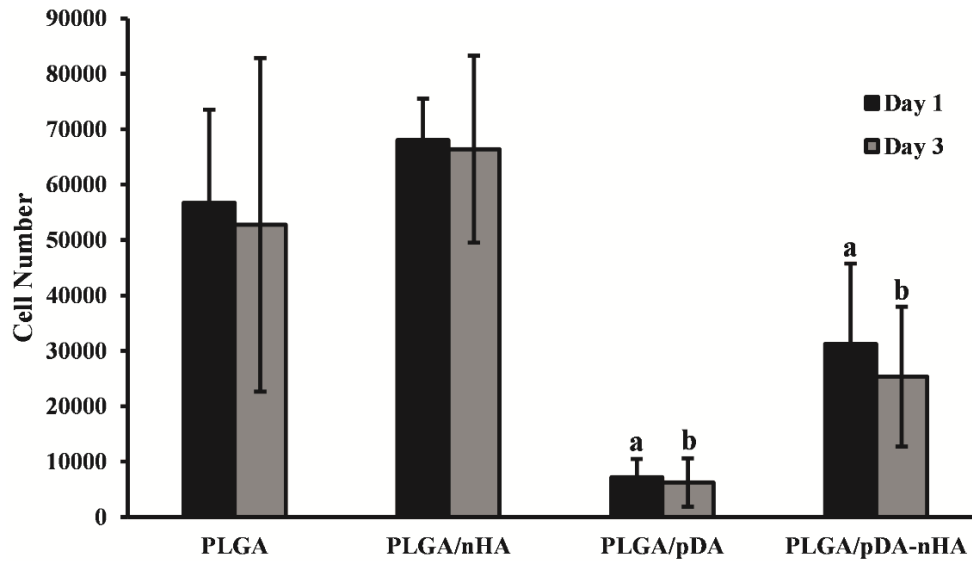
Figure 4.7     Pilot CCK-8 assay for PLGA, PLGA/nHA, PLGA/pDA, and PLGA/pDA/nHA.

"a" denotes significantly higher or lower compared to other treatment on day 1.
"b" denotes significantly higher or lower compared to other treatment on day 3.

## 4.4     Discussion of the current method

With the current method, the surface modification of pDA assisted nHA coating on 3D printed PLGA scaffolds was studied. From the observations of surface morphology, elemental composition, hydrophilicity, as hypothesized, pDA significantly promoted the immobilization of nHA on the PLGA surface.

The roughened surfaces of scaffold struts were observed from the global view of PLGA/pDA and PLGA/pDA-nHA scaffolds compared to relatively smooth surfaces of PLGA and PLGA/nHA, which suggested pDA and pDA-nHA readily modified the PLGA surfaces. Nevertheless, there was no visible differences in strut width among the groups, suggesting the 12-hour incubation with PDA or pDA-nHA was not detrimental to the bulk structure, despite the basic

56

(pH=9.5) liquid environment. In contrast, in a previous study, the strut width of PLGA scaffolds was significantly reduced after alkali treatment (pH=12.0) for only 2 hours.[172]

Although polydopamine coating has been shown to be an effective method to modify polymer surfaces, the thickness of the pDA coating was limited with the traditional method (pH=8.5, 10mM Tris-HCl, room temperature).[162] Therefore, enhancing the coating speed could significantly improve the coating thickness. An increase in the non-oxidized monomer dopamine has demonstrated positive effects on the pDA coating thickness.[166,167] Increasing the dopamine concentration to 8 mg/mL has been reported to greatly increase the coating thickness to 80 nm (20 nm/h) and no further improvement was obtained with higher concentrations.[158,159] Metal ions and hydrogen peroxide have also been shown to serve as oxidants in the dopamine solution to catalyze the coating growth to 43 nm/h.[163] Meanwhile, adjusting the oxidant/dopamine ratio and raising the temperature have improved the coating speed to $90 \pm 5$ nm/h.[164] The highest reported pDA coating speed was 339 nm/h, obtained by treating the substrate with sulfuric acid/sodium sulfate gas in a 300°C nitrogen environment.[165] Compared to previous results for pDA deposition, the present study achieved a much higher coating speed (1435 nm/h) than the coating from other traditional Tris-HCl methods, with uniform thickness and distribution. Remarkably, the PLGA/pDA-nHA provided an even higher coating speed of 1842 nm/h, probably resulting from the presence of both dopamine monomer and nHA, which may be cross-linked during the oxidation of dopamine and form larger molecular groups prior to the deposition on the PLGA substrate.

In addition to the promising coating thickness and speed, higher magnification of the pDA-nHA coating from the top and cross-sectional view of the struts revealed interconnected cancellous bone-like porous structures on the surfaces of both PLGA/pDA and PLGA/pDA-nHA. The porous structure achieved was similar to a previous study,[173] in which nHA served as a stabilizer for pDA-

57

imprinting proteins. More importantly, these interconnected porous structures have demonstrated benefits for protein (e.g. BMP-2) adsorption, nutrient transport,[174] and cell activities.[175] Therefore, the surfaces of PLGA/pDA and PLGA/pDA-nHA formed in this study might also have advantages for cell-material interactions.

The pDA and pDA-nHA coating was investigated by EDX as well. Although the amount of nitrogen might be too small to detect, the changes in carbon and oxygen between PLGA and PLGA/PDA verified the existence of pDA. Due to the high ratio of molecular weight of carbon to oxygen (96 g/mol to 32 g/mol) in pDA, it was not surprising that the carbon in pDA constituted a larger elemental percentage than oxygen in the new material (PLGA/PDA). Considering the coating layer in PLGA/pDA observed in **Figure 4.4C**, the pDA coating was indeed successful. Regarding the nHA coating, the amount of calcium in PLGA/pDA-nHA was nearly double that in PLGA/nHA, demonstrating that PDA promoted nHA adhesion on the PLGA surface. Moreover, the ratio of calcium/phosphorus in PLGA/nHA (1.4) and PLGA/pDA-nHA (1.657) are approximately the ratio of calcium and phosphorous in a nHA molecule (1.667). Thus, the coating of nHA was successful and the presence of pDA positively influenced the deposition of nHA.

The FTIR spectra provided additional support of the effective surface modifications. The peak at 1150 cm$^{-1}$ (P=O bond) was the highest in PLGA/pDA-nHA. Interestingly, the peak at the same location in PLGA/nHA was higher compared to PLGA/pDA and PLGA, which indicated that even the negligible amount nHA on PLGA/nHA surface was detectable by FTIR. Additionally, the wide band of O-H became shorter in PLGA/pDA-nHA with the presence of the P=O peak, in comparison to that in PLGA/pDA. This might imply that the hydroxyl groups from dopamine donated one hydrogen and replaced it with a calcium ion from nHA, supporting the

58

hypothesis that the dopamine was crosslinked with nHA during the oxidation process. Therefore, the P=O peak in PLGA/pDA-nHA likely represented a substantial amount of nHA on the surface.

Besides the surface chemistry, hydrophilicity is another essential surface condition that affects the performance of biodegradable polymer scaffolds.[155] Differences between all pairwise comparisons indicated both pDA and nHA alone significantly improved the surface hydrophilicity, and the combination of pDA and nHA provided extra wettability and produced the most hydrophilic surface (26.02 ± 2.58º). This was lower than 55.1º[176] and 32.7 ± 3.9º[110] reported from recent studies of pDA and ceramic coatings. The pDA-nHA modified PLGA surface also showed superior hydrophilicity to the previous study of 2-hour alkali-treated, nHA coated surface with a contact angle of 51.87° ± 13.29°.[172]

## 4.5    Summary of the current method

In summary, although pDA coating is a convenient way to improve surface conditions of biodegradable polymers, prior methods of pDA coating have had limited coating speed (and thus coating thickness).  Herein, using a modified pDA coating method of increasing the pH to 9.5 and the temperature to 60ºC, pDA, and pDA-nHA coating speed and thickness were greatly enhanced. The surface morphology, elemental composition, and hydrophilicity collectively demonstrated the effective surface modification achieved by pDA and pDA-nHA on 3D printed PLGA scaffolds. Additionally, the interconnected porous structure formed in the coating layer may enable drug loading functionality and improved cell-substrate interactions. Despite the promising results, some of the scaffolds appeared to be deformed (swirled) after pDA modification, which may due to that treatment temperature (60°C) reach the glass transition temperature. Alternatively, both this and the low cell viability issues may be solved by the modified treatment: (i) perform the pDA-treatment at 45°C; and (ii) ultrasonicate the pDA-treated PLGA to remove unattached pDA or

other intermediate chemicals to attenuate the dose of pDA immobilized on PLGA surface. Evaluation of scaffolds coated by this modified method is described below, (iii) for a more appropriate comparison, the control groups will be as printed PLGA treated with Tris-HCl only and the as printed PLGA treated with ultrasonication.

## 4.6 Results for the alternative method

### 4.6.1 Characterization of global structure and surface morphologies

To observe the microstructural surface modifications incurred during the nHA, pDA, and hybrid pDA-nHA coating process, the scaffolds were observed from the top by SEM under 30×, 1000×, and 5000×, corresponding to the global view, inset, and surface view, respectively, in **Figure 4.8**. From the global view, the porous structure was uniformly fabricated on the as-printed PLGA scaffold treated with Tris buffer and ultrasonication (**Figure 4.8A**). No differences in strut width or cross-sectional area were observed among the groups ($p$ = 0.815) (**Figure 4.9**). However, variations in surface morphologies were identified from the inset and surface views. Micro-pores were visible on the surface of PLGA (**Figure 4.8B**), PLGA/nHA (**Figure 4.8D**), and pDA (**Figure 4.8F**). nHA displayed visible nHA particles on the porous surface (**Figure 4.8D**). No surface pores were observed on pDA-nHA (**Figure 4.8H**). To further evaluate the coatings on the PLGA substrate, cross-sectional views were obtained by SEM scanning under 300× and 5000× (inset) (**Figure 4.10**). No differences in the strut cross-section or coating thickness were visible among the groups. Interestingly, the surface pores that were not visible from

60

the top views of pDA-nHA (**Figure 4.8H**) were observed in the cross-sectional view

(**Figure 4.10G&H**).
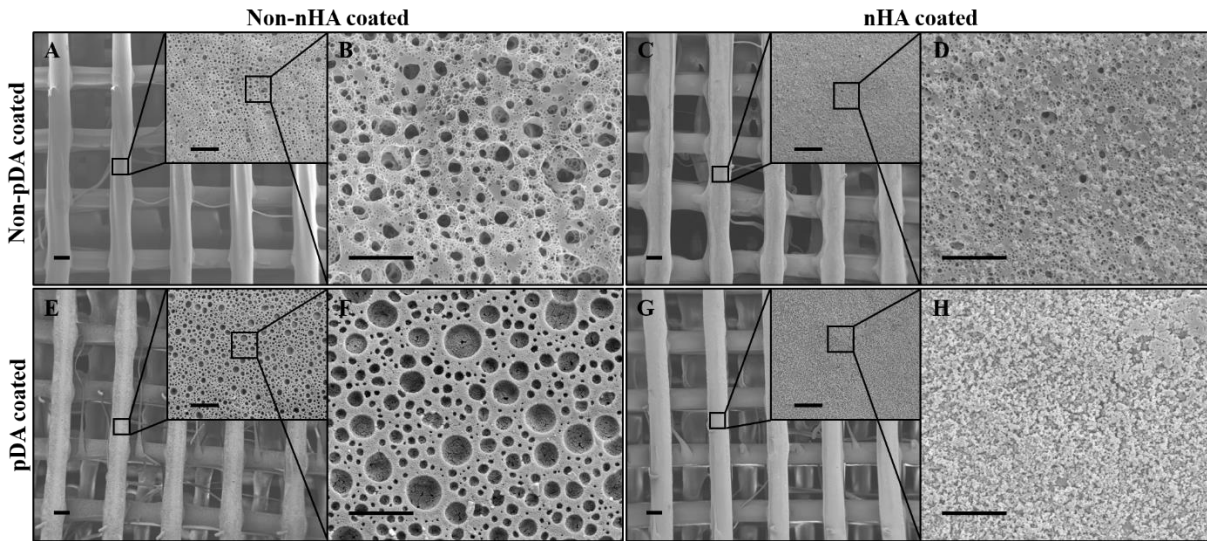


Figure 4.8     (A) PLGA scaffold, (B) Surface view of PLGA scaffold, (C) PLGA/nHA scaffold, (D) Surface view of PLGA/nHA scaffold, (E) PLGA/PDA scaffold, (F) Surface view of PLGA/pDA scaffold, (G) PLGA/pDA-nHA scaffold, (H) Surface view of PLGA/pDA-nHA scaffold.

Scaffold global view images (30X), scale bars = 200µm. Inset images (2000X), scale bars = 10µm. Surface view images (5000X), scale bars = 5µm.
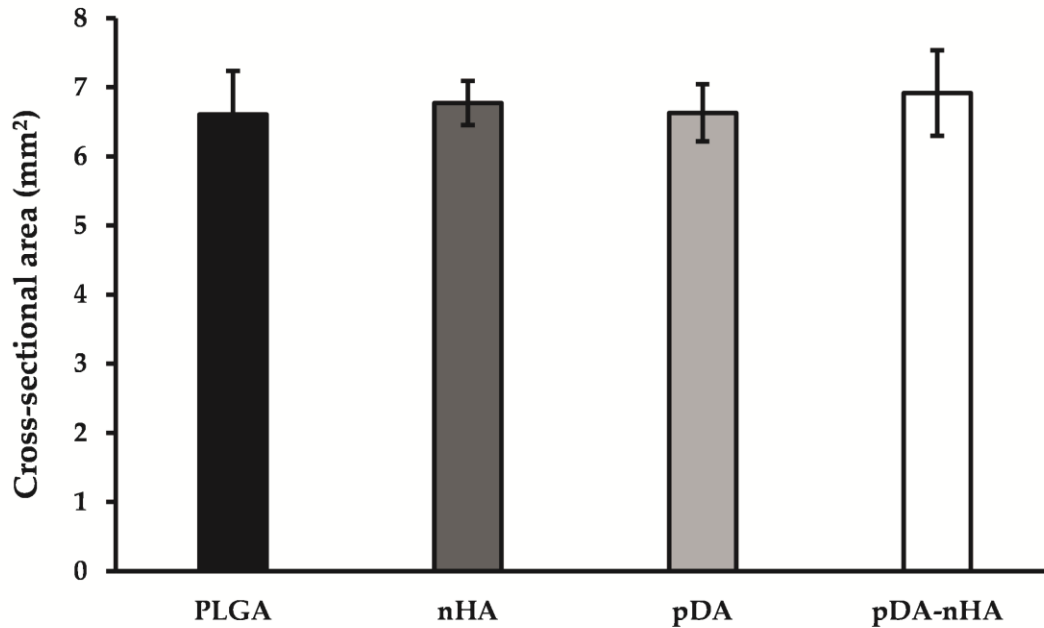
Figure 4.9    Comparison of cross-sectional area for all the groups. *(p>0.05)*
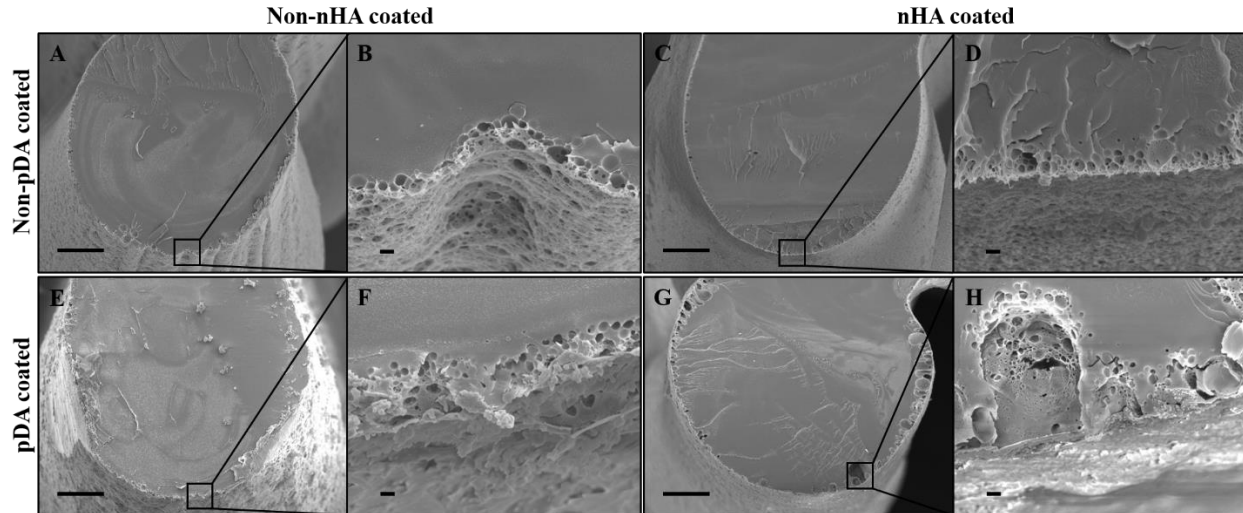


Figure 4.10    Cross-sectional view of a single strut from (A) PLGA scaffold, (C) PLGA/nHA scaffold, (E) PLGA/pDA scaffold, (G) PLGA/pDA-nHA scaffold. Horizontal view of cross-section from (B) PLGA scaffold, (D) PLGA/nHA scaffold, (F) PLGA/pDA scaffold, (H) PLGA/pDA-nHA scaffold.

Scale bars of single strut images (300X) = 500µm. Scale bars of the horizontal view (5000X) = 1µm.

62

To further investigate the formation of surface micropores, the as printed PLGA scaffold treated only with Tris-HCl and only with ultrasonication were scanned under SEM. It was clearly shown that the Tris-HCl added micropores to the surface (**Figure 4.11B**), while ultrasonicated scaffold left a smooth surface (**Figure 4.11D**). Clearly, Tris buffer but not ultrasonication introduced porous surface patterns.
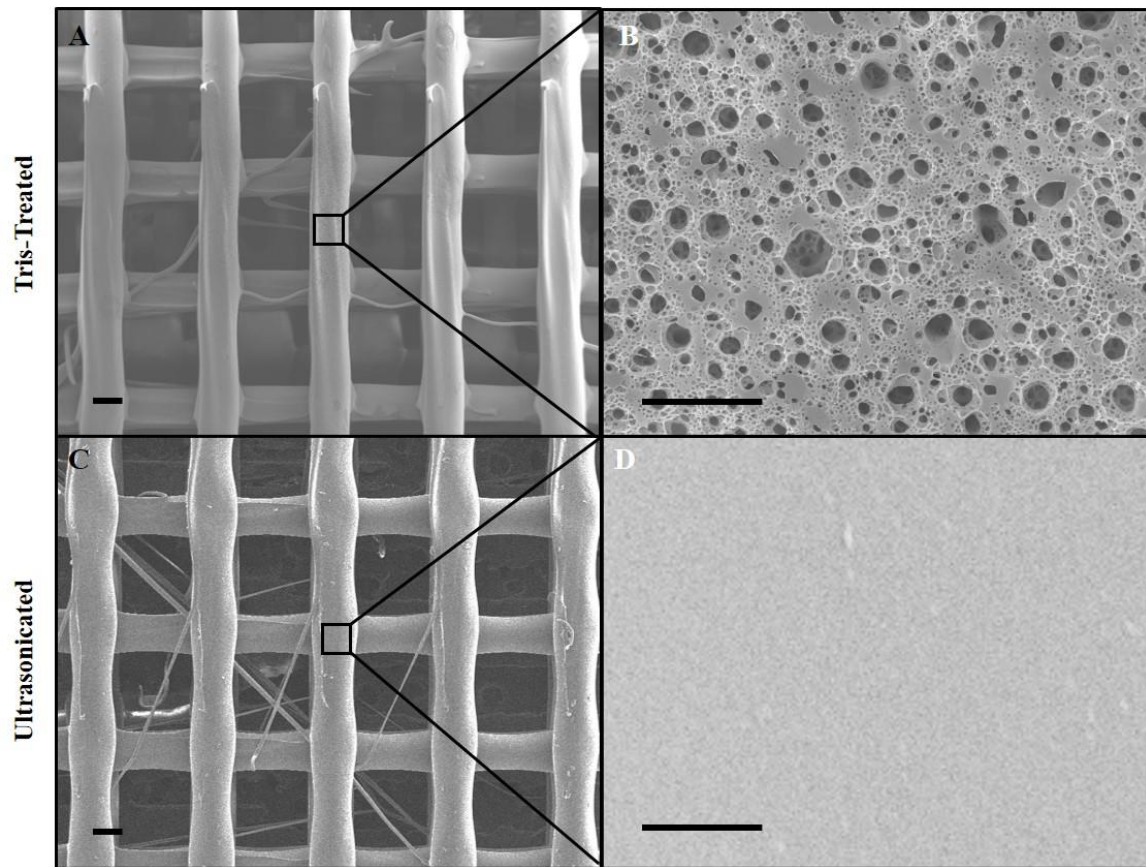


Figure 4.11    The effect of Tris-HCl and ultrasonication on 3D printed PLGA surface.

(A) and (B) The global view and the surface view of Tris-treated scaffold.
(C) and (D) The global view and the surface view of ultrasonicated scaffold.

### 4.6.2   Water contact angle analysis

Water contact angle measurements were used to analyze the influence of pDA and nHA on the hydrophilicity of the materials. As shown in **Figure 4.12**, the WCA was $68.1 \pm 4.4°$ for PLGA, $57.5 \pm 6.7°$ for PLGA/nHA, $52.6 \pm 2.2°$ for PLGA/PDA, and $44.5 \pm 4.1°$ for PLGA/PDA-nHA, in which PLGA was significantly higher than all other groups, no difference was observed between PLGA/nHA and PLGA/pDA, and PLGA/pDA-nHA was the lowest (all pairwise comparisons, $p<0.0001$). Since angles less than $90°$ can be defined as hydrophilic surfaces, all the groups exhibited hydrophilic surfaces, but PLGA/pDA-nHA was the most hydrophilic. Notably, the water contact angle of control ($68.1 \pm 4.4°$) in this alternative method (PLGA treated with Tris-HCl buffer) was significantly lower than the control ($108.6 \pm 5.9°$) in the original method (PLGA without Tris-HCl treatment). This reduction was potentially due to the presence of hydrophilic functional groups (-OH and -$NH_2$) in Tris-HCl molecules which altered surface geometries by adding micro-patterns (**Figure 4.11B**) even after ultrasonication.

64
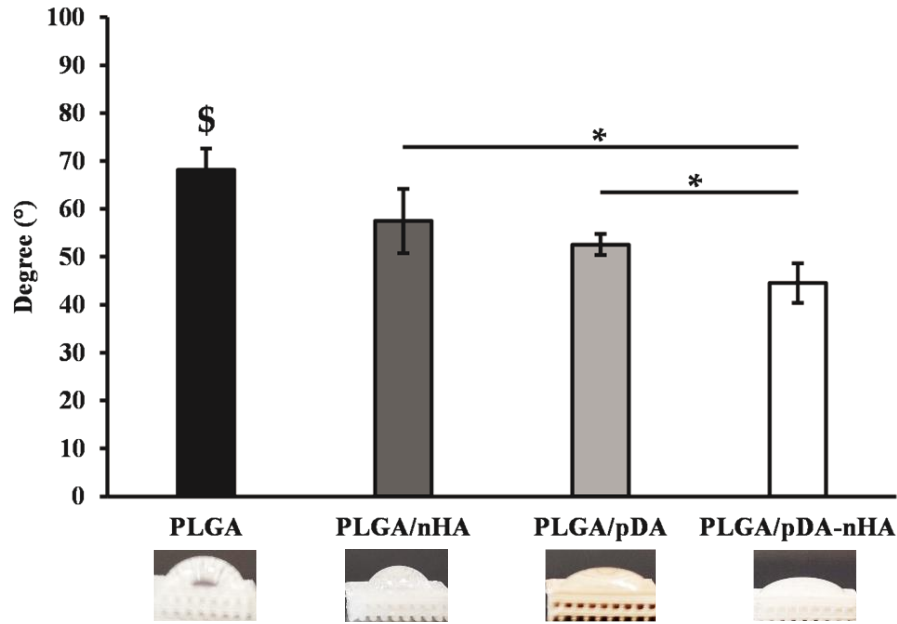
Figure 4.12    Water contact angle. $p<0.0001$ compared to all groups. *$p<0.0001$ pairwise comparisons as indicated. (n=5)

### 4.6.3    Mechanical properties

Polydopamine and nHA coating played an important role in modifying the surface conditions of 3D printed PLGA scaffold. It is worth investigating the potential effects of the coating on mechanical properties. First, the cross-sectional area was obtained for calculating the Young's modulus, and no difference was observed ($p > 0.5$) (**Figure 4.13A**). Similarly, the stiffness ($p > 0.5$) (**Figure 4.13B**) and Young's modulus ($p > 0.5$) (**Figure 4.13C**) was not varied for all the groups. Therefore, the pDA and nHA coatings did not affect the mechanical properties of 3D printed PLGA scaffold and all groups of scaffolds retained sufficient Young's modulus that is comparable to native cancellous bone (up to 500 MPa).

65
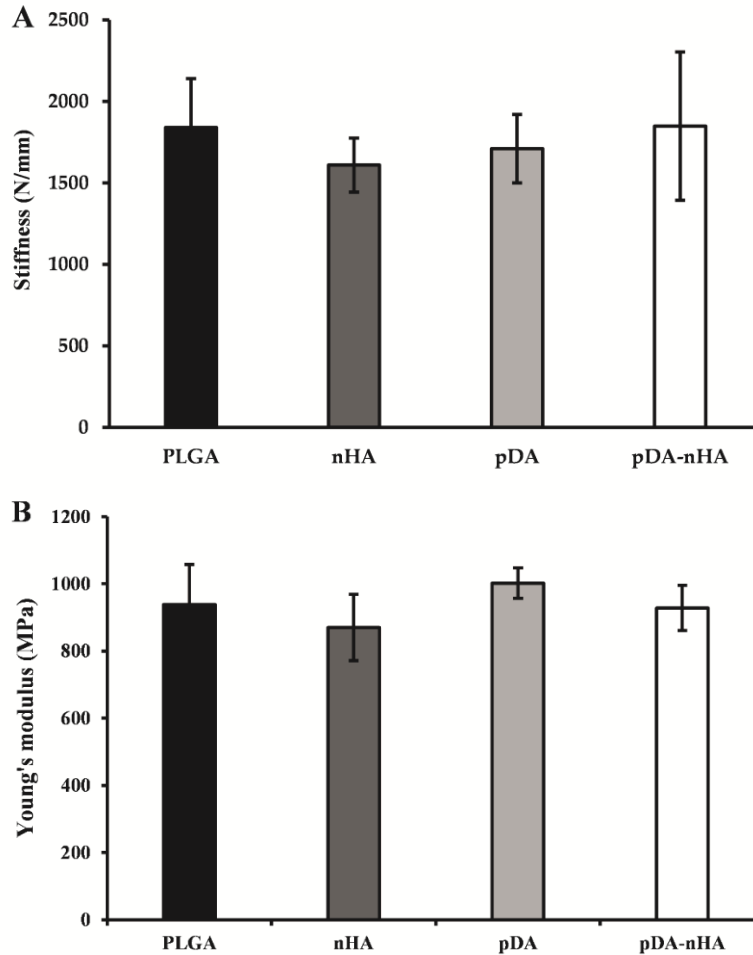
Figure 4.13    (A) Stiffness and (B) Young's modulus (n=8). No significant different in all the groups.

### 4.6.4    Cell viability analysis

After modifying the treatment process (use lower treatment temperature and ultrasonicate the unattached pDA and other intermediate chemicals), the dose of pDA was expected to be significantly reduced. The cell viability showed that no cell dead in day 1, 3, and 5 pDA extract. On the contrary, the cell number seemed to be higher in day 5 extract (**Figure 4.14**), suggesting that the concentration of pDA dose was low enough to be cell-friendly and high enough to promote

66

cell proliferation which agreed to other studies. However, further analysis of cell activities needs to be carried on verifying the efficacy of modified pDA treatment.
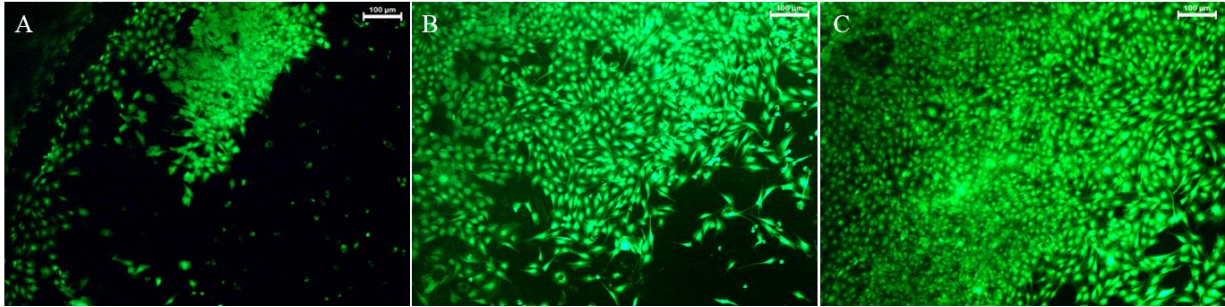


Figure 4.14    Cell viability assay on day 1 (A), day 3 (B), day 5 (C).

(Viable cells are stained green, dead cells red). The cells in all treatments are alive and the cell numbers seems to increase from day 1 to day 5

### 4.6.5    Cell adhesion, proliferation, and differentiation analysis

The in vitro cell culture was conducted to verify the influences of pDA-nHA coating on cell attachment and proliferation measured by CCK-8 kit. MC3T3 cells were seeded on scaffolds with different coatings to evaluate the adhesion and proliferation of cells on day 1, day 3, and day 5. CCK-8 kit was employed to quantify cell number over the course of 5 days. As shown in **Figure 4.15A**, the cell number on PLGA/pDA was the lowest at the all-time point. Only PLGA/pDA-nHA showed significantly higher cell number from day 1 to day 3 and day 3 to day 5. From the normalized cell number (**Figure 4.15B**), PLGA/pDA-nHA was the only group that reached the tripled cell number for day 5/day 1 compared to less than doubled for the rest of groups. Overall, the pDA-induced nHA coating optimally promoted cell growth among the experimental groups on day 5 ($p<0.05$).

67
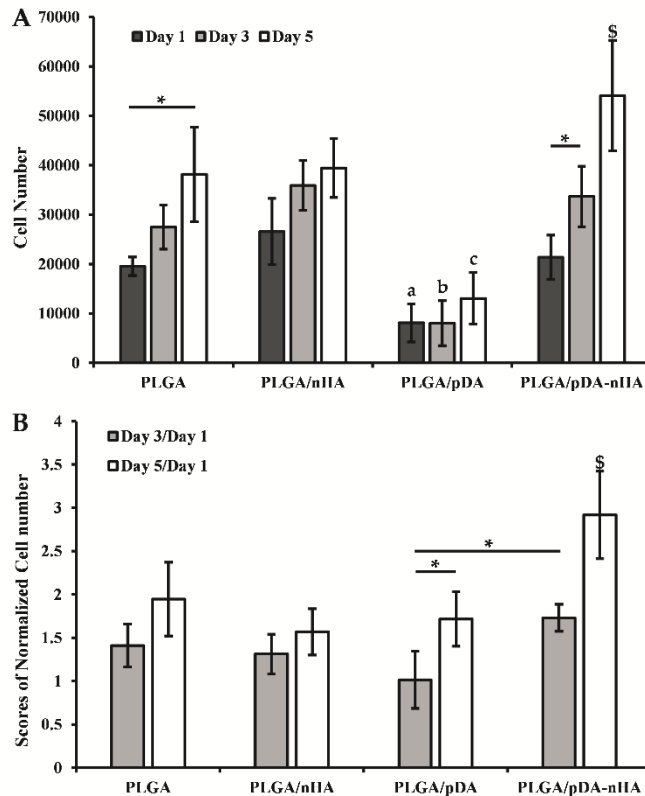
Figure 4.15    (A) Cell number obtained by CCK-8 assay. *Differences over time in the same group. "a", "b", and "c" denote significantly lower than all other groups on day 1, day 3, and day 5, respectively. $ denotes the highest among all the groups. (n=6, $p<0.05$). (B) Cell number normalized to day 1. *Differences in the same or between different groups.

## 4.7    Discussion of the modified method

In this study, we developed a hybrid coating method for pDA-induced nHA surface modifications on 3D printed PLGA scaffolds and analyzed the effects of the coatings on material properties. The PLGA scaffolds were 3D printed successfully and consistently. Similar to previous research of nHA coating on 3D printed PLA scaffold via alkali treatment[177], a few thin residuals were detected between the struts (**Figure 4.8A**),

68

likely due to the motion of printhead, which is typical for fused deposition modeling printing. Notably, the residuals remained on all the treated groups (**Figure 4.8C, E, and G**) in this study, which was not the case in the previous study. This indicated that the 12-hour long process of pDA-nHA coating was not detrimental (i.e, causing polyester hydrolysis) to the substrate material, though the treatment environment was also basic (pH=9.5) in this study. Additionally, the cross-sectional areas for all the groups were equivalent, further confirming the surface modification method in this study is polymer friendly. The micro-/nano-porous structures formed on the surface of the struts on PLGA and pDA groups were first reported in this study. Previously, unmodified (as-printed) PLGA displayed a smooth surface[178]. Here, the Tris buffer itself created micro-/nano-pores on the PLGA surface (**Figure 4.8B**). The surface porous structure on pDA appeared more regular (pore shape and depth), suggesting pDA might regulate the formation of the surface coating in a more organized way. Compared to either pDA or nHA alone, the less visible surface pores on pDA-nHA surface (top views, **Figure 4.8H**) might be due to entanglement/crosslinking of pDA with nHA particles, forming a denser coating with fewer void spaces. The lower Ra value of pDA-nHA compared to pDA alone also supported the SEM observation that the coating was not only visibly denser but also less rough due to the lack of microscale pores. Although the mechanism of porous coating formation is not clear from this study, the micro-/nano-texture on PLGA could be beneficial for cell-material interactions.[95,161]

The FTIR spectra verified the efficacy of the surface modifications by detection of related functional groups in the coating. The highest P=O peak at 1150 cm$^{-1}$ found in pDA-nHA suggested substantial nHA immobilization. This P=O peak in nHA was higher than those in pDA and PLGA,

indicating that even the limited amount of nHA was detectable by FTIR. Notably, since both C-N and N-H peaks were absent in PLGA and nHA, the Tris buffer molecules (containing -C-NH$_2$) did not remain in the coating. Additionally, ultrasonication did not alter surface morphology (**Figure 4.11C-D**). Therefore, Tris buffer might only trigger the formation of the porous coating, rather than becoming a component of the porous coating. In contrast, the C-N and N-H peaks in pDA and pDA-nHA could be attributable to both pDA and Tris buffer, since pDA can react to Tris buffer via Michael addition reaction under a basic environment. This could explain why the C-N and N-H peaks became shorter in pDA-nHA, as the additional nHA particles competitively interacted with pDA and fewer nitrogen sources from the Tris buffer were immobilized in the coating.

Hydrophilicity is an important parameter affecting cell function on the surface of a biomaterial. The analysis of the water contact angle provided further supportive information of the coating efficacy. It is well known that polyesters are hydrophobic materials. However, PLGA in this study exhibited hydrophilic properties based on the WCA ($68.1 \pm 4.4°$) below 90°, compared to the as-printed PLGA ($108.62 \pm 5.86°$),[178] presumably due to the rougher surface after soaking in Tris buffer. Although both nHA and pDA alone improved the hydrophilicity, the WCA further decreased with the hybrid pDA-nHA coating. Typically, greater surface roughness leads to a lower WCA (i.e, hydrophilic substrate) [179]. Here, pDA-nHA with the lowest surface roughness displayed the highest hydrophilicity. Clearly, the physical microstructures on the surface were not the only factor affecting WCA, but rather the hydrophilic functional groups (catechol, amine, and hydroxyl) of both pDA and nHA molecules interacted with the water droplet to enhance the hydrophilicity of the substrate. It is hypothesized that the nHA particles were not simply entrapped within or deposited onto the pDA layer, as is the case for other pDA coating methods; instead, the nHA and

70

pDA particles may have anchored together, growing in an entangled manner through the thickness of the coating. To verify this assumption, the mechanism of dopamine polymerization in the presence of nHA should be explored further.

At the beginning of the polymerization process, the monomer dopamine (DA) is oxidized into dopamine quinone, which then forms leucodopaminechrome (DAL) through a cycloaddition reaction [180]. Further oxidation of DAL produces 5,6-dihydroxyindole (DHI). Consequently, 5,6-indolequinone is formed, which branchingly reacts with DHI, resulting in a majority of dimers and higher-order oligomers being self-polymerized into a coating layer on the substrate [98] through covalent bonds, hydrogen bonds, $\pi$ bonds, and catechol/quinone interactions [99100101]. Among these interactions, $\pi$ bonds and salt displacement between the amine groups and aromatics rings are thought to be the main contributors to the strong attractions between the poly-catecholamine molecules [102]. Under this circumstance, dopamine polymerization took place primarily between DA monomers and intermediate oligomers/polymers (e.g. DHI, pDA) until the polymer chain was saturated, instead of relying on polymer-polymer interactions [181]. This provided a critical but short window for nHA to anchor to the catechol and amine free radicals since the presence of non-oxidized dopamine was essential for the formation and growth of the pDA coating [162]. Consequently, these nHA-anchored monomers and oligomers likely polymerized together to eventually form a hybrid coating on the substrate, rather than starting nHA deposition after the completion of dopamine polymerization to form an nHA coating on top of the pDA layer, which was conducted by the current standard of the pDA-based coating studies.

It is essential that a surface coating method maintain the mechanical properties of biomaterials for load-bearing applications in bone tissue engineering. Since polydopamine and nHA coatings modified the surface conditions of 3D printed PLGA scaffolds, the effects of the

71

coatings on mechanical properties were also investigated. Stiffness and effective Young's modulus were similar among groups. While the coating strongly modified the surface conditions, the thickness of the coating (around 2 µm) was negligible in comparison to the diameter of a single strut (around 300 µm). Thus, it is reasonable that the coating was not sufficient to increase the scaffold's bulk mechanical properties. This finding was consistent with previous research [182][176], in which PLGA and pDA coated PLGA scaffolds displayed similar strut width and effective Young's modulus.

The pDA-nHA hybrid coating network was advantageous to cell-material interactions in this study. In the conventional pDA-nHA coating (nHA onto pDA in a layer-wise manner), cells are likely exposed to only the nHA layer. The polydopamine layer in the middle simply serves as a mediator for immobilizing nHA, sacrificing any positive effects on pDA on cellular functions. From SEM, pDA alone displayed micro-/nano-porous features (**Figure 4.8E&F**), which have been shown by others to facilitate the cell attachment process [121] and activate intracellular signal transductions [122], such as ROCK (RhoA kinase)-myosin II pathway [183]. Polydopamine coating has also been reported to promote the adhesion and proliferation of cells on various surfaces (e.g. MC3T3s on polyethylene, human mesenchymal stem cells on PCL), due to an increase in the immobilization of serum adhesive proteins [115][116][117][97][118]. This might be directly related to the improvement of surface hydrophilicity [119] and presence of functional groups (e.g., $OH^-$, $NH_2^-$)[120]. In a study of pDA coating (2 mg/mL) on PLA scaffolds [112], higher human adipose-derived stem cell (hADSC) attachment rate and proliferation were observed on pDA-modified PLA compared with PLA alone over the course of 7 days. Type I collagen (Col I) secretion was significantly higher on the substrates with the 2 mg/mL pDA coating 1-hour post-seeding than on the non-pDA treated substrate[112]. In this study, surprisingly, pDA showed the lowest cell adhesion on day 1,

72

which has not been reported from similar studies. The concentration of pDA—4 mg/mL during the coating procedure—whether only immobilized on or also eluting from the pDA scaffold, might have been high enough to impede cell attachment (day 1). A lower dosage of dopamine (e.g., 3 mg/mL) may be used in the future to promote improved cell adhesion and proliferation for pDA alone group. On the contrary, the pDA-nHA coating did not inhibit cell attachment, and significantly promoted cell growth, likely due to the exposure of cells to both nHA and (a more moderate amount of) pDA. It is believed the entangled nHA in the coating functioned in two ways: reducing the dosage of pDA and providing additional nano-sized surface patterns, which each benefited cell attachment and proliferation [40]. Here, presumably due to exposure of cells to both nHA and pDA particles, superior proliferation on the hybrid pDA-nHA coating compared to either coating alone was observed.

### 4.8    Summary of the modified method

In this study, nHA particles were successfully immobilized within a hybrid pDA-nHA coating on the surface of 3D printed PLGA scaffolds via dopamine self-polymerization. The pDA-nHA coating introduced micro-/nano-surface texture, increased hydrophilicity, and improved cell proliferation, but did not affect the bulk structure or mechanical properties. Instead of a layer-wise coating of pDA then nHA, nHA was introduced to the PLGA surface during dopamine polymerization. Being anchored with pDA particles and polymerization intermediates, the long-term stability of nHA particles on the PLGA substrate is worth investigating. Overall, the dopamine-based coating method holds great potential for the functionalization of surfaces with not only ceramic particles such as nHA but also metal ions (e.g. $Zn^{2+}$, $Mg^{2+}$, and $Ag^+$) and growth factors (e.g. BMP-2 and VEGF), to further direct cell-material interactions for a wide range of biomaterial substrates in a simple and effective manner.

73

# FUTURE STUDY: EVALUATE THE EFFECTS OF POLYDOPAMINE INDUCED NHA COATING ON PLGA-NHA COMPOSITE SCAFFOLD

It has been demonstrated that pDA and nHA particles on a substrate can modify the surface morphology and improve osteoconductivity and osteoinductivity with, e.g., MC3T3s and human adipose-derived stem cells (hADSCs)[126,112]. However, given the nature of coating (i.e., limited thickness compared to the printed struts), the mechanical properties may not be significantly affected. nHA as a ceramic additive can improve the mechanical properties of PLGA scaffolds, while it may not sufficiently modify the surface conditions. Therefore, the PLGA-nHA composite coated with pDA-nHA (PLGA-nHA/pDA-nHA) may produce both superior mechanical properties and surface conditions. The *objectives* of this aim are: (i) to characterize the surface conditions (morphologies, chemistries, and roughness) of PLGA-nHA/pDA-nHA scaffold, (ii) to investigate the mechanical properties of the pDA-nHA modified PLGA/nHA composite scaffold, and (iii) to evaluate the biological properties of PLGA-nHA/pDA-nHA scaffold. It is *hypothesized* that: (i) PLGA-nHA/pDA-nHA will present superior surface conditions (i.e., coating thickness and surface roughness compared to PLGA/pDA-nHA), (ii) the pDA-nHA coating will not be sufficient to increase the mechanical properties of PLGA/nHA composite scaffold, while those of the composite PLGA-nHA/pDA-nHA will be higher than PLGA/pDA-nHA, and (iii) cell attachment, proliferation, and differentiation will be improved on PLGA-nHA/pDA-nHA compared to PLGA/pDA-nHA.

74

## 5.1 Rationale

Although pDA-nHA coating has been verified as a simple and effective approach to modify the surface of 3D printed PLGA scaffold in the previous study, the mechanical properties were not significantly improved with the pDA-nHA coating. On the other hand, PLGA-nHA composite scaffold showed superior mechanical properties over PLGA scaffold but with less capabilities of altering surface conditions compared to pDA-nHA. It is worth combining both advantages in one application. Toward this end, this aim will focus on: (i) the investigation of surface morphologies and chemistries of PLGA-nHA composite scaffold coated with pDA-nHA (PLGA-nHA/pDA-nHA), (ii) the comparisons of stiffness and effective Young's modulus of PLGA/pDA-nHA and PLGA-nHA/pDA-nHA scaffold, (iii) the study of *in vitro* cell behaviors on PLGA/pDA-nHA and PLGA-nHA/pDA-nHA scaffold. The *hypotheses* are that: (i) PLGA-nHA/pDA-nHA will produce thicker and rougher pDA-nHA coating than PLGA/pDA-nHA, (ii) PLGA-nHA/pDA-nHA is expected to have superior stiffness and effective Young's modulus than PLGA/pDA-nHA, (iii) the cell attachment (CCK-8 on day 1 and Phalloidin/DAPI staining), proliferation (CCK-8 on day 3 and day 5), and differentiation (ALP on day 14) will be improved more on PLGA-nHA/pDA-nHA than PLGA/pDA-nHA.

## 5.2    Experimental approach and data analysis
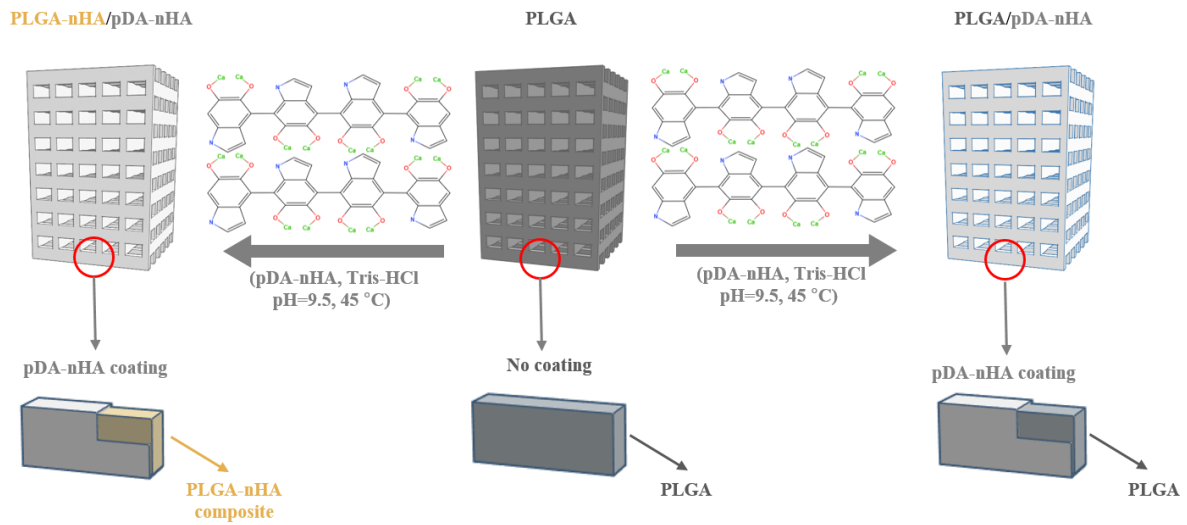


Figure 5.1      The mechanism of pDA-nHA coating on PLGA-nHA composite scaffold.

REFERENCES

1.  Zhou, H., Lawrence, J. G. & Bhaduri, S. B. Fabrication aspects of PLA-CaP/PLGA-CaP composites for orthopedic applications: A review. *Acta Biomater.* **8**, 1999–2016 (2012).

2.  WOOLF, A. D.; PFLEGER, B. Burden of major musculoskeletal conditions. Bulletin of the World Health Organisation. **9**, 2003 (2003).

3.  Ahmadi, S. M. *et al.* Additively manufactured open-cell porous biomaterials made from six different space-filling unit cells: The mechanical and morphological properties. *Materials (Basel).* **8**, 1871–1896 (2015).

4.  D. de Moulin. *A history of surgery: with emphasis on the Netherlands - D. de Moulin - Google Books*. (Springer Science & Business Media, 2012).

5.  Baroli, B. From natural bone grafts to tissue engineering therapeutics: Brainstorming on pharmaceutical formulative requirements and challenges. *Journal of Pharmaceutical Sciences* vol. 98 1317–1375 (2009).

6.  Logeart-Avramoglou, D., Anagnostou, F., Bizios, R. & Petite, H. Engineering bone: challenges and obstacles. *J. Cell. Mol. Med.* **9**, 72–84 (2005).

7.  Younger, E. M. & Chapman, M. W. Morbidity at bone graft donor sites. *J Orthop Trauma* **3**, 192–195 (1989).

8.  Amini, A. R., Laurencin, C. T. & Nukavarapu, S. P. Bone tissue engineering: recent advances and challenges. *Crit. Rev. Biomed. Eng.* **40**, 363–408 (2012).

9.  *Bone fixation device*. (2001).

10. *Bimetal acetabular component construct for hip joint prosthesis*. (2001).

11. Intervertebral cage and method of use. (1999).

12. Surmeneva, M. A. *et al.* Fabrication of multiple-layered gradient cellular metal scaffold via electron beam melting for segmental bone reconstruction. *Mater. Des.* **133**, 195–204 (2017).

13. Long, M. & HJ, R. Titanium alloys in total joint replacement - A materials science perspective. *Biomater* **19**, 1621–1639 (1998).

77

14. Liu, X., Chu, P. K. & Ding, C. Surface modification of titanium, titanium alloys, and related materials for biomedical applications. *Materials Science and Engineering R: Reports* vol. 47 49–121 (2004).

15. McAfee, P. C. *et al.* The effect of spinal implant rigidity on vertebral bone density. A canine model. *Spine (Phila. Pa. 1976).* **16**, S190-7 (1991).

16. Niinomi, M. Recent research and development in titanium alloys for biomedical applications and healthcare goods. *Science and Technology of Advanced Materials* vol. 4 445–454 (2003).

17. Zhang, X.-Y., Fang, G. & Zhou, J. Additively Manufactured Scaffolds for Bone Tissue Engineering and the Prediction of their Mechanical Behavior: A Review. *Materials (Basel).* **10**, 50 (2017).

18. Suganuma, J. & Alexander, H. Biological response of intramedullary bone to poly-L-lactic acid. *J. Appl. Biomater.* **4**, 13–27 (1993).

19. Ribeiro, M., Monteiro, F. J. & Ferraz, M. P. Infection of orthopedic implants with emphasis on bacterial adhesion process and techniques used in studying bacterial-material interactions. *Biomatter* **2**, 176–194 (2012).

20. Stradiotti, P., Curti, A., Castellazzi, G. & Zerbi, A. Metal-related artifacts in instrumented spine. Techniques for reducing artifacts in CT and MRI: State of the art. *Eur. Spine J.* **18**, 102 (2009).

21. Geurts, J. A. P. & Walenkamp, G. H. I. M. PMMA beads and spacers for local antibiotic administration. in *Management of Periprosthetic Joint Infections (PJIs)* 219–230 (Elsevier, 2017). doi:10.1016/B978-0-08-100205-6.00010-0.

22. Vaishya, R., Chauhan, M. & Vaish, A. Bone cement. *Journal of Clinical Orthopaedics and Trauma* vol. 4 157–163 (2013).

23. Kühn, K.-D. (Klaus-D. *Bone cements : up-to-date comparison of physical and chemical properties of commercial materials*. (Springer, 2000).

24. Benzel, E. C., Thammavaram, K. & Kesterson, L. The diagnosis of infections associated with acrylic cranioplasties. *Neuroradiology* **32**, 151–153 (1990).

25. Albrektsson, T. & Johansson, C. Osteoinduction, osteoconduction and osseointegration. *Eur. Spine J.* **10**, S96–S101 (2001).

26. Saleh, K. J. *et al.* Acrylic bone cement in total joint arthroplasty: A review. *Journal of Orthopaedic Research* vol. 34 737–744 (2016).

27. Nandi, S. K., Roy, S., Mukherjee, P. & Kundu, B. (PDF) Orthopaedic applications of bone graft & graft substitutes: A review. *Indian J. Med. Res.* **132**, 15–30 (2010).

28. Gentile, P., Chiono, V., Carmagnola, I. & Hatton, P. An Overview of Poly(lactic-co-glycolic) Acid (PLGA)-Based Biomaterials for Bone Tissue Engineering. *Int. J. Mol. Sci.* **15**, 3640–3659 (2014).

29. Dorozhkin, S. V. Calcium orthophosphate-based biocomposites and hybrid biomaterials. in *Journal of Materials Science* vol. 44 2343–2387 (2009).

30. Garlotta, D. A Literature Review of Poly(Lactic Acid). *J. Polym. Environ.* **9**, 63–84 (2001).

31. Makadia, H. K. & Siegel, S. J. Poly Lactic-co-Glycolic Acid (PLGA) as biodegradable controlled drug delivery carrier. *Polymers (Basel).* **3**, 1377–1397 (2011).

32. Thomas, V., Dean, D. R. & Vohra, Y. K. Nanostructured biomaterials for regenerative medicine. *Current Nanoscience* vol. 2 155–177 (2006).

33. Vasita, R., Shanmugam I, K. & Katt, D. S. Improved biomaterials for tissue engineering applications: surface modification of polymers. *Curr. Top. Med. Chem.* **8**, 341–53 (2008).

34. De Bartolo, L., Morelli, S., Bader, A. & Drioli, E. Evaluation of cell behaviour related to physico-chemical properties of polymeric membranes to be used in bioartificial organs. *Biomaterials* **23**, 2485–2497 (2002).

35. Cato T. Laurencin, Mohamed Attawia & Mark D. Borden. Advancements in tissue engineered bone substitutes : Current Opinion in Orthopaedics. *Curr. Opin. Orthop.* **10**, 445–451 (1999).

36. Kofron, M. D. *et al.* The implications of polymer selection in regenerative medicine: A comparison of amorphous and semi-crystalline polymer for tissue regeneration. *Adv. Funct. Mater.* **19**, 1351–1359 (2009).

37. Rizzi, S. C. *et al.* Biodegradable polymer/hydroxyapatite composites: Surface analysis and initial attachment of human osteoblasts. *J. Biomed. Mater. Res.* **55**, 475–486 (2001).

38. Huang, B. *et al.* Polymer-ceramic composite scaffolds: The effect of hydroxyapatite and β-tri-calcium phosphate. *Materials (Basel).* **11**, (2018).

39. Pan, Z. & Ding, J. Poly(lactide-co-glycolide) porous scaffolds for tissue engineering and regenerative medicine. *Interface Focus* **2**, 366–77 (2012).

40. Wang, X., Jiang, M., Zhou, Z., Gou, J. & Hui, D. 3D printing of polymer matrix composites: A review and prospective. *Compos. Part B Eng.* **110**, 442–458 (2017).

41. Shuai, C., Yang, B., Peng, S. & Li, Z. Development of composite porous scaffolds based on poly(lactide-co-glycolide)/nano-hydroxyapatite via selective laser sintering. *Int. J. Adv. Manuf. Technol.* **69**, 51–57 (2013).

42. Xu, S. *et al.* Selective laser sintering fabrication of nano-hydroxyapatite/poly-&amp;epsilon;-caprolactone scaffolds for bone tissue engineering applications. *Int. J. Nanomedicine* 4197 (2013) doi:10.2147/IJN.S50685.

43. Zhao, X. *et al.* BMP-2 immobilized PLGA/hydroxyapatite fibrous scaffold via polydopamine stimulates osteoblast growth. *Mater. Sci. Eng. C* **78**, 658–666 (2017).

44. Habibovic, P. In vitro and in vivo bioactivity assessment of a polylactic acid/hydroxyapatite composite for bone regeneration. *Biomatter* **4**, e27664 (2014).

45. Chen, X. *et al.* 3D printed porous PLA/nHA composite scaffolds with enhanced osteogenesis and osteoconductivity in vivo for bone regeneration. *Biomed. Mater.* **14**, 065003 (2019).

46. Gonçalves, E. M. *et al.* Three-dimensional printed PCL-hydroxyapatite scaffolds filled with CNTs for bone cell growth stimulation. *J. Biomed. Mater. Res. - Part B Appl. Biomater.* **104**, 1210–1219 (2016).

47. Oladapo, B. I., Zahedi, S. A. & Adeoye, A. O. M. 3D printing of bone scaffolds with hybrid biomaterials. *Compos. Part B Eng.* **158**, 428–436 (2019).

48. Neufurth, M. *et al.* 3D printing of hybrid biomaterials for bone tissue engineering: Calcium-polyphosphate microparticles encapsulated by polycaprolactone. *Acta Biomater.* **64**, 377–388 (2017).

49. Kohn, D. H., Sarmadi, M., Helman, J. I. & Krebsbach, P. H. Effects of pH on human bone marrow stromal cells in vitro: Implications for tissue engineering of bone. *J. Biomed. Mater. Res.* **60**, 292–299 (2002).

50. Melchels, F. P. W., Feijen, J. & Grijpma, D. W. A poly(d,l-lactide) resin for the preparation of tissue engineering scaffolds by stereolithography. *Biomaterials* **30**, 3801–3809 (2009).

51. Serra, T., Planell, J. A. & Navarro, M. High-resolution PLA-based composite scaffolds via 3-D printing technology. *Acta Biomater.* **9**, 5521–5530 (2013).

52. Jaidev, L. R. & Chatterjee, K. Surface functionalization of 3D printed polymer scaffolds to augment stem cell response. *Mater. Des.* **161**, 44–54 (2019).

53. Ishack, S., Mediero, A., Wilder, T., Ricci, J. L. & Cronstein, B. N. Bone regeneration in critical bone defects using three-dimensionally printed β-tricalcium phosphate/hydroxyapatite scaffolds is enhanced by coating scaffolds with either dipyridamole or BMP-2. *J. Biomed. Mater. Res. - Part B Appl. Biomater.* **105**, 366–375 (2017).

54. Zakaria, S. M., Sharif Zein, S. H., Othman, M. R. & Jansen, J. A. Hydroxyapatite nanoparticles: Electrospinning and calcination of hydroxyapatite/polyvinyl butyral nanofibers and growth kinetics. *J. Biomed. Mater. Res. Part A* **101A**, 1977–1985 (2013).

55. Trachtenberg, J. E., Placone, J. K., Smith, B. T., Fisher, J. P. & Mikos, A. G. Extrusion-based 3D printing of poly(propylene fumarate) scaffolds with hydroxyapatite gradients. *J. Biomater. Sci. Polym. Ed.* **28**, 532–554 (2017).

56. Wang, M. Developing bioactive composite materials for tissue replacement. *Biomaterials* **24**, 2133–2151 (2003).

57. Khan, Y. M., Katti, D. S. & Laurencin, C. T. Novel polymer-synthesized ceramic composite-based system for bone repair: Anin vitro evaluation. *J. Biomed. Mater. Res.* **69A**, 728–737 (2004).

58. Senatov, F. S., Gorshenkov, M. V., Tcherdyntsev, V. V., Kaloshkin, S. D. & Sudarchikov, V. A. Fractographic analysis of composites based on ultra high molecular weight polyethylene. *Compos. Part B Eng.* **56**, 869–875 (2014).

59. Nie, L. *et al.* Macroporous biphasic calcium phosphate scaffolds reinforced by poly-L-lactic acid/hydroxyapatite nanocomposite coatings for bone regeneration. *Biochem. Eng. J.* **98**, 29–37 (2015).

60. Dávila, J. L. *et al.* Fabrication of PCL/β-TCP scaffolds by 3D mini-screw extrusion printing. *J. Appl. Polym. Sci.* **133**, n/a-n/a (2016).

61. Costa, D. O. *et al.* The differential regulation of osteoblast and osteoclast activity by surface topography of hydroxyapatite coatings. *Biomaterials* **34**, 7215–7226 (2013).

62. He, C., Jin, X. & Ma, P. X. Calcium phosphate deposition rate, structure and osteoconductivity on electrospun poly(l-lactic acid) matrix using electrodeposition or simulated body fluid incubation. *Acta Biomater.* **10**, 419–427 (2014).

63. Hu, Y. *et al.* Regulation of the differentiation of mesenchymal stem cells in vitro and osteogenesis in vivo by microenvironmental modification of titanium alloy surfaces. *Biomaterials* **33**, 3515–3528 (2012).

64. Dinklage, A., Klinger, T., Marx, G. & Schweikhard, L. *Plasma Physics Confinement, Transport and Collective Effects ei Springer*. https://cds.cern.ch/record/1338842/files/9783540252740_TOC.pdf (2005).

65. Liu, P. *et al.* Surface modification of porous PLGA scaffolds with plasma for preventing dimensional shrinkage and promoting scaffold–cell/tissue interactions. *J. Mater. Chem. B* **6**, 7605–7613 (2018).

66.	Tian, H., Tang, Z., Zhuang, X., Chen, X. & Jing, X. Biodegradable synthetic polymers: Preparation, functionalization and biomedical application. *Prog. Polym. Sci.* **37**, 237–280 (2012).

67.	Chan, C.-M., Ko, T.-M. & Hiraoka, H. Polymer surface modification by plasmas and photons. *Surf. Sci. Rep.* **24**, 1–54 (1996).

68.	*Long Term Properties of Polyolefins*. vol. 169 (Springer Berlin Heidelberg, 2004).

69.	Jiao, Y.-P. & Cui, F.-Z. Surface modification of polyester biomaterials for tissue engineering. *Biomed. Mater.* **2**, R24–R37 (2007).

70.	Dee, K. C., Puleo, D. A. & Bizios, R. *An introduction to tissue-biomaterial interactions*. (Wiley-Liss, 2002).

71.	Ito, Y. Covalently immobilized biosignal molecule materials for tissue engineering. *Soft Matter* **4**, 46–56 (2008).

72.	Ma, Z., Mao, Z. & Gao, C. Surface modification and property analysis of biomedical polymers used for tissue engineering. *Colloids Surfaces B Biointerfaces* **60**, 137–157 (2007).

73.	Quirk, R. A., Davies, M. C., Tendler, S. J. B., Chan, W. C. & Shakesheff, K. M. Controlling Biological Interactions with Poly(lactic acid) by Surface Entrapment Modification. *Langmuir* **17**, 2817–2820 (2001).

74.	Cai, K. *et al.* Influence of different surface modification treatments on poly(D,L-lactic acid) with silk fibroin and their effects on the culture of osteoblast in vitro. *Biomaterials* **23**, 1603–11 (2002).

75.	Duan, B. *et al.* Surface modification of three-dimensional Ca-P/PHBV nanocomposite scaffolds by physical entrapment of gelatin and its in vitro biological evaluation. *Front. Mater. Sci.* **5**, 57–68 (2011).

76.	Saxena, S. *et al.* Development of a New Polypropylene-Based Suture: Plasma Grafting, Surface Treatment, Characterization, and Biocompatibility Studies. *Macromol. Biosci.* **11**, 373–382 (2011).

77.	Guang Liu, W. *et al. Effects of baicalin-modi®ed poly(D,L-lactic acid) surface on the behavior of osteoblasts*. https://link.springer.com/content/pdf/10.1023%2FA%3A1026398532009.pdf.

78.	Goddard, J. M. & Hotchkiss, J. H. Polymer surface modification for the attachment of bioactive compounds. *Prog. Polym. Sci.* **32**, 698–725 (2007).

79.	Edlund, U., Sauter, T. & Albertsson, A.-C. Covalent VEGF protein immobilization on resorbable polymeric surfaces. *Polym. Adv. Technol.* **22**, 166–171 (2011).

80.    Park, G. E., Pattison, M. A., Park, K. & Webster, T. J. Accelerated chondrocyte functions on NaOH-treated PLGA scaffolds. *Biomaterials* **26**, 3075–3082 (2005).

81.    Alippilakkotte, S. & Sreejith, L. Benign route for the modification and characterization of poly(lactic acid) (PLA) scaffolds for medicinal application. *J. Appl. Polym. Sci.* **135**, 1–13 (2018).

82.    Yuan, X., Mak, A. F. . & Yao, K. Comparative observation of accelerated degradation of poly(l-lactic acid) fibres in phosphate buffered saline and a dilute alkaline solution. *Polym. Degrad. Stab.* **75**, 45–53 (2002).

83.    He, Y. *et al.* A 3D-Printed PLCL Scaffold Coated with Collagen Type I and Its Biocompatibility. *Biomed Res. Int.* **2018**, 1–10 (2018).

84.    Yang, S., Han, X., Jia, Y., Zhang, H. & Tang, T. Hydroxypropyltrimethyl ammonium chloride chitosan functionalized-PLGA electrospun fibrous membranes as antibacterialwound dressing: In vitro and in vivo evaluation. *Polymers (Basel).* **9**, 1–19 (2017).

85.    Yu, H. S., Jang, J. H., Kim, T. Il, Lee, H. H. & Kim, H. W. Apatite-mineralized polycaprolactone nanofibrous web as a bone tissue regeneration substrate. *J. Biomed. Mater. Res. - Part A* **88**, 747–754 (2009).

86.    Yanagida, H. *et al.* Cell adhesion and tissue response to hydroxyapatite nanocrystal-coated poly(l-lactic acid) fabric. *J. Biosci. Bioeng.* **108**, 235–243 (2009).

87.    Wang, S., Cui, W. & Bei, J. Bulk and surface modifications of polylactide. *Anal. Bioanal. Chem.* **381**, 547–556 (2005).

88.    Mima, Y. *et al.* Enhancement of cell-based therapeutic angiogenesis using a novel type of injectable scaffolds of hydroxyapatite-polymer nanocomposite microspheres. *PLoS One* **7**, (2012).

89.    Liu, Y., Ai, K. & Lu, L. Polydopamine and its derivative materials: Synthesis and promising applications in energy, environmental, and biomedical fields. *Chemical Reviews* vol. 114 5057–5115 (2014).

90.    Lee, H., Dellatore, S. M., Miller, W. M. & Messersmith, P. B. Mussel-inspired surface chemistry for multifunctional coatings. *Science* **318**, 426–30 (2007).

91.    Lee, H., Dellatore, S. M., Miller, W. M. & Messersmith, P. B. Mussel-inspired surface chemistry for multifunctional coatings. *Science* **318**, 426–30 (2007).

92.    Yan, J. *et al.* Polydopamine Spheres as Active Templates for Convenient Synthesis of Various Nanostructures. *Small* **9**, 596–603 (2013).

93. Ko, E., Yang, K., Shin, J. & Cho, S.-W. Polydopamine-Assisted Osteoinductive Peptide Immobilization of Polymer Scaffolds for Enhanced Bone Regeneration by Human Adipose-Derived Stem Cells. (2013) doi:10.1021/bm4008343.

94. Wang, Z. *et al.* Mussel-inspired nanostructured coatings assembled using polydopamine nanoparticles and hydroxyapatite nanorods for biomedical applications. *Biosurface and Biotribology* **3**, 1–10 (2017).

95. Li, Y. *et al.* Improving Osteointegration and Osteogenesis of Three-Dimensional Porous Ti6Al4V Scaffolds by Polydopamine-Assisted Biomimetic Hydroxyapatite Coating. *ACS Appl. Mater. Interfaces* **7**, 5715–5724 (2015).

96. Wu, C. *et al.* Mussel-inspired bioceramics with self-assembled Ca-P/polydopamine composite nanolayer: Preparation, formation mechanism, improved cellular bioactivity and osteogenic differentiation of bone marrow stromal cells. *Acta Biomater.* **10**, 428–438 (2014).

97. Gao, X. *et al.* Polydopamine-Templated Hydroxyapatite Reinforced Polycaprolactone Composite Nanofibers with Enhanced Cytocompatibility and Osteogenesis for Bone Tissue Engineering. *ACS Appl. Mater. Interfaces* **8**, 3499–3515 (2016).

98. Ball, V. Polydopamine films and particles with catalytic activity. *Catal. Today* **301**, 196–203 (2018).

99. Liebscher, J. *et al.* Structure of polydopamine: A never-ending story? *Langmuir* **29**, 10539–10548 (2013).

100. Hong, S. *et al.* Non-Covalent Self-Assembly and Covalent Polymerization Co-Contribute to Polydopamine Formation. *Adv. Funct. Mater.* **22**, 4711–4717 (2012).

101. Li, M., Liu, X., Xu, Z., Yeung, K. W. K. & Wu, S. Dopamine Modified Organic-Inorganic Hybrid Coating for Antimicrobial and Osteogenesis. *ACS Appl. Mater. Interfaces* **8**, 33972–33981 (2016).

102. Lim, C. *et al.* Nanomechanics of Poly(catecholamine) Coatings in Aqueous Solutions. *Angew. Chemie Int. Ed.* **55**, 3342–3346 (2016).

103. Lee, H., Scherer, N. F. & Messersmith, P. B. *Single-molecule mechanics of mussel adhesion*. vol. 103 www.pnas.orgcgidoi10.1073pnas.0605552103 (2006).

104. Lee, H., Dellatore, S. M., Miller, W. M. & Messersmith, P. B. Mussel-Inspired Surface Chemistry for Multifunctional Coatings. *Science (80-. ).* **318**, 426–430 (2007).

105. Kasemset, S., Lee, A., Miller, D. J., Freeman, B. D. & Sharma, M. M. Effect of polydopamine deposition conditions on fouling resistance, physical properties, and permeation properties of reverse osmosis membranes in oil/water separation. *J. Memb. Sci.* **425**–**426**, 208–216 (2012).

106. Bernsmann, F., Frisch, B., Ringwald, C. & Ball, V. Protein adsorption on dopamine–melanin films: Role of electrostatic interactions inferred from ζ-potential measurements versus chemisorption. *J. Colloid Interface Sci.* **344**, 54–60 (2010).

107. Ryu, J., Ku, S. H., Lee, H. & Park, C. B. Mussel-Inspired Polydopamine Coating as a Universal Route to Hydroxyapatite Crystallization. *Adv. Funct. Mater.* **20**, 2132–2139 (2010).

108. Shin, Y. M., Lee, Y. Bin & Shin, H. Time-dependent mussel-inspired functionalization of poly(l-lactide-co-e{open}-caprolactone) substrates for tunable cell behaviors. *Colloids Surfaces B Biointerfaces* (2011) doi:10.1016/j.colsurfb.2011.05.004.

109. Kord Forooshani, P. *et al.* Antibacterial Properties of Mussel-Inspired Polydopamine Coatings Prepared by a Simple Two-Step Shaking-Assisted Method. *Front. Chem.* **7**, (2019).

110. Liu, Y. *et al.* Polydopamine-modified poly(L-lactic acid) nanofiber scaffolds immobilized with an osteogenic growth peptide for bone tissue regeneration. *RSC Adv.* **9**, 11722–11736 (2019).

111. Iqbal, Z., Lai, E. P. C. & Avis, T. J. Antimicrobial effect of polydopamine coating on Escherichia coli. *J. Mater. Chem.* **22**, 21608–21612 (2012).

112. Kao, C. T. *et al.* Poly(dopamine) coating of 3D printed poly(lactic acid) scaffolds for bone tissue engineering. *Mater. Sci. Eng. C* **56**, 165–173 (2015).

113. Liu, C.-Y. & Huang, C.-J. Functionalization of Polydopamine via the Aza-Michael Reaction for Antimicrobial Interfaces. *Langmuir* **32**, 5019–5028 (2016).

114. Wang, L. *et al.* Mussel-inspired deposition of copper on titanium for bacterial inhibition and enhanced osseointegration in a periprosthetic infection model. *RSC Adv.* **7**, 51593–51604 (2017).

115. Tsai, W.-B., Chen, W.-T., Chien, H.-W., Kuo, W.-H. & Wang, M.-J. Poly(dopamine) coating of scaffolds for articular cartilage tissue engineering. *Acta Biomater.* **7**, 4187–4194 (2011).

116. Ku, S. H., Ryu, J., Hong, S. K., Lee, H. & Park, C. B. General functionalization route for cell adhesion on non-wetting surfaces. *Biomaterials* **31**, 2535–2541 (2010).

117. Chien, H.-W., Kuo, W.-H., Wang, M.-J., Tsai, S.-W. & Tsai, W.-B. Tunable Micropatterned Substrates Based on Poly(dopamine) Deposition via Microcontact Printing. *Langmuir* **28**, 5775–5782 (2012).

118. Alas, G. R., Agarwal, R., Collard, D. M. & García, A. J. Peptide-functionalized poly[oligo(ethylene glycol) methacrylate] brushes on dopamine-coated stainless steel for controlled cell adhesion. *Acta Biomater.* **59**, 108–116 (2017).

85

119. Wu, C., Zhang, Y., Zhou, Y., Fan, W. & Xiao, Y. A comparative study of mesoporous glass/silk and non-mesoporous glass/silk scaffolds: Physiochemistry and in vivo osteogenesis. *Acta Biomater.* **7**, 2229–2236 (2011).

120. Liu, Z. *et al.* Effect of polydopamine on the biomimetic mineralization of mussel-inspired calcium phosphate cement in vitro. *Mater. Sci. Eng. C* **44**, 44–51 (2014).

121. Seo, C. H., Furukawa, K., Montagne, K., Jeong, H. & Ushida, T. The effect of substrate microtopography on focal adhesion maturation and actin organization via the RhoA/ROCK pathway. *Biomaterials* **32**, 9568–9575 (2011).

122. Lu, J., Rao, M. P., MacDonald, N. C., Khang, D. & Webster, T. J. Improved endothelial cell adhesion and proliferation on patterned titanium surfaces with rationally designed, micrometer to nanometer features. *Acta Biomater.* **4**, 192–201 (2008).

123. Chien, C.-Y., Liu, T.-Y., Kuo, W.-H., Wang, M.-J. & Tsai, W.-B. Dopamine-assisted immobilization of hydroxyapatite nanoparticles and RGD peptides to improve the osteoconductivity of titanium. *J. Biomed. Mater. Res. Part A* **101A**, 740–747 (2013).

124. Chien, C.-Y. & Tsai, W.-B. Poly(dopamine)-Assisted Immobilization of Arg-Gly-Asp Peptides, Hydroxyapatite, and Bone Morphogenic Protein-2 on Titanium to Improve the Osteogenesis of Bone Marrow Stem Cells. (2013) doi:10.1021/am401071f.

125. Yu, X., Walsh, J. & Wei, M. Covalent Immobilization of Collagen on Titanium through Polydopamine Coating to Improve Cellular Performances of MC3T3-E1 Cells. *RSC Adv.* **4**, 7185–7192 (2013).

126. Lee, D. J. *et al.* Dopaminergic effects on in vitro osteogenesis. *Bone Res.* **3**, (2015).

127. Cheng, Y. L., Chen, Y. W., Wang, K. & Shie, M. Y. Enhanced adhesion and differentiation of human mesenchymal stem cell inside apatite-mineralized/poly(dopamine)-coated poly(ε-caprolactone) scaffolds by stereolithography. *J. Mater. Chem. B* **4**, 6307–6315 (2016).

128. Wang, C. X. *et al.* Dopamine D1 receptor-mediated activation of the ERK signaling pathway is involved in the osteogenic differentiation of bone mesenchymal stem cells. *Stem Cell Res. Ther.* **11**, 12 (2020).

129. Ho, C. C. & Ding, S. J. Structure, properties and applications of mussel-inspired polydopamine. *Journal of Biomedical Nanotechnology* vol. 10 3063–3084 (2014).

130. Jiang, J. *et al.* Mussel-Inspired Dopamine and Carbon Nanotube Leading to a Biocompatible Self-Rolling Conductive Hydrogel Film. *Mater. (Basel, Switzerland)* **10**, (2017).

131. Huang, S., Liang, N., Hu, Y., Zhou, X. & Abidi, N. Polydopamine-Assisted Surface Modification for Bone Biosubstitutes. *Biomed Res. Int.* **2016**, 2389895 (2016).

86

132. Luo, R. *et al.* Improved immobilization of biomolecules to quinone-rich polydopamine for efficient surface functionalization. *Colloids Surfaces B Biointerfaces* **106**, 66–73 (2013).

133. Wang, H. *et al.* Design and preparation of porous polymer particles with polydopamine coating and selective enrichment for biomolecules. *RSC Adv.* **7**, 45311–45319 (2017).

134. Zhou, J. *et al.* Improving osteogenesis of three-dimensional porous scaffold based on mineralized recombinant human-like collagen via mussel-inspired polydopamine and effective immobilization of BMP-2-derived peptide. *Colloids Surfaces B Biointerfaces* **152**, 124–132 (2017).

135. Holten-Andersen, N. *et al.* Metals and the Integrity of a Biological Coating: The Cuticle of Mussel Byssus. *Langmuir* **25**, 3323–3326 (2009).

136. Jia, L. *et al.* Polydopamine-assisted surface modification for orthopaedic implants. *J. Orthop. Transl.* **17**, 82–95 (2019).

137. Jo, S. *et al.* Enhanced Adhesion of Preosteoblasts inside 3DPCL Scaffolds by Polydopamine Coating and Mineralization. *Macromol. Biosci.* **13**, 1389–1395 (2013).

138. Ye, Q., Zhou, F. & Liu, W. Bioinspired catecholic chemistry for surface modification. *Chemical Society Reviews* vol. 40 4244–4258 (2011).

139. Kim, S.-S., Sun Park, M., Jeon, O., Yong Choi, C. & Kim, B.-S. Poly(lactide-co-glycolide)/hydroxyapatite composite scaffolds for bone tissue engineering. *Biomaterials* **27**, 1399–1409 (2006).

140. Zhang, J., Yin, H. M., Hsiao, B. S., Zhong, G. J. & Li, Z. M. Biodegradable poly(lactic acid)/hydroxyl apatite 3D porous scaffolds using high-pressure molding and salt leaching. *J. Mater. Sci.* **49**, 1648–1658 (2014).

141. Zhang, C., Wu, X., Qu, F., Qiang, L. & Wang, H. Electrospun Porous PDLLA Fiber Membrane Coated with nHA. *Appl. Sci.* **8**, 831 (2018).

142. Wiggins, J. S., Hassan, M. K., Mauritz, K. A. & Storey, R. F. Hydrolytic degradation of poly(d,l-lactide) as a function of end group: Carboxylic acid vs. hydroxyl. *Polymer (Guildf).* **47**, 1960–1969 (2006).

143. Jaidev, L. R. & Chatterjee, K. Surface functionalization of 3D printed polymer scaffolds to augment stem cell response. *Mater. Des.* (2019) doi:10.1016/j.matdes.2018.11.018.

144. Yuan, X., Mak, A. F. . & Yao, K. Comparative observation of accelerated degradation of poly(l-lactic acid) fibres in phosphate buffered saline and a dilute alkaline solution. *Polym. Degrad. Stab.* **75**, 45–53 (2002).

145. Du, K., Shi, X. & Gan, Z. Rapid biomimetic mineralization of hydroxyapatite-g-pdlla hybrid microspheres. *Langmuir* **29**, 15293–15301 (2013).

146. Zhang, M., Ye, L., Gao, Y., Lv, X. & Chang, J. Effects of hydrolysis on dodecyl alcohol modified β-CaSiO3 particles and PDLLA/modified β-CaSiO3 composite films. *Compos. Sci. Technol.* **69**, 2547–2553 (2009).

147. Puppi, D., Chiellini, F., Piras, A. M. & Chiellini, E. Polymeric materials for bone and cartilage repair. *Prog. Polym. Sci.* **35**, 403–440 (2010).

148. Ma, Z. *et al.* Design and 3D printing of adjustable modulus porous structures for customized diabetic foot insoles. *Int. J. Light. Mater. Manuf.* **2**, 57–63 (2019).

149. Weißmann, V., Bader, R., Hansmann, H. & Laufer, N. Influence of the structural orientation on the mechanical properties of selective laser melted Ti6Al4V open-porous scaffolds. *Mater. Des.* **95**, 188–197 (2016).

150. Liao, X. L., Xu, W. F., Wang, Y. L., Jia, B. & Zhou, G. Y. Effect of porous structure on mechanical properties of C/PLA/nano-HA composites scaffold. *Trans. Nonferrous Met. Soc. China (English Ed.* **19**, s748–s751 (2009).

151. Korpela, J. *et al.* Biodegradable and bioactive porous scaffold structures prepared using fused deposition modeling. *J. Biomed. Mater. Res. Part B Appl. Biomater.* **101B**, 610–619 (2013).

152. Garciandia, L. E. Characterization of rapid prototyped Ti6Al4V bone scaffolds by the combined use of micro-CT and in situ loading. (2009).

153. In Pyo Park, P. & Jonnalagadda, S. Predictors of glass transition in the biodegradable poly-lactide and poly-lactide-co-glycolide polymers. *J. Appl. Polym. Sci.* **100**, 1983–1987 (2006).

154. Guo, T. *et al.* 3D Printing PLGA: A Quantitative Examination of the Effects of Polymer Composition and Printing Parameters on Print Resolution. *Biofabrication* **9**, (2017).

155. Qiang, L., Zhang, C., Qu, F., Wu, X. & Wang, H. Electrospun Porous PDLLA Fiber Membrane Coated with nHA. *Appl. Sci.* **8**, 831 (2018).

156. Wu, T.-F. & Hong, J.-D. Dopamine-Melanin Nanofilms for Biomimetic Structural Coloration. *Biomacromolecules* **16**, 660–666 (2015).

157. Kim, H. W. *et al.* Oxygen concentration control of dopamine-induced high uniformity surface coating chemistry. *ACS Appl. Mater. Interfaces* **5**, 233–238 (2013).

158. Ball, V., Frari, D. Del, Toniazzo, V. & Ruch, D. Kinetics of polydopamine film deposition as a function of pH and dopamine concentration: Insights in the polydopamine deposition mechanism. *J. Colloid Interface Sci.* **386**, 366–372 (2012).

159. Hong, S. H. *et al.* Sprayable Ultrafast Polydopamine Surface Modifications. *Adv. Mater. Interfaces* **3**, (2016).

160. Zhou, P. *et al.* Rapidly-deposited polydopamine coating via high temperature and vigorous stirring: Formation, characterization and biofunctional evaluation. *PLoS One* **9**, (2014).

161. Hejazi, I. *et al.* Investigating the role of surface micro/nano structure in cell adhesion behavior of superhydrophobic polypropylene/nanosilica surfaces. *Colloids Surfaces B Biointerfaces* **127**, 233–240 (2015).

162. Lakshminarayanan, R., Madhavi, S. & Sim, C. P. C. Oxidative Polymerization of Dopamine: A High-Definition Multifunctional Coatings for Electrospun Nanofibers - An Overview. in *Dopamine - Health and Disease* (2018). doi:10.5772/intechopen.81036.

163. Zhang, C. *et al.* Copper Sulphate/Hydrogen Preoxide -Induced Rapid Deposition of Polydopamine Coatings with High Uniformity and Enhanced Stability. *Angew. Chemie Int. Ed.* **55**, 3054–3057 (2016).

164. Ponzio, F. *et al.* Oxidant Control of Polydopamine Surface Chemistry in Acids: A Mechanism-Based Entry to Superhydrophilic-Superoleophobic Coatings. *Chem. Mater.* (2016) doi:10.1021/acs.chemmater.6b01587.

165. Coskun, H. *et al.* Chemical vapor deposition - based synthesis of conductive polydopamine thin-films. *Thin Solid Films* (2018) doi:10.1016/j.tsf.2017.10.063.

166. Ponzio, F., Bertani, P. & Ball, V. Role of surfactants in the control of dopamine-eumelanin particle size and in the inhibition of film deposition at solid-liquid interfaces. *J. Colloid Interface Sci.* (2014) doi:10.1016/j.jcis.2014.06.025.

167. Schneider, A. *et al.* Boric Acid as an Efficient Agent for the Control of Polydopamine Self-Assembly and Surface Properties. *ACS Appl. Mater. Interfaces* (2018) doi:10.1021/acsami.7b08356.

168. Alfieri, M. *et al.* The Chemistry of Polydopamine Film Formation: The Amine-Quinone Interplay. *Biomimetics* (2018) doi:10.3390/biomimetics3030026.

169. Zhou, Z. *et al.* New approach for improving anticorrosion and biocompatibility of magnesium alloys via polydopamine intermediate layer-induced hydroxyapatite coating. *Surfaces and Interfaces* **19**, 100501 (2020).

170. Kaushik, N., Nguyen, L. N., Kim, J. H., Choi, E. H. & Kaushik, N. K. Strategies for using polydopamine to induce biomineralization of hydroxyapatite on implant materials for bone tissue engineering. *International Journal of Molecular Sciences* vol. 21 1–19 (2020).

171. Park, J. *et al.* Surface modification of a three-dimensional polycaprolactone scaffold by polydopamine, biomineralization, and BMP-2 immobilization for potential bone tissue applications. *Colloids Surfaces B Biointerfaces* **199**, 111528 (2021).

172. Chen, W., Tucker, L., Bennett, J., Nichols, L. & Priddy, L. B. Effects of alkali treatment time on nano- hydroxyapatite coating of 3d printed poly (lactic-co-glycolic acid) scaffolds. *Bioceramics* **31**, 21–29 (2019).

173. Sun, Y. *et al.* Interconnectivity of macroporous molecularly imprinted polymers fabricated by hydroxyapatite-stabilized Pickering high internal phase emulsions-hydrogels for the selective recognition of protein. *Colloids Surfaces B Biointerfaces* **155**, 142–149 (2017).

174. Lin, D. *et al.* Rapid initiation of guided bone regeneration driven by spatiotemporal delivery of IL-8 and BMP-2 from hierarchical MBG-based scaffold. *Biomaterials* **196**, 122–137 (2019).

175. Newland, B. *et al.* Macroporous heparin-based microcarriers allow long-term 3D culture and differentiation of neural precursor cells. *Biomaterials* 119540 (2019) doi:10.1016/j.biomaterials.2019.119540.

176. Xu, Z. *et al.* Poly(dopamine) coating on 3D-printed poly-lactic-co-glycolic acid/β-tricalcium phosphate scaffolds for bone tissue engineering. *Molecules* **24**, (2019).

177. Chen, W. *et al.* Alkali treatment facilitates functional nano-hydroxyapatite coating of 3D printed polylactic acid scaffolds. *Mater. Sci. Eng. C* 111686 (2020) doi:10.1016/j.msec.2020.111686.

178. Chen, W., Tucker, L., Teer, L. & Priddy, L. B. Dopamine-assisted nano-hydroxyapatite coating on 3d printed poly ( lactic-co-glycolic acid ) scaffolds. *Biomed Sci Instrum* **56**, 939527 (2020).

179. Li, C., Zhang, J., Han, J. & Yao, B. A numerical solution to the effects of surface roughness on water–coal contact angle. *Sci. Rep.* **11**, 459 (2021).

180. Ito, S. A Chemist's View of Melanogenesis. *Pigment Cell Res.* **16**, 230–236 (2003).

181. Della Vecchia, N. F. *et al.* Tris buffer modulates polydopamine growth, aggregation, and paramagnetic properties. *Langmuir* **30**, 9811–9818 (2014).

182. Chen, L., Shao, L., Wang, F., Huang, Y. & Gao, F. Enhancement in sustained release of antimicrobial peptide and BMP-2 from degradable three dimensional-printed PLGA scaffold for bone regeneration. *RSC Adv.* **9**, 10494–10507 (2019).

183. M, N., F, E., S, M. & A, K. Engineering microscale topographies to control the cell-substrate interface. *Biomaterials* **33**, 5230–5246 (2012).

90

# I

## GENERAL METHODS

### A.1 Fabrication of PLA scaffold

PLA filament (Makerbot, large spool, diameter 1.75mm) was used to fabricate scaffolds with Makerbot Replicator Z18 (MakerBot Industries, LLC, NY, USA) via fused deposition modeling (FDM). SolidWorks 2017 software was used to create and export geometries as stereolithographic (STL) files to be transferred to the 3D printer. The pore size, strut width, and strut height of the designed scaffold were 0.56 mm, 0.2 mm, and 0.2 mm, respectively. The printer extruded filament with a speed of 10 mm s$^{-1}$ in the x-y plane. The nozzle head was heated to 210℃, and melted PLA material was extruded through a 0.4 mm diameter nozzle. Scaffolds for mechanical testing were printed with the dimensions of 4×4×8 mm.

### A.2 Fabrication of PLGA scaffold

The PLGA scaffolds were 3D printed by BIO X (CELLINK, Blacksburg, VA, USA) using a thermoplastic printhead and 0.2 mm nozzle diameter. One g of PLGA pellets were loaded into the cartridge, the plunger was inserted to press the pellets to the bottom of cartridge, and the cartridge and pneumatic tubing were attached to the printhead. Both scaffolds (pore size: 560 µm, porosity: 71.4%) and solid plates (no pores) in the dimensions of 7×7×2 mm (L×W×H) were printed layer by layer from predesigned stereolithographic (STL) files.

### A.3 Fabrication of PLGA-nHA composite scaffold

To obtain a homogeneous mixture, 0.8g PLGA pellet was initially dissolved in 5 ml 1,4-dioxane by magnetic stirring for 1 hours, and then the solution was continuously stirred for 4 hours after adding 0.2g nHA powder to yield a final ratio of PLGA-nHA:1,4-dioxane weight to volume of 1:5. The 3D printed samples were fabricated by BIOX 3D printer using a thermoplastic printhead and 0.3 mm nozzle tip. The g-code file was modified by adding G4 pause command

92

(P500) and assigned layer height (200µm), infill pattern (Recliner), and infill density (100%). The top (1KX magnification) and cross-sectional views (10KX magnification) of the surface morphologies from a representative strut were obtained by SEM scanning. The cross-sectional images were then undergone quantitative particle analysis.

## A.4 Alkali treatment of PLA scaffold

The hydrophobic PLA surface was activated to introduce carboxyl functional groups[84] by immersion of samples in ammonia solution (pH=12.5) under magnetic stirring (180rpm) at room temperature for 1 hour (PLA/1hAT) or 6 hours (PLA/6hAT). Samples were ultrasonicated in 100% ethanol for 3 minutes to remove any residuals from surface and air dried for 1 hour. For nHA coating, samples were immersed in 1% (w/v) nHA (Sigma-Aldrich, St. Louis, MI, USA) in 100% ethanol under magnetic stirring at 180 rpm for 1 hour. The nHA coated samples (PLA/nHA, PLA/1hAT/nHA, and PLA/6hAT/nHA) were ultrasonicated and air dried.

## A.5 nHA, pDA, and pDA-nHA coatings of PLGA scaffold

For preparing the pDA coated samples (denoted as PLGA/pDA), the as-printed samples (scaffolds or solid plates, depending on outcome measure) were soaked in a 4 mg/mL dopamine solution (10 mM Tris-HCl, pH=9.5). The samples were then incubated at 45°C while stirring at 140 rpm (with constant fresh air supplement by two fans) in a BTLab Systems shaking incubator (Geno Technology Inc., USA) for 12 hours. The pDA-induced nHA coating on the PLGA samples (denoted as PLGA/pDA-nHA) was performed in the same manner except for the addition of 0.5 wt% nHA powder in the Tris buffer. Likewise, the nHA coated PLGA samples (denoted as PLGA/nHA) were prepared using the same approach but with only nHA in the Tris buffer. PLGA

93

samples soaked in Tris buffer alone served as controls (denoted as PLGA). After the treatment, all the samples were ultrasonicated with $ddH_2O$ three times (three minutes each time).

### A.6    Surface morphologies and strut width analysis

Surface morphology and strut width were observed using scanning electron microscopy (SEM-Zeiss SUPRA 40, Germany). Prior to imaging, scaffolds (n=6) were sputter coated (EMS 150T ES) with gold-palladium for 2 minutes. Changes in surface morphology resulting from AT and nHA treatments were observed from top, horizontal, and cross-sectional views. For strut width analysis, one top-view image per sample comprising approximately 33% of the total top-view area of the scaffold was collected. The strut widths were analyzed by leveraging an edge-detection method in image processing using a custom script (MATLAB) shown in **Figure A. 1**. For each captured SEM image, four regions of interests (ROIs) were manually cropped from each of 6 struts. The noise level in the relatively small ROI cropped is assumed to be stationary, and thus the edge detection method was implemented on each individual ROI to find the boundaries of strut. The resulting edge map was a binary image with background as value 0 and strut boundaries as value 1. In the edge map, the strut width at each column was calculated by finding the range of pixel locations with value 1. Subsequently, the strut width in each ROI was characterized by averaging all the column-wise evaluation.
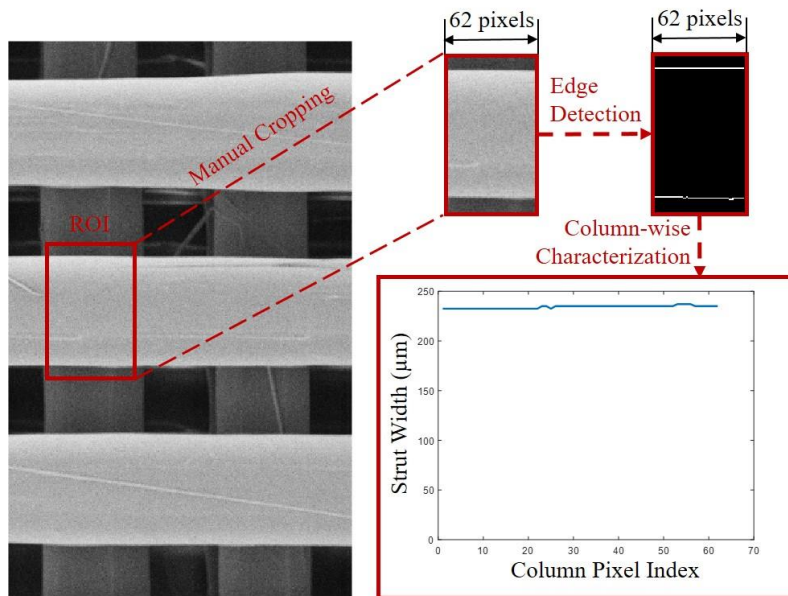
Figure A.1　　Procedure for strut width measurement.

## A.7　　Surface condition analysis

Energy dispersive X-ray spectroscopy (EDX, Zeiss SUPRA 40, Germany) and Fourier-transform infrared spectroscopy (FTIR, ThermoScientific Nicolet 6700) were applied to analyze the surface chemistry of modified scaffolds. Elemental analysis in conjunction with SEM imaging was determined by EDX spectra (to be finished once data obtained). The peaks of functional groups were detected by the collected absorbance in the range of 525 cm$^{-1}$ to 2000 cm$^{-1}$ from the FTIR spectrum. Regarding the measurement of water contact angle, 15 µL of water was added drop-wise on the top surface of solid plates (n=5). Images were captured within 5 seconds with a Leica Triple Camera and processed using the angle tool of ImageJ software (NIH). Surface roughness was scanned and analyzed by Keyence VR 5000 Series Software (KEYENCE CORPORATION OF AMERICA, Itasca, IL U.S.A.) (**Figure A. 2**). The surface of 6 struts

95

were scanned, and 7 lines at the center of each single strut for each scaffold (n=3) were analyzed using the multi-line surface roughness mode.
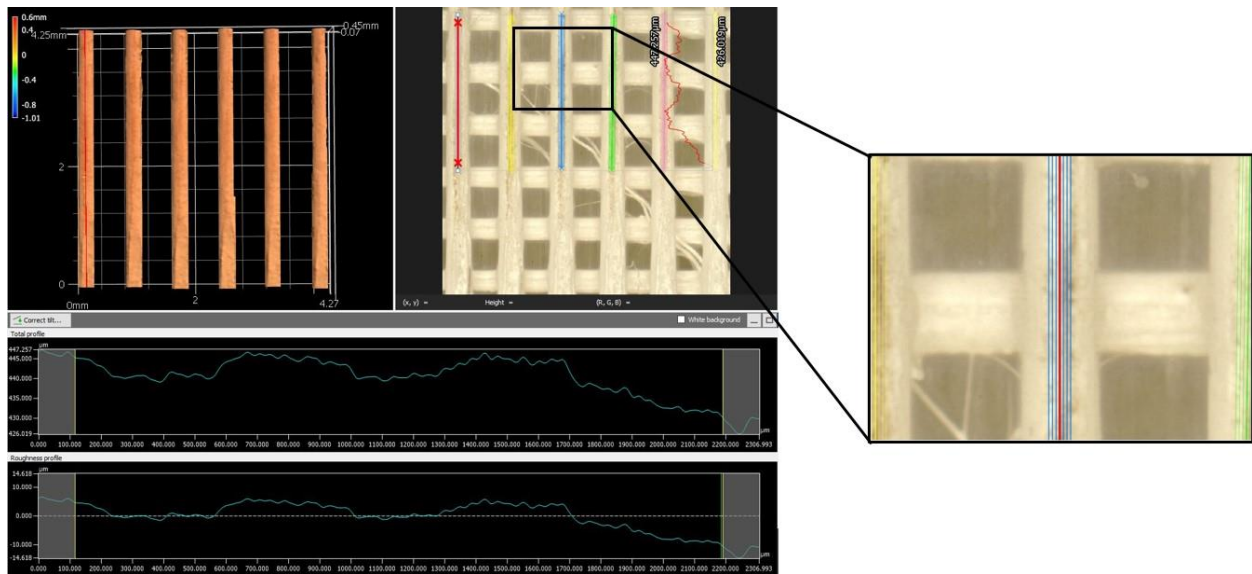


Figure A.2    Procedure for surface roughness analysis.

### A.8    nHA particle analysis

The frequency particle diameter and the nearest neighbor distances (NND) of the nHA particles in PLGA matrix were measured via ImageJ. The nHA particles in the SEM image were defined with boundaries by the range of the particles' diameters (0.04-0.35 µm) under binary mode (threshold = 18.93%). Then, the "analyze particle" function collected the areas of all the defined particles. A histogram was produced based on the frequency of the particle diameter in GraphPad. The NND analysis was performed by the NND plugin tool of ImageJ, which measured the distance between one particle and the particle nearest to it.

96

### A.9 Compression testing

Uniaxial compression tests were performed on scaffolds with dimensions of 4×4×8 mm (n=8) via Instron 5882 (Illinois Tool Works, Inc., IL, USA) at 1 mm/min with a preload of 5N. The stiffness (k) was calculated from the linear portion of the force-displacement curve (**Equation A.1**), where F was the applied force and $\Delta L$ was the compressive displacement. The cross-sectional area (A) was calculated from one layer of struts based on SEM images (**Equation A.2**), where $\overline{W}$ was the average strut width for each group, $L_s$ was the length of a single strut (4 mm), and N was the number of struts in a single layer. Since the 3D printed scaffold was not solid, effective Young's modulus $(E_e)$[148] was calculated by **Equation A.3**. To compare with native bone, the effective Young's modulus was replaced with Young's modulus in Chapter IV. Therefore, the cross-sectional area was obtained from the multiplication of the length and width of scaffold (4 mm × 4 mm).

$$k = \frac{F}{\Delta L} \tag{A.1}$$

$$A = \overline{W} \times L_s \times N \tag{A.2}$$

$$E_e = \frac{F \times L}{A \times \Delta L} \tag{A.3}$$

### A.10 *In vitro* cell culture

Mouse osteosarcoma cells (ATCC® CRL™-2836) or mouse preosteoblasts (MC3T3-E1) were cultured in minimum essential medium (α-MEM), 10% fetal bovine serum (FBS, Atlanta Biologicals, GA, USA), and 1% penicillin/streptomycin (PS). Culture medium was replaced every 3 days. The two-layer scaffolds (n=10) were sterilized by soaking into 70% ethanol and evaporated

overnight. Subsequently, $5 \times 10^4$ osteosarcoma cells or MC3T3-E1 were seeded dropwise on all over the top of the scaffolds in a 48-well plate. The cell seeded scaffolds were statically incubated at 37°C, 5% $CO_2$ conditions for 1 hour to allow the cells to attach before 400 µL extra medium was added to each well. The cell attachment and proliferation on scaffolds were evaluated longitudinally using a Cell Counting Kit-8 (CCK-8, Sigma Aldrich, MO, USA) assay on days 1, 3, and 5. According to the manufacturer's protocol, at each time point, the media and CCK-8 reagent were mixed a ratio of 9:1 before adding to the wells. After 4 hours incubation, the solution was transferred to new wells for measuring the absorbance at 450nm with 650nm background on µQuant microplate photometer (Bio-Tek Instruments, Inc). The scaffolds were washed with PBS, and fresh media was replaced for CCK-8 measurements at subsequent timepoints. Total cell number was normalized to cross-sectional area. The effects of surface modification on cell proliferation was further compared to initial cell attachment by normalizing cell numbers on days 3 and 5 to cell number on day 1 for each treatment.

### A.11   Analysis of thermal properties

Poly (D, L-lactide-co-glycolide) (PLGA, LA:GA=75:25, MW=156 kDa) with ester end-group and pellet size of 1-3 mm was used for all experiments (LACTEL® Absorbable Polymers, Birmingham, AL, USA). To determine the operating temperature range for thermoplastic 3D printing, a differential scanning calorimeter (DSC, TA Q20, New Castle, DE, USA) was used to determine the glass transition temperature (Tg) and melting point (Tm) of PLGA pellets. Additionally, the thermal decomposition temperature (Td) was measured via thermogravimetric analysis (TGA). 8.6 mg of PLGA pellets were heated from 40℃ to 300℃ at a heating ramp of 10℃/min in aluminum crucibles with nitrogen as the gas medium.

98

## A.12   Statistical analysis

Statistical analyses were conducted using SAS 9.4 (SAS Institute Inc., Cary, NC) and all results were reported as mean ± standard deviation. The differences in strut width, surface roughness, elemental quantification, water contact angle, stiffness, Young's modulus, effective Young's modulus, and cell growth were assessed by either one-way or two-way analysis of variance (ANOVA) with Tukey's post-hoc test for pairwise comparisons based on the experimental design, and p-values $< 0.05$ were considered statistically significant.